A Study on Microstructure and Properties of Fe-xCr alloys and Fe-9Cr Based ODS Alloys Processed via Spark Plasma Sintering

A Dissertation

Presented in Partial Fulfillment of the Requirements for the

Degree of Doctor of Philosophy

with a

Major in Materials Science and Engineering

in the

College of Graduate Studies

University of Idaho

by

Arnab Kundu

Major Professor: Indrajit Charit, Ph.D.

Committee Members: Krishnan S. Raja, Ph.D.; Samrat Choudhury, Ph.D.;

Thomas Williams, Ph.D.

Department Administrator: Eric Aston, Ph.D.

May 2019

Authorization to Submit Dissertation

This dissertation of Arnab Kundu submitted for the degree of Doctor of Philosophy in Materials Science and Engineering and titled "A Study on Microstructure and Properties of Fe-xCr alloys and Fe-9Cr Based ODS Alloys Processed via Spark Plasma Sintering" has been reviewed in final form. Permission, as indicated by the signatures and dates below, is now granted to submit final copies to the College of Graduate Studies for approval.

Major Professor: ……………………………..   Date: ………………………
                                        Dr. Indrajit Charit

Committee Members:
                                    ……………………………..   Date: ………………………
                                        Dr. Krishnan Raja

                                    ……………………………..   Date: ………………………
                                        Dr. Samrat Choudhury

                                    ……………………………..   Date: ………………………
                                        Dr. Thomas Williams

Department
Administrator: ……………………………..   Date: ………………………
                                        Dr. Eric Aston

Abstract

Fe-Cr based oxide dispersion strengthened (ODS) alloys are potential candidates for usage as nuclear fuel cladding material for the upcoming Generation-IV nuclear reactor, especially in liquid sodium cooled fast reactors. These high performance materials have many advantages since they possess remarkable mechanical strength at high temperature and outstanding irradiation resistance. Particularly, ODS steels known as nanostructured ferritic alloys have negligible swelling under irradiation, and equally excellent creep properties because of nano-reinforcements i.e. the nanometric oxides present in the matrix. Traditionally, ODS processing combines mechanical alloying (MA) followed by hot consolidation via hot extrusion and hot isostatic pressing. In the present study, the ODS alloys are produced by a combined route of MA and Spark Plasma Sintering (SPS). After consolidation, the effects of processing parameters including milling parameters and sintering parameters, on the microstructure characteristics and mechanical properties of the milled powder and consolidated alloys are investigated. Once the suitable parameters are decided for the maximum compaction state for Fe-9Cr alloy, Fe-Cr alloys were produced with varying Cr content to understand the effect of Cr on the process of MA and SPS. Secondly, the effect of bimodal distribution obtained by various MA time has been observed after consolidation process. Finally, having understood the basic fundamentals of processing of Fe-Cr alloys, Fe-9Cr ODS was produced with addition of W and Ti and oxide particles as dispersoid phase. During the process of MA, the oxides get dissolved in the matrix and during consolidation process these oxides get precipitated as nanophases in the matrix thus resulting in the higher strength. In general, yttria (Y_2O_3) has been used as the oxide which is added to the Fe-Cr alloy system. Recently some work has been done on the addition of lanthana (La_2O_3). In this study,

we have introduced a new oxide (CeO_2) in the same amount (wt%) compared to Y_2O_3 and La_2O_3 to understand the effect of CeO_2 on the ODS alloy. Powder and consolidated alloys characterization were performed using Scanning electron microscopy (SEM), Electron backscatter diffraction (EBSD) and Transmission electron microscopy (TEM). The mechanical properties were evaluated using microhardness testing and mini-compression testing. Corrosion tests were conducted at room temperature in various to understand the nature of the oxide layer formed on the Fe-Cr and Fe-9Cr ODS materials. Mechanical alloying created high density of dislocations, vacancies in the powder and facilitated the nucleation of NCs. It resulted in faster densification behavior by initiating sintering at lower temperatures by lowering the activation energy for both grain boundary and volume diffusion. Maximum densification (around 98%) occurred at temperatures 1000 ^{O}C for a sintering time of 45 min at 80 MPa pressure for 10 h ball milled powder. Due to the combined strengthening mechanisms of work hardening, grain refinement, dispersion strengthening and solid solution strengthening, superior strength was achieved for the materials. On addition of alloying elements and the rare earth oxides, the presence of second phase particles like $Cr_{0.875}Ti_{0.125}$ is observed along with Ti-Cr-O-RE type precipitates which imparts high strength to the matrix both at room temperature an at elevated temperatures.

Acknowledgements

I would sincerely like to thank my major professor Dr. Indrajit Charit for giving me the opportunity to work in the project and with his group. The guidance and support that he has been rendering upon me through past three years is truly admirable. I am very much grateful for his trust, time, patience and encouragement.. I truly appreciate the freedom that he has given me to bring in my own ideas in this project. Without him this dissertation would not be in the format presented here.

I would like to thank Dr. Thomas Williams for teaching me various instruments in the microscopy center and for having the faith in me to work on those alone. Without his support the work here would not have been as it looks now.

I would want to thank Dr. Krishnan Raja for his immense help and contribution in helping me understand various steps of the corrosion study performed in the project, which has turned to be one of the intricate aspects of the work.

I would like to express my sincere gratitude my committee members; Dr. Tom Williams, Dr. Krishnan Raja and Dr. Samrat Choudhury for their valuable comments and taking time out of their tight schedule for improving the quality of my dissertation.

I would like to acknowledge Dr. Eric Aston as the chair of the department of Chemical and Materials Engineering Department at University of Idaho and other faculty members. I truly appreciate the help of Chemical and Materials Engineering Department staff specially Mrs. Margaret Baker, Mrs. Gail Bergman, Dr. Dave MacPherson and Mr. Charles Cornwall for helping me a lot during past three years.

Dedication

The thesis is dedicated to my parents for their unconditional love and support.

Table of Contents

List of Figures

List of Tables

Chapter 1: Introduction

1.1. Motivation

Before the industrial revolution, the energy requirement was moderate. For heat energy people relied on the sun during day and burned wood at night. For mode of transportation, we depended on muscle power of animals on land and force of wind on sea. For doing our work that we could not do with our own labour, we used animals. We used the wind and water power to drive the simple machines to plant grain and pump water. The evolution of the steam engine by Thomas Newcomen and James Watt in the mid 1700s opened up a world of new possibilities. More convenient than wind and water, and less expensive than a stable full of horses, steam engines were used to power locomotives, factories, and various other daily chores. The main fuel for steam engine was wood and later coal. Very soon coal became a very usable source of energy- from heating houses to running steam engines to various extraction process of metals. In 1880, coal powered a steam engine attached to the world's first electric generator. Thomas Edison's plant in New York City provided the first electric light to Wall Street financiers and the New York Times [1]. A year later, the world's first hydroelectric power plant went on-line in Appleton, Wisconsin- river water was used for producing electricity. By the late 1800s, petroleum was discovered. A material which was once contaminating wells for drinking water became a huge source of energy. By the end of the century, gasoline produced from petroleum was being used for running internal combustion engines. With the low-cost automobile and low cost of electricity, the society's energy requirement started increasing drastically almost doubling every 10 years, resulting in the construction of huge power plants, coal plants and hydroelectric dams. Power lines

extended hundreds of miles between cities, bringing electricity to rural areas. After World War II revealed the destructive power of nuclear energy, people started thinking of using this huge power source for the benefit of mankind. And then started the advent of the nuclear reactors and nuclear industry.

The nuclear energy is produced by the nuclear fission process in the nuclear reactor. The basic process of a nuclear fission is that a high energy neutron strikes a fissionable element or a fissionable composite. On striking the fissionable material, there is a decomposition process – the fissionable material breaks down into fission fragments, supplementary neutrons and high energy. The most well-known fission material is uranium or uranium dioxide. Each fission reaction of U-235 produces in average 2.5 neutrons. These neutrons strike other U-235 atoms and thus the chain reaction continues. Almost 99.25% of the neutrons are prompt neutrons i.e. they get released instantaneously (10-14 secs) while the rest 0.75% neutrons released at about 20 secs, known as delayed neutrons, play a very important role in controlling the nuclear fission reaction. An average energy of 193.5 MeV is released per fission reaction. The fission reaction of U235 can occur in 30 different ways leading to a possibility of 60 different fission fragments. The energy produced is transferred to the coolant through the cladding material, which gets warmed up to volatile form and drives the turbine blade and thus produces electricity. Thus, the nuclear energy is a clean form of energy as it does not produce any harmful greenhouse gases and also the carbon foot print is less. The present day reactors have limited energy efficiency and produce large volumes of nuclear waste. More advanced nuclear reactors, which are currently under investigation, are expected to allow more efficient and safer use of nuclear energy. In all these cases, the fuel cladding is the most important safety barrier in fission nuclear reactors, as it restrains most of the radioactive

fission products within its volume [2]. The main purpose of fuel cladding in a nuclear reactor are: (i) to provide a structure to hold fuel pellets, and (ii) to retain the fission products and prevent direct contact between coolant and fuel. So, cladding material must possess good ductility, impact strength and creep strength so that the cladding integrity is maintained during the reactor operation. The material must also be easily fabricated. The resistance to corrosion by coolant must be high for a material to be used as cladding. The cladding material must possess high melting point. Since cladding separates fuel and coolant, it presents resistance to heat transfer from fuel to coolant. To ensure rapid removal of fission heat, the cladding material must have high thermal conductivity. The material of cladding must not be damaged by neutron irradiation. The material also must possess low absorption cross section for neutrons. The costs to fabricate and to assemble should also be optimized in order to facilitate maintenance and disposal. Aluminium, beryllium, magnesium and zirconium are generally considered for cladding. Aluminium is used in small, research reactors. Magnox, an alloy of magnesium is used in gas-cooled reactors. Zircaloy-2 and Zircaloy-4, alloys of zirconium, possess good mechanical properties and have superior resistance to corrosion and are used in thermal power reactors. The corrosion resistance property of zirconium is increased by addition of tin, iron, chromium and nickel. By addition of these metals to zirconium, the low absorption cross section for neutrons remains almost the same. However, zircaloy-2 has tendency to react with hydrogen, an undesirable event. This drawback was also minimized by restraining the concentration of Sn and Fe in the Zircoloy-2 thus producing a new material Zircoloy-4. The requirement of low absorption cross section may not be satisfied for upcoming Gen-IV fast reactors. However, a material with low swelling under higher fast neutron fluence is required. Ferritic/martensitic (F-M) ODS steels have both low swelling and

good resistance to corrosion by liquid sodium. Hence, F/ M ODS can be used as cladding material in sodium cooled fast reactors. Mechanical alloying (MA) has emerged as a competitive route for processing these high temperature alloys in the beginning of 1970s. Generally, the oxide dispersion strengthened (ODS) alloys are processed via MA and hot isostatic pressing (HIP) followed by a series of thermo-mechanical processing steps.

1.2. Objective

One of the main purposes of this work is to eliminate the need for hot extrusion and hot pressing as intermediate processing steps by fabricating a process route for the usage of spark plasma sintering (SPS) to process advanced ODS alloys. SPS systems offer many advantages over conventional techniques such as hot pressing, hot isostatic pressing or atmospheric furnaces, including ease of operation and accurate control of sintering energy resulting in lower temperature sintering and less time, applicability to both electrically conductive and non-conductive materials and fabricating material with reduced anisotropy.

Traditionally, Y_2O_3 is the rare earth oxide used as dispersoids in ODS alloys. However, this work has utilized La_2O_3 and CeO_2 in ODS steels in place of Y_2O_3 because of their similar thermodynamic stability, abundance and lack of prior studies [3].

1.3. Dissertation Overview

The dissertation consists of 6 chapters. Chapter 1 gives us an overview of the motivation and objective of the work. Chapter 2 depicts an insight on the previous work done by various researchers on this field. Chapter 3 provides us an understanding on the fabrication route of Fe-9Cr alloy by high energy ball milling and spark plasma sintering. Chapter 4 tells us about the effect of varying chromium percentages on the properties of spark plasma sintered Fe-xCr

alloys. Chapter 5 briefs us about the properties of new Fe-9Cr ODS alloys. Chapter 6 gives us an insight in the irradiation behaviour of pure iron alloys. Chapter 7 is about the future works that can be done in order to understand the Fe-Cr alloy system for potential application usage.

References

1. Vaclav Smil, *Energy in World History,* Westview Press, 1994.

2. P. Yvon and F. Carré, Structural materials challenges for advanced reactor systems, J. Nucl. Mater. 385 (2009) 217.

3. K.S. Rajan, Selection of Materials for Reactor Internals, School of Chemical & Biotechnology, SASTRA University.

Chapter 2: Background

2.1. Oxide dispersion strengthened (ODS) alloys

The worldwide energy demand between 2012 and 2040 is expected to grow by nearly half as described by Energy Information Administrator (EIA). The demand of developed country will rise by 18% while developing country demand will jump by 71%, with Indian, Southeast Asian, and African demand more than doubling. To meet the future energy demand, the need for designing and higher stability of nuclear power plants with higher energy efficiency is required. The energy sources have to go way beyond their limit to function specially at high temperatures. Such developments cannot be achieved without the development of materials which will show superior properties at higher temperatures. The ODS alloys have shown excellent potential for high temperature applications. They exhibit excellent creep strength and oxidation resistance at high temperatures. ODS alloys have potential applications in tubing for high temperature heat exchangers, sheet for burners and combustion chambers, fuel cladding materials for next generation nuclear reactors and gas turbine engines [1].

The ODS alloys were first discovered by William Coolidge in 1910 when he was working at General Electric (GE) Company [2]. He manufactured thorium oxide dispersed tungsten to improve the creep resistance of tungsten. Then, the first dispersion strengthened material was designed as a structural load bearing system. In 1970, Benjamin [3] developed mechanical alloying to combine yttrium oxide and gamma prime hardening in a complex nickel-based superalloy.

Oxide dispersion strengthening occurs due to the incoherency of the oxide particles within the lattice of the material. The oxide particles pin the dislocations within the material thus hindering its movement which in turn prevents creep. Since the oxide particles are incoherent, dislocations can only move by climb. Climb is less energetically favorable and occurs only at high temperatures. Climb can occur either at the particle-dislocation interface or by overcoming multiple particles [4]. However, the dislocation, even after overcoming particle by climb, can still get pinned at the particle-matrix interface, which further requires additional threshold stress to detach the dislocation out of this pinning effect. [5].

In spite of the various advantages of the ODS alloys at high temperatures, some challenges are faced in the usage of these alloys, mainly: (a) high processing costs, (b) joints fabricated by conventional fusion welding techniques have low creep strength at high temperatures, and (c) secondary recrystallization needs to be optimized [6],

2.2. Ferritic/Martensitic ODS alloys

Concepts for the next generation of nuclear power reactors designed to meet increasing demand for energy include water-cooled, gas-cooled, and liquid-metal-cooled reactors. Depending on operating conditions, some of the designs favor the use of elevated-temperature ferritic/martensitic steels for in-core and out-of-core applications. Ferritic/martensitic steel has a number of advantages, such as (a) high thermal conductivity, (b) low thermal expansion, (c) compatibility to heavy liquid metal coolant, (d) void swelling resistance, © He-embrittlement resistance (at doses> 150 dpa), (f) High density of irradiation-defect sinks, (g) negligible radiation-induced hardening and embrittlement (above 450 ^{O}C). On the other hand, there are a significant number of disadvantages like (a) microstructural instability under

irradiation and high temperatures, (b) radiation-induced segregation, (c) intergranular segregation and intergranular fracture, (d) precipitation of brittle phases, and © insufficient creep strength. In order to overcome these obstacles, people decided to introduce a high number density of stable, fine-scale, precipitates that pin the motion of dislocations. Thus, came the advent of ODS F/M steels. The main advantages of the F/M ODS steels are: (a) high, stable dislocation sink strengths, (b) large numbers of stable, nanometer-scale precipitates that trap He in fine-scale bubbles, (c) reduced swelling, (d) stabilized grain boundaries, © high creep strength, and (f) maximum service temperature is 700 ^{O}C.

One of the important areas of application of these ODS steels is sodium cooled fast reactor fuel cladding material. The structural material components for the advanced nuclear reactors will be exposed to higher temperatures (700 ^{O}C) and severe radiation exposure (200 dpa and beyond) [7]. Recent development in ODS steels allow them to be used as fuel cladding in upcoming sodium-cooled fast reactors because oxide particles dispersed in the ferritic or ferritic/martensitic matrix improve the radiation resistance and creep resistance at high temperature. The ODS steels has not only the oxide particle nanoclusters composed of Y–Ti–O atoms but also micron-size grain morphology. But the fabrication route for these ODS steels as long, thin-walled cladding material has been still difficult. The main problem that people have been facing was in low hoop strength because of elongated fine grains parallel to the rolling direction [8]. To address the issue, F/M 9Cr-ODS steels are being developed. The 9Cr ODS steels have been previously developed by melting, casting and a combined process of MA and extrusion. Various properties of Fe-9Cr ODS alloy have been investigated before like microstructural characterization, mechanical properties, void formation after irradiation,

damage structure before and after irradiation, and so forth. Some of the work that has been done before is listed in the table below.

Table 2.1: Various studies previously conducted on Fe-9Cr based ODS alloys

Author	Material	Processed	Topics investigated
C. Topbasi et al. [9]	NF616 (Fe-8.8Cr-.1C)	arc melting	Voids formed by Kr irradiation
S. Li et al. [10]	Fe-9Cr-.01C	melting	Nanoindentation after irradiation, SRIM
K. Ono et al [11]	Fe-9Cr	casting	He ion irradiation effects
K. Ono et al. [12]	Fe–9Cr–2W	casting	Formation of bubbles and voids
W. Eiichi et al. [13]	Fe-9Cr	casting	Damage structure and Mech. Prop after Neutron irradiation
L. Toualbi et al. [14]	Fe–9Cr–1W–0.2Ti–0.3Y$_2$O$_3$	MA, hot extrusion	Microstructural and Mechanical properties
L. Toualbi et al [15]	Fe–9Cr–1W–0.3Ti–0.2Y$_2$O$_3$	MA, hot extrusion	Microstructural and Mechanical properties
K. Rajan et al [16]	Fe9Cr-1Mo-0.5Y$_2$O$_3$	MA, SPS	Microstructural and Mechanical properties

Recent efforts are ongoing to produce the Fe-9Cr ODS alloy by a combined route of mechanical alloying (MA) and spark plasma sintering (SPS). These newly developed process makes us have more control over the grain structure, defects formation and other properties which may make them more amenable for application as nuclear fuel cladding material.

2.3. Mechanical Alloying (MA)

Ball milling or mechanical alloying (MA) is a powder processing technique that allows production of homogeneous materials starting from blended elemental powder mixtures. It involves repeated cold welding, fracturing, and re-welding of powder particles in a high-energy ball mill. MA has been utilized as a primary processing step toward manufacturing iron-based and nickel-based ODS alloys. This technique was first developed in a nickel-based superalloy intended for gas turbine applications [17-19].

The MA process starts with pouring a powder mixture in a stainless steel container sealed under a protective argon atmosphere to avoid oxidation during milling along with a grinding medium (generally hardened steel or tungsten carbide balls). In some cases of milling ductile powders such as Ni, about 1–2 wt.% of a process control agent (PCA) (usually stearic acid) is normally added in order to avoid excessive cold welding of the particles. This mix is then milled for the desired length of time until a steady state is reached when the composition of every powder particle is the same as the proportion of the elements in the starting powder mix. The types of mills generally used are SPEX shaker mills (back-and-forth shaking motion is combined with lateral movements), planetary ball mill (centrifugal force produced by the vials rotating around their own axes and that produced by the rotating support disk) and attritor mills (centrifugal force produced by rotating horizontal drum half-filled with small steel balls). The SPEX shaker mill can mill powder up to 10 g whereas planetary ball mills can go up to a few 100 gm of powder. The attritor mills can mill powder in the range of 0.5 kg to 40 kg. Some recent commercial mills can even go up to 1250 kg. The time required for processing are short in the SPEX mills and are longer in the attritor mills. A comprehensive article about MA processing can be found in work by C. Suryanarayana [20]. Various factors come into

play during the process of MA: (a) mill type, (b) milling container, (c) milling speed, (d) milling time, © type and size of the grinding medium, (f) ball-to-powder weight ratio (BPR), (g) extent of filling the vial, (h) milling atmosphere, and (i) temperature of milling. Many of these processing parameters are interdependent. So, for understanding the process of MA one has to take care of each of the parameters efficiently.
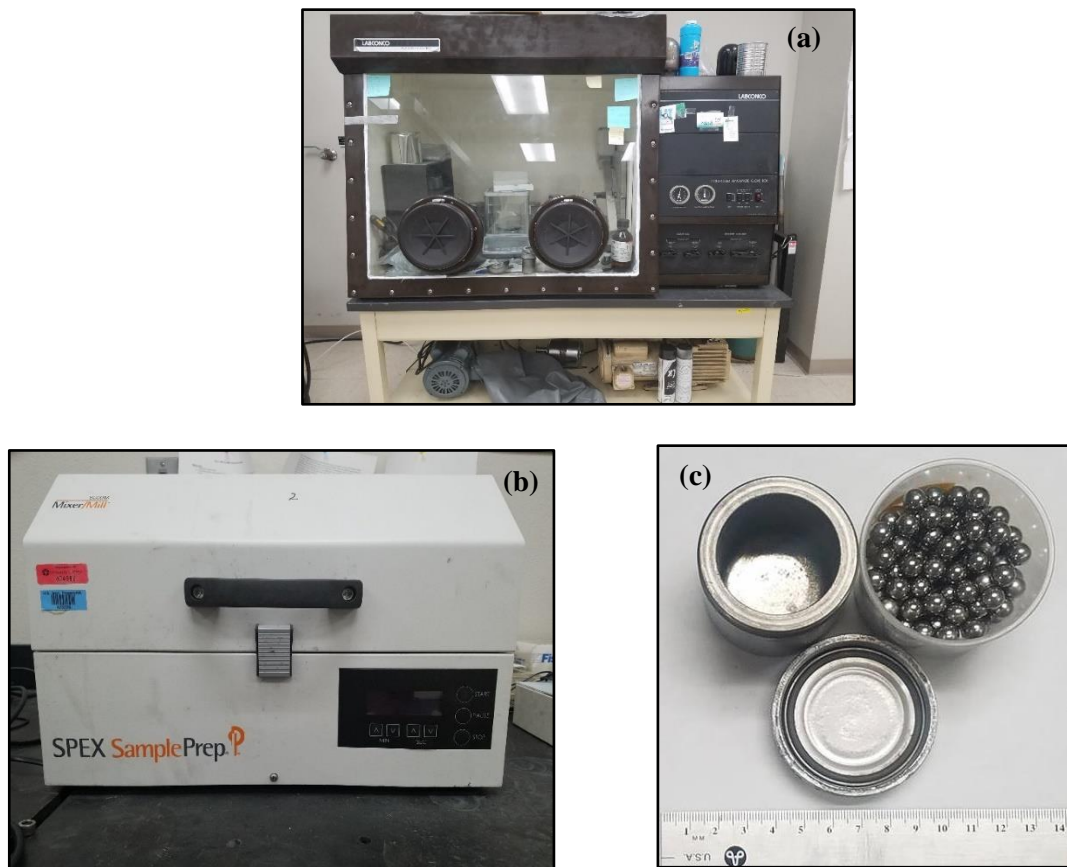
Figure 2.1: (a) Argon atmosphere controlled glove box, (b) SPEX shaker Mill, (c) Stainless steel vial and stainless steel grinding balls

In the process of MA, the powder particles are repeatedly cold welded, fractured and re-welded. During the process, steel balls are colliding with each other and some powder is always trapped in between them (Figure 2.2). About 1000 particles with an aggregate weight of about 0.2 mg are trapped during each such collision event [20]. Due to this process of impact, the powder particles get plastically deformed. This results in formation of new bigger

surfaces which in turn helps the particles to weld together, thus leading to an increase in particle size. So, powder with wide range of powder particle size gets produced.
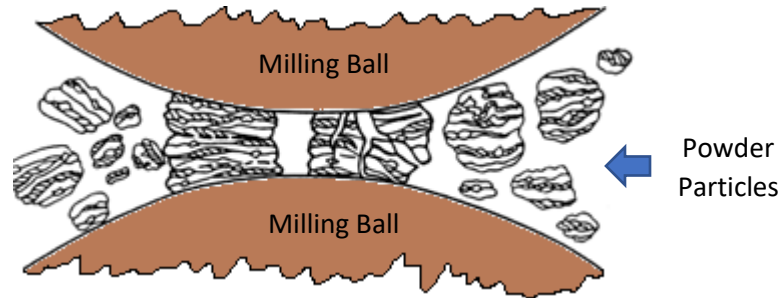
Figure 2.2: Ball-powder-ball collision of powder mixture during mechanical alloying.
[Courtesy Elsevier]

At this stage, the newly formed particles have a layered structure consisting of various combinations of the beginning constituents. As more time elapses in the milling process, the particles get work hardened and repeatedly fractured and re-welded. After milling for a certain length of time, a balance is achieved between the rate of welding, which tends to increase the average particle size and the rate of fracturing, which tends to decrease the average particle size. At this equilibrium stage it is found that each particle contains substantially all the starting ingredients, in the proportion they were mixed together at the beginning. Also, the particles reach saturation hardness due to the accumulation of strain energy. The particle size distribution at this stage also becomes narrow, because particles larger than average are reduced in size due to fracture at the same rate that fragments while smaller than average gets bigger due to welding [21].

During MA, the process of solid solution comes into occurrence. Solid solubility is achieved between two foreign materials under some conditions which are known as Hume-Rothery rules. According to this rule, solid solution occurs when: (a) atomic size difference is

< 15%, (b) both has the same crystal structure, (c) both have similar electronegativity and (d) both have almost similar valency. It is generally assumed that solid solubility limit depends on the ratio of intermixing due to shear forces to the decomposition of the solid solution. When the ratio is very large, a fully random solid solution is achieved. During MA, due to nanostructures formation solid solubility increases as there is higher volume fraction of atoms at the grain boundaries which results in enhanced diffusion paths.

From thermodynamic point of view, an analogy can also be drawn on solid solution process during MA [22]. It is known that the average free energy of a mechanical mixture powder composed of pure components of *A* and *B* with molar free energy of $\mu_A{}^\circ$ and $\mu_B{}^\circ$, respectively can be determined as below [25]:

$$G\{mixture\} = (1-X)\mu_A^\circ + X\mu_B^\circ \qquad (2.1)$$

where *X* is the molar fraction of *B*.

But during MA, the atoms are not only in mixture but also in solid solution. This results in a deviation from the general mixing law. This is because the number of ways the particles gets arranged in mechanical mixture is less than that after MA process. As a result, the enthalpy of the MA particles becomes different from normal mechanical mixture. The general way of depicting the free energy diagram for these two different conditions is shown in Figure 2.3.
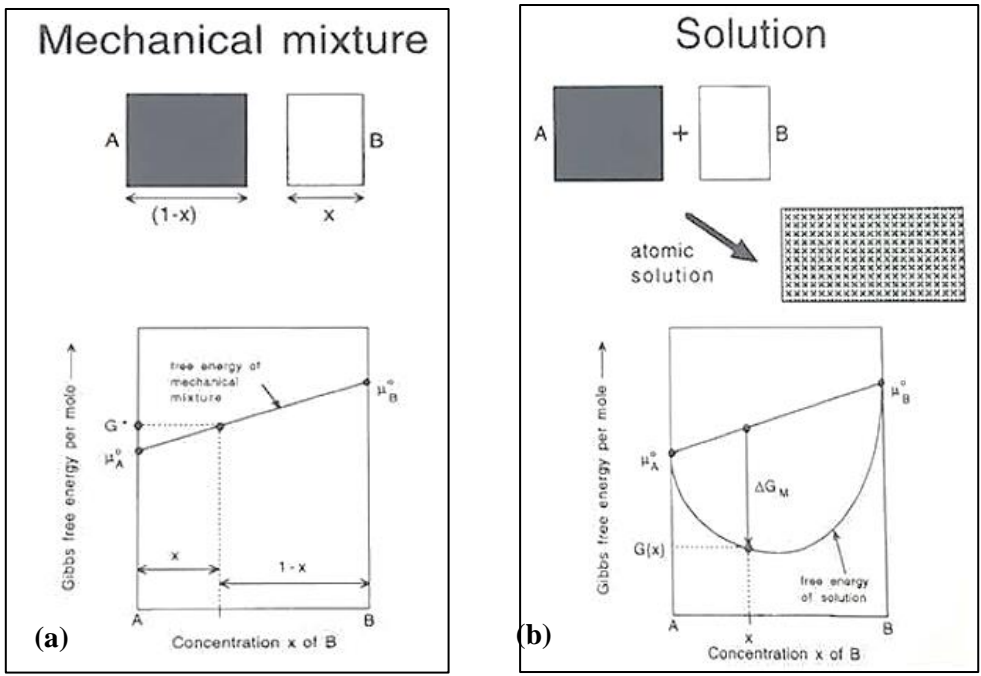
Figure 2.3: Gibbs Free Energy diagram for (a) mechanical mixing and (b) solid solution [22]

Figure 2.4 shows the process of reduction of particles by the process of MA until an atomic solution is achieved [22].
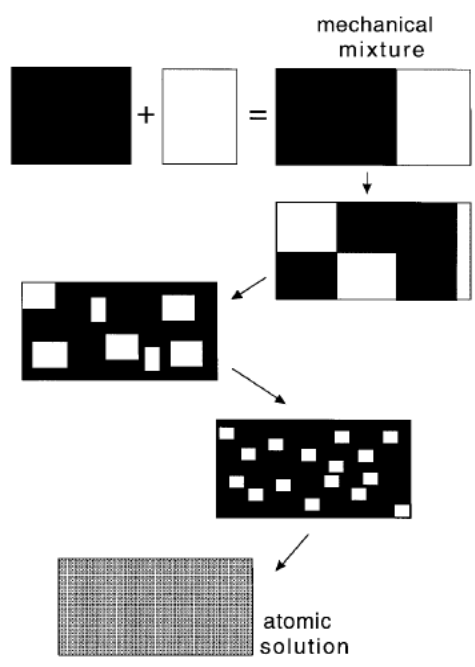
Figure 2.4. Schematic of formation of atomic solution during MA [22] (Courtesy of Taylor and Francis)

So, the question that arises here is that at what level of particle size we can consider the process of MA to be forming solid solution. So, for this let us consider at the beginning that there is no enthalpy of mixing. Assuming that there are m_A atoms per powder particle of A and m_B atoms per particle of B and the powders are mixed in a proportion that gives an average mole fraction X of B. The molar entropy of mixing when $m_A = m_B = 1$ can be calculated in the following equation [22]:

$$\Delta S_M = - k N_a \times [(1-X)\ln(1-X) + X\ln(X)] \qquad (1.2)$$

This shows that when the particle sizes are reduced to atomic scale, the largest reduction in free energy occurs. But the entropy of mixing cannot be neglected in general. Only when the particle sizes are very small it can be neglected as shown in Figure 2.5.
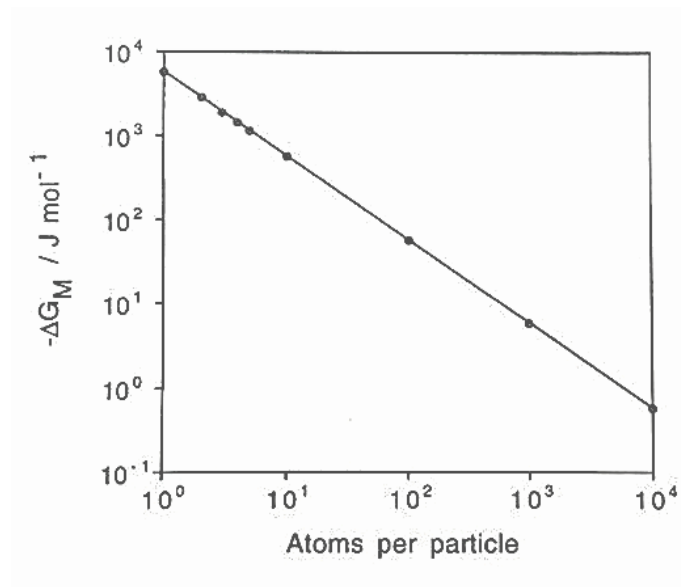
Figure 2.5. Molar Gibbs Free Energy as a function of particle size [22] (Courtesy of Taylor and Francis)

In commercial purpose, powder metallurgy produces powder of size 100 μm. So, the entropy of mixing can be neglected totally. But the enthalpy of mixing will not be zero as assumed before. Enthalpy of mixing is defined as the heat/enthalpy released when two or

materials are mixed together. Intermolecular forces (mainly the binding energy) are the main factors driving the change in the enthalpy. The binding energy is the change in energy as the distance between a pair of atoms is reduced from ∞ distance to an equilibrium distance. So, for a pair of A atoms it is written $-2\varepsilon_{AA}$. From the standard theory of atomic solutions, the molar enthalpy of mixing is given by [22]:

$$\Delta H_M = zN_a(1-X)X\omega, \text{ where } \omega = \varepsilon_{AA} + \varepsilon_{BB} - 2\varepsilon_{AB} \qquad (2.3)$$

where z is the coordination number of the material A. In the case where the particles are not mono-atomic, only the particles present at the interface between two dissimilar atoms will be influenced by the unlike atoms. In that scenario the enthalpy of mixing can be written as [22]:

$$\Delta H_M = zN_a \, \omega 2\delta \, S_V X \, (1-X) \qquad (2.4)$$

where S_V is the amount of interfacial area per unit volume for two dissimilar atoms, 2δ is the thickness of the interface and δ is a mono-layer of atoms. The interfacial energy per unit area, σ is given in the following equation [22]:

$$\Delta H_1 = V_m S_v \, \sigma \qquad (2.5)$$

where V_m is the molar volume. During MA, the particle size gets reduced and thus S_v significantly increases. So, the model predicted above is in contrary to the formation of solid solution. The dissolution of particles during MA is only possible when the interfacial energy decreases as particles become smaller. This can be only achieved if the particles gain coherency with the matrix lattice as they become smaller due to fracture and welding of particle. The particles dissolution is the inverse of precipitation mechanism and is shown in Figure 2.6. As the particle size becomes smaller and smaller, higher coherency is achieved and this reduces the interfacial energy of the system.

(a) coherent   (b) coherent   (c) incoherent
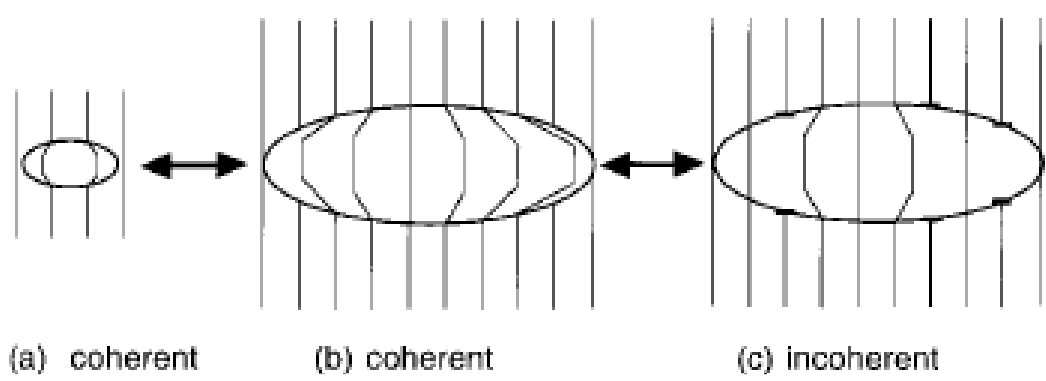
Figure 2.6. Changes in coherency as a function of particle size [22] (Courtesy of Taylor and Francis)

Again, the degree of solubility does not increase after a certain period of milling time. The solid solution generally increases with increasing milling time as the diffusion occurs. But after certain time, when supersaturation is achieved there is no more solid solubility as shown in Figure 2.7 [21].

Solid Solubility

Milling Time
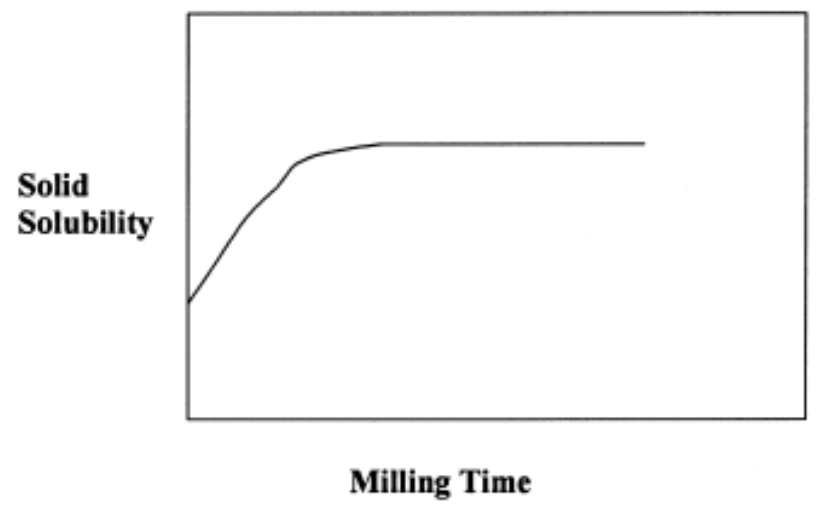
Figure 2.7. Variation of solid solubility with time during MA process [21] (Courtsey to Elsevier)

Again, it has been seen that in case of two component metals which form an isomorphous system, the lattice parameter of one of the metals decreases where as that of the other increases

with milling time. Once equilibrium conditions are reached, the two lattice parameters merge and a homogeneous solid solution is formed as shown in Figure 2.8 [20].
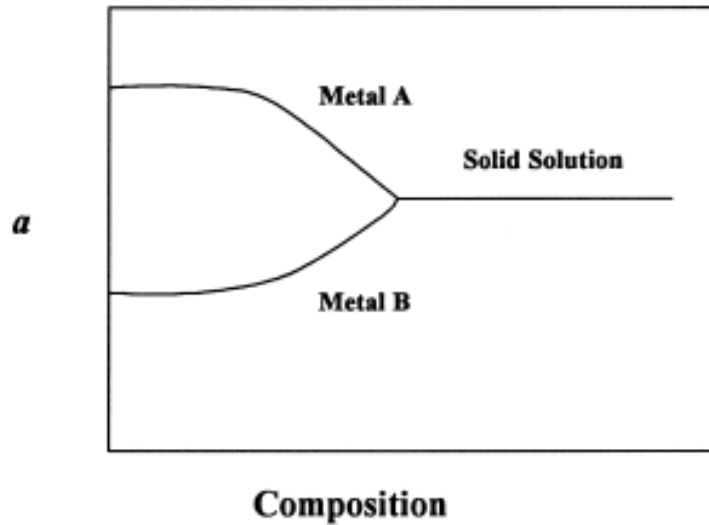
Figure 2.8. Variation of schematic variation of the lattice parameter of the individual component phases with milling time in a binary alloy system during MA process [20] (Courtsey to Elsevier).

In the course of the milling process, a gradual deterioration of effectivity is generally observed. In general, three stages are observed during milling according to mechanochemistry as shown in Figure 2.9 [23].

(a) Rittinger stage: In this stage the interaction of particles is negligible, and the energy input is approximately proportional to the new surface area (Stage-I).

(b) Aggregation stage: In this stage the new surface area produced is not proportional to the energy input because of particle interaction (aggregation). But the degree of dispersion increases significantly (Stage-II).

(c) Agglomeration stage: In this stage the increase in dispersion drops to a negligible value and then stops. Surface area decreases as the particles start agglomerating due to chemical bonds (Stage-III).
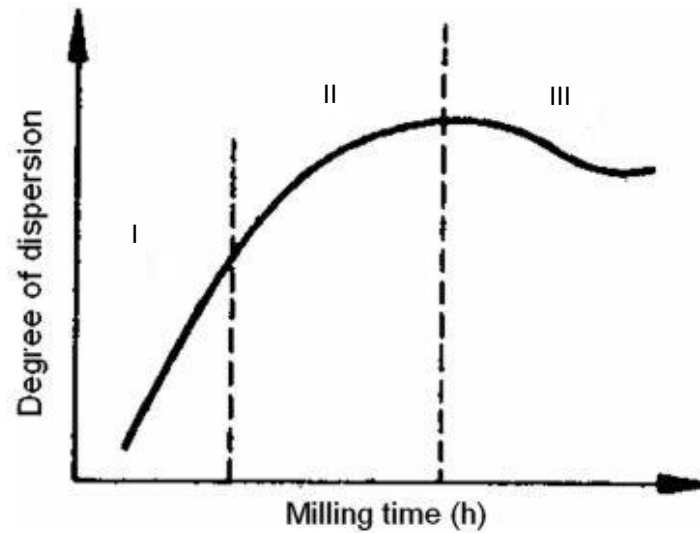
Figure 2.9. Three stages of High Energy Milling [23]

MA of ODS powder is a type of ductile-brittle alloying process. The brittle oxide particles are dispersed in a ductile matrix phase. Figures 2.10(a–c) illustrates a typical microstructural evolution during MA of the ODS alloys. During the initial stages of milling, due to high collisions between ball and powder, the ductile particles get crushed and flattened. On the other hand, the brittle oxide particles get fragmented and get trapped in the ductile particles and along the inter-lamellar spacing as depicted in Figure 2.10(a). With further milling, the lamellae get refined as shown in Figure 2.10(b). With further milling, lamellae get further refinement and the brittle oxide particles get consistently dispersed as shown in Figure 2.10(c) [20].
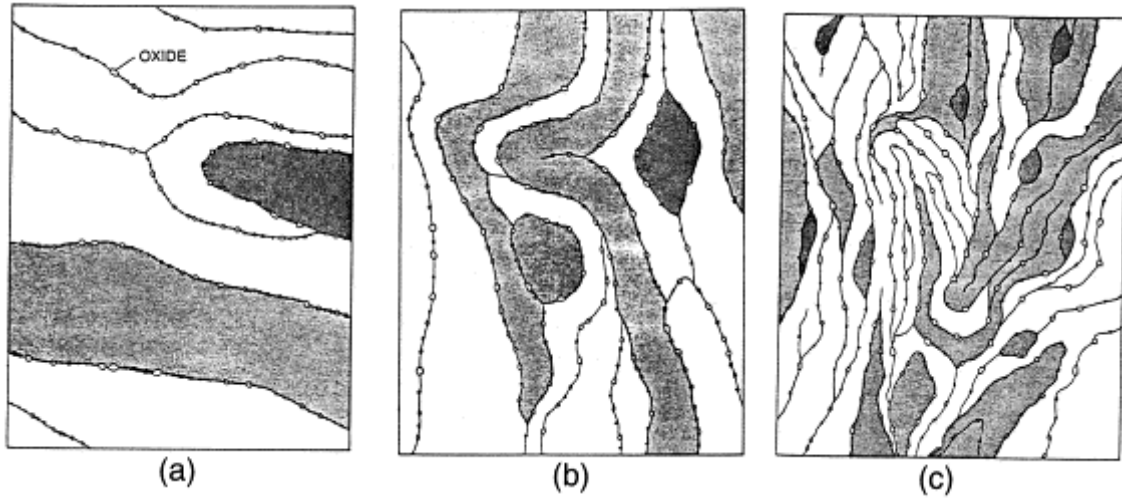
Figure 2.10(a-c). Schematics different stages of microstructural evolution during MA of ODS alloys of Er_2O_3 in α_2-titanium aluminide matrix (Courtesy of Elsevier) [20]

Mechanical alloying provides both solid solution strengthening and precipitation hardening in ODS alloys. In processing ODS alloys, the role of ball milling appears complex because two major phenomena occur at the same time: dissolution of solutes within the matrix and nucleation of the first nanoclusters [24, 25].

2.3. Compaction of milled powder

Compaction is an important step in powder processing as it enables the forming of loose metal powders into required shapes with enough strength to withstand the sintering process. In this process loose powders are converted into required shape with sufficient strength to withstand ejection from the tools and subsequent sintering process. In some case like cemented carbide, hot compaction is done followed by sintering. Different compaction process is shown in Figure 2.11.
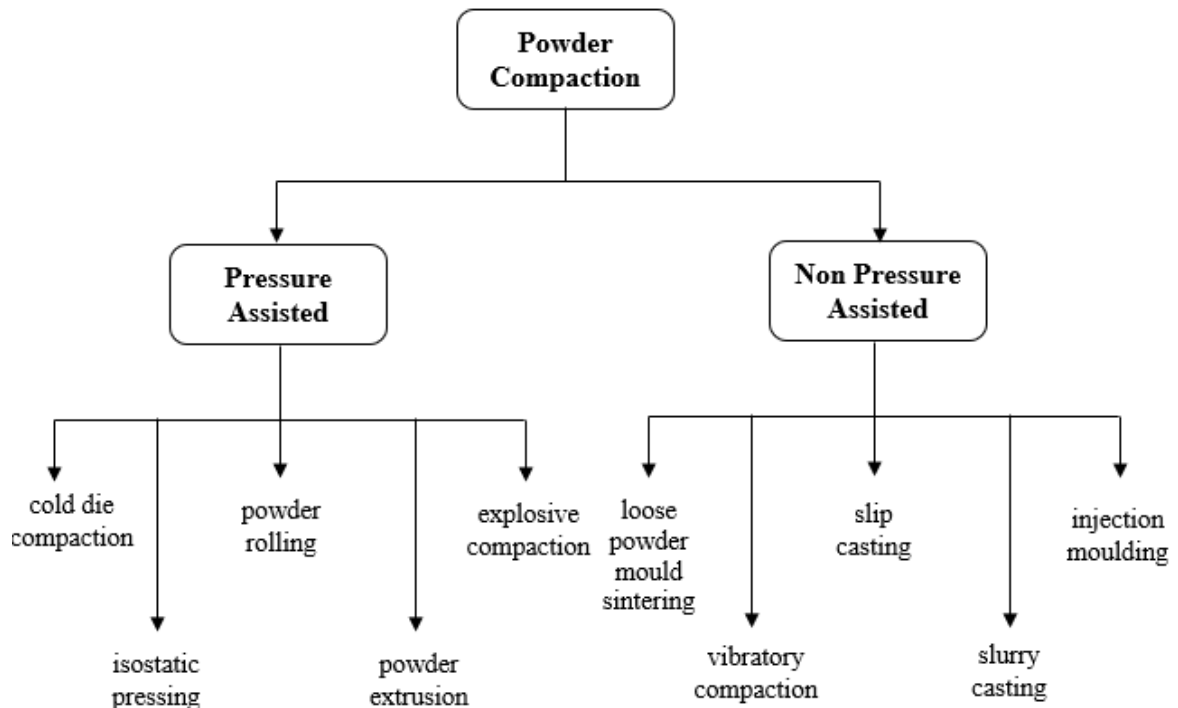
Figure 2.11. Different types of compaction process

During the process of compaction, powder particles flow past each other and interact with both surrounding particles and the also the die and punch. Also, the particles get deformed in the process. In case of homogeneous compaction, in the initial stage, rapid densification occurs due to the rearrangement of the particles. In the second stage increased applied pressure

results in elastic and plastic deformation resulting in cold working and locking of the particles. In the second stage the rate of densification is much less compared to the first stage. Figure 2.12 depicts a general compaction process. According to the usage of apparatus, compaction can be also be of two types:

a. Single end die compaction: In this case, powders close to the punch and die walls experience much better force than in centre. So, the green density varies across the sample length. This non-uniformity in green density results in non-uniformity in properties of sintered part.

b. Double end die compaction: In this case, powder particles experience more uniform pressure from both top and bottom, resulting in minimization of density variation. But there is still possibility of variation if the components have high aspect ratio (length to diameter ratio). This means that long rods and tubes cannot be produced by die compaction.
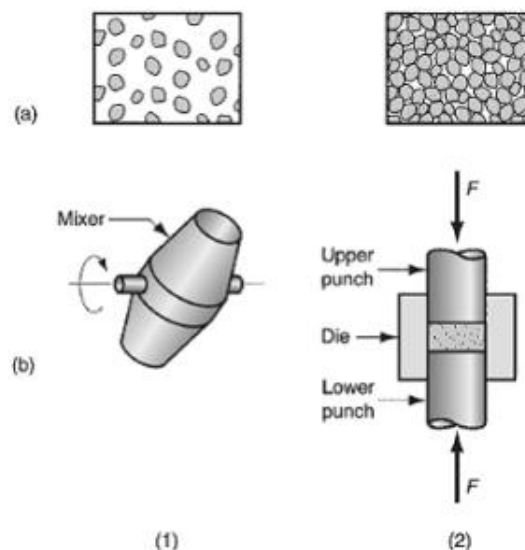
Figure 2.12. The conventional powder metallurgy production sequence: (1) blending and (2) compacting; (a) shows the condition of the particles, whereas (b) shows the operation and/ or work part during the sequence [26]

2.4. Consolidation/sintering of compacted powder

Sintering is the process of making objects from powder, by heating the material in a furnace below its melting point so that bonding takes place by diffusion of atoms. This leads to individual powder particles adhering to each other in a dense compact. There are different types of sintering: (a) Solid state sintering, (b) Liquid Phase sintering, (c) Activated sintering, (d) Reaction sintering, (c) Rate controlled sintering, (f) Microwave sintering, (g) gas plasma sintering, (h) Spark plasma sintering, etc.

The most effective approach for ODS alloy fabrication is powder metallurgy route consisting of MA of the starting powders, followed by consolidation using either hot extrusion (HE) or hot isostatic pressing (HIP). Appropriate thermo-mechanical processing (TMP) is often performed to improve the microstructure and mechanical properties. Recent studies are now being carried out on processing route via spark plasma sintering (SPS). A general process for ODS alloy fabrication is shown in Figure 2.13.
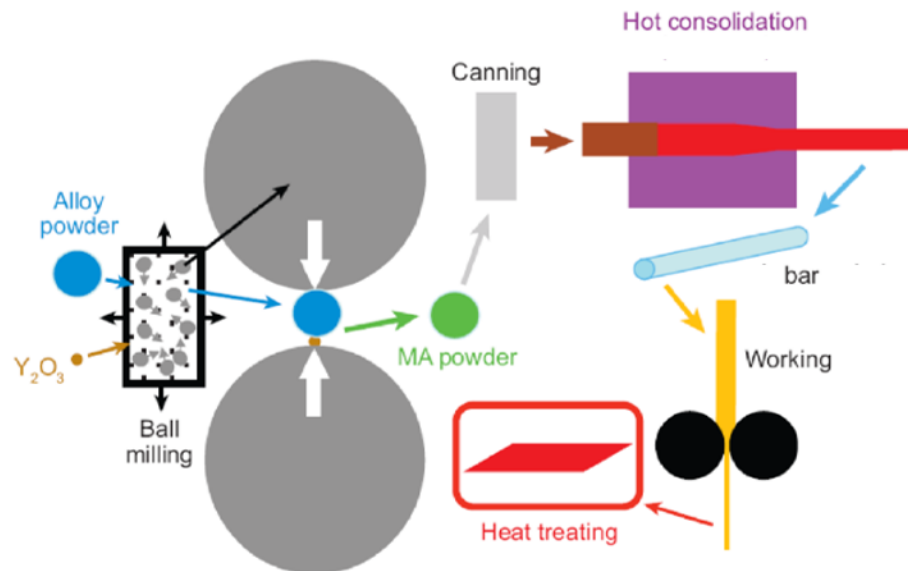
Figure 2.13. The conventional route of ODS alloy processing [7]

During the sintering process, the powder gets compacted in three step process (Figure 2.14(a-d)) which are:

1. Initial Stage: In this stage neck and grain boundary formation occurs along with smoothening of the surface. In this stage the relative reaches in the range of 60-65%. Linear shrinkage generally occurs around 3-5%.

2. Intermediate stage: In this stage isolated pore structures are formed. Grain growth and densification also occurs in this stage. In this stage the relative density reaches in the vicinity of 65-95%.

3. Final stage: In this stage the pores starts shrinking and grain growth occurs. The relative density in this stage reaches 95-99%.

(a)   (b)   (c)   (d)
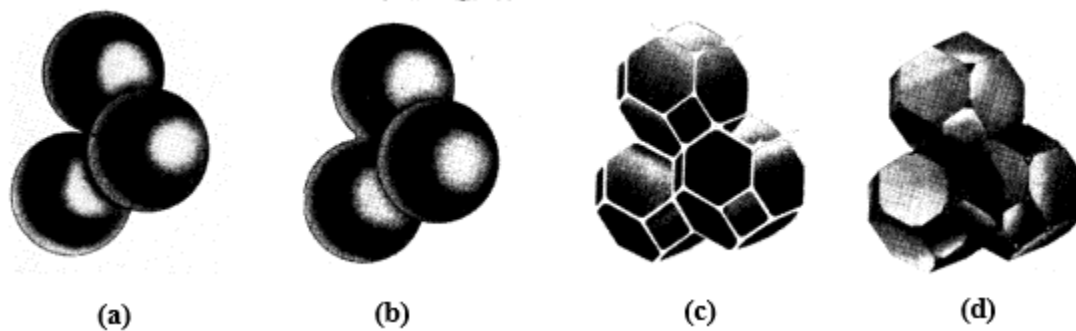
Figure 2.14: (a) Initial stage of sintering: model structure represented by spheres in tangential direction, (b) Near end of initial stage and the spheres have start to coalesce, (c) Intermediate stage: dark grains have started to take the shape of tetrakaidecahedron, enclosing white pore channels along grain boundary; (d) Final stage: pores are tetrahedral inclusions at corners where four tetrakaidecahedra meet. [27]

One of the important features of the consolidated products is that the grain size is extremely small, probably the smallest achieved in case of bulk material. When these materials are further heat treated, grain coarsening occurs and anisotropy nature starts developing in the materials which is ideal for application as high temperature material where superior creep resistance is important. During the process of sintering, recovery and

recrystallization may also take place depending on the working temperature. The process of recrystallization is a complex one. There are various mechanisms for recrystallization based on various factors like: (a) precipitation, (b) formation of high angle boundaries from the sub grains formed during the early stage of consolidation and (c) strain induced boundary migrating (SIBM) in which a 'bulge' develops on a high angle boundary as a result of strain gradients across the boundary [28]. While recrystallization occurs in general alloys at about $0.5T_m$, in case of ODS alloys the recrystallization temperature shoots up as high as $0.9T_m$. The reason behind is that grain-boundary junction pinning represents a much larger force against recrystallization nucleation than the dispersoid pinning. This explains the high recrystallization temperatures irrespective of alloy system when the grain structure is sub-micrometer in size. Again, these phenomena depend on the way of processing these ODS alloy. The typical ways of processing ODS alloys are:

(a) Hot isostatic pressing of the ODS powder

Hot isostatic pressing (HIP) is the simultaneous application of high temperature and pressure in all directions to produce a dense material. During the process, the material is surrounded by an inert atmosphere. The compacted powder undergoes a thermal treatment at high pressure to achieve consolidation. Because of the isostatic nature of the pressurising medium, various material shape can be produced by this process. The critical aspect of this technique is that the interface must be isolated from the gaseous pressure medium. This is often achieved by encapsulating the component. During this process the applied pressure can be as high as 200 MPa and the temperature can also reach to 2000 ^{O}C. This HIP process is generally used in the manufacture of both ceramics and alloys. Recent work has been done in

producing ODS and NFSs by this method. Figure 2.15 shows a typical fabrication route by HIP process.
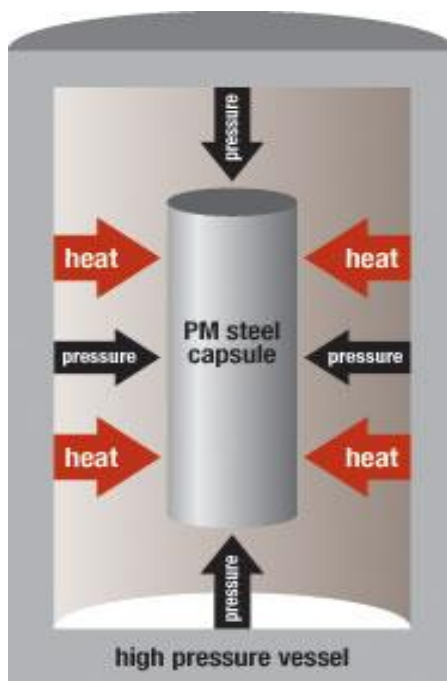
Figure 2.15. The HIP process of consolidation [29]

HIP process has been widely practiced for the fabrication of Fe-Cr ODS alloy. Previous work by Haijian Xu et al. [30] has shown the fabrication of Fe-15Cr ODS steel with the HIP process. Microstructural and mechanical property evolution of Fe-9Cr ODS alloy produced by MA and HIP has been done by L. Toualbi et al. [14,15]. In the work by Chen-yang Lu et al. [31], the author has described that during the MA process, Y_2O_3 gradually gets dissolved in the ferritic matrix. With increasing milling time, the powder particles changed morphology from spherical to laminar and again back to spherical. After HIP process the author has reported the formation of high density non-stoichiometric Y–Ti–O-rich nano-clusters and a few stoichiometric $Y_2Ti_2O_7$ precipitates are formed in the ODS alloy. The $Y_2Ti_2O_7$ precipitates had a size of 7 nm. While with increasing temperature, Y-Ti-O nanoclusters were stable, the size of the $Y_2Ti_2O_7$ precipitates kept on increasing.

(b) Spark Plasma Sintering of the ODS powder

Spark plasma sintering (SPS) is a thermal and pressure assisted compaction/sintering process. It is also known as field assisted sintering technique (FAST) [32] or pulsed electric current sintering (PECS) [33]. This process utilizes a combined action of a pulsed direct electrical current (DC) and pressure to perform high speed consolidation of powder. The direct way of heating allows very high heating rates, thus increasing densification due to enhanced diffusion [34-36]. It is regarded as a rapid sintering method in which the heating power is distributed over the volume of the powder compact and the heating power is dissipated exactly at the contact points of the powder particles. SPS systems offer many advantages over conventional techniques such as hot pressing (HP), hot isostatic pressing (HIP) or atmospheric furnaces, including ease of operation and accurate control of sintering energy resulting in lower temperature sintering and less time, and applicability to both electrically conductive and non-conductive materials.

The first sintering under electric current was performed in 1906 [36]. Inoue invented the "spark sintering" based on pulsed current, but commercialization did not come to a large success [38]. In 1953, a German company developed a similar process using AC current. Lockheed Missile and Space Co. bought parts of Inoue's work but successful implementation in industry is not known [39-44]. In the early 1990s, Japanese companies started the industrial production of spark plasma sintering machines. After that, Germany and USA started producing similar equipment based on pulsed DC current. Art present several companies from China, Korea, Japan, etc. offer FAST/ SPS set-ups. Today, the total number of FAST/SPS devices or equivalent (among them Dr Fritsch GmbH) installed in the world is estimated to 1750.

In SPS process, the application of fast heating rate (up to 1000 ^{O}C/min), short holding times (less than an hour) and low sintering temperatures (200–300 °C lower than most of the conventional sintering techniques) [45-49] help in a faster fabrication route. In SPS, the pulsed electric current disperses the heating power at contact points of the powder particles ensuring rapid densification process [34].

The main reason behind the faster consolidation during the SPS process is the dominance of surface diffusion, diffusion through the melt, or time-independent processes such as plastic deformation [49] in contrast to the kinetically slow diffusion mechanisms such as grain boundary and volume diffusion. For this faster densification process, SPS has been quite successful in the production of cutting tools, Figure 2.16 represents a schematic diagram of SPS process.
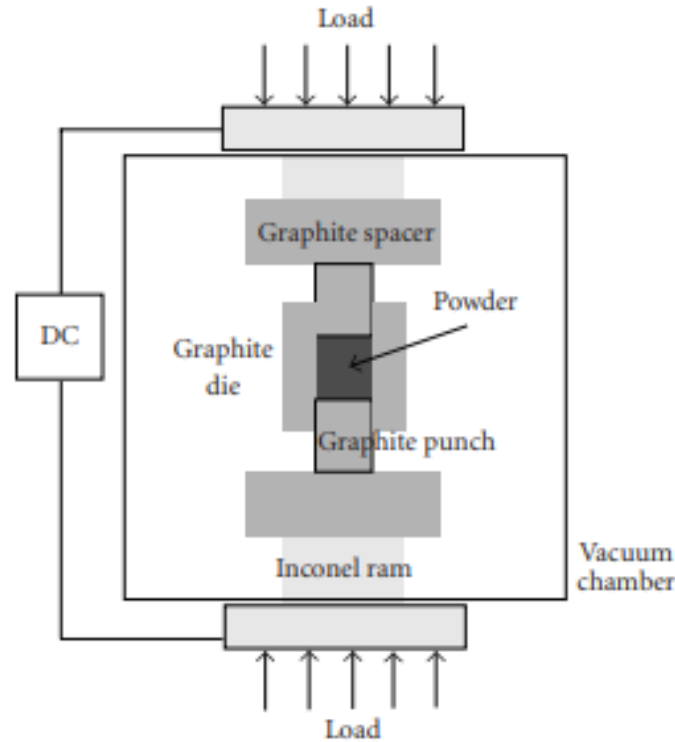
Figure 2.16. The SPS process of consolidation [51]

The SPS system consists of a uniaxial hydraulic unit and built-in water-cooled special energizing mechanism, a water-cooled vacuum chamber, atmosphere controls, vacuum exhaust unit, special sintering DC pulse generator and a computer program controller. A Dr. Sinter SPS-515S machine (formerly manufactured by SPS Syntex Inc. and currently manufactured by the Fuji Electronic Industrial Co. Ltd.) is shown in Figure 2.17(a). This machine has the current capacity of 1500 A and hydraulic capacity of 50 kN operating in 12:2 pulsed pattern mode (current is applied for 12 ms, followed by a 2 ms of no current). Powder material is stacked a graphite die with two punches on top and bottom (Figure 2.17(b)). High pressure and pulsed current are applied through two punches for the compaction process. Figure 2.17(c) shows the intermediate stage during the process of sintering.
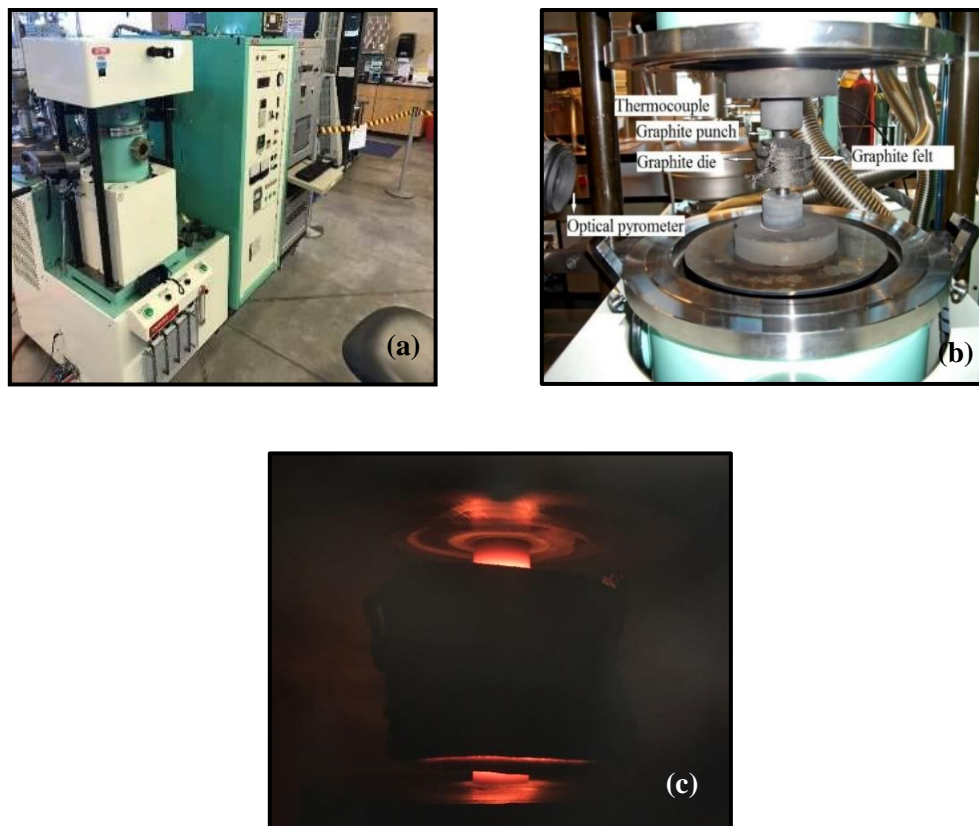
Figure 2.17. (a) The Dr. Sinter SPS-515S machine at CAES, Idaho Falls, (b) The SPS setup and (c) Sintering occurring at 1000 $^{\circ}$C

During the process of SPS a lot of mechanisms occur simultaneously as proposed by researchers and some of them are summarized as below [34]:

(i) Plasma generation

In the work by Inoue [38], the author predicted that ionization at the inter-particle contact due to spark discharges due to micro capacitive nature, develops 'impulsive pressures' facilitating diffusion of the atoms at powder particles contacts. The pulsed current has also a cleaning effect on the particle surfaces. The proof was based on the observation of a grain boundary formed between particles without any oxidation [52]. The generation of plasma is still debated, but it seems to be widely accepted that occasional electric discharges may take place on a microscopic level.

(ii) Electroplastic effect

Metal powders exhibit lower yield strength under an electric field. In the work by Raichenko et al. [53] and Conrad [54], the researchers observed the effects of high density electric current pulses on the flow stress of metals at low homologous temperatures.

(iii) Joule heating

The electric current that flows through particles creates Joule heating effect that aids in the consolidation of the particles. Joule heating also helps in cleaning powder surfaces which provides more preferred paths for current flow.

(iv) Pulsed current

The pulsed DC current theoretically generates spark plasma, spark impact pressure, Joule heating and an electrical field diffusion effect. Gas and other impurities present on the particle

surface gets removed due to very high temperature generated on the surface. Figure 2.18 illustrates the flow of pulsed current through powder particles.
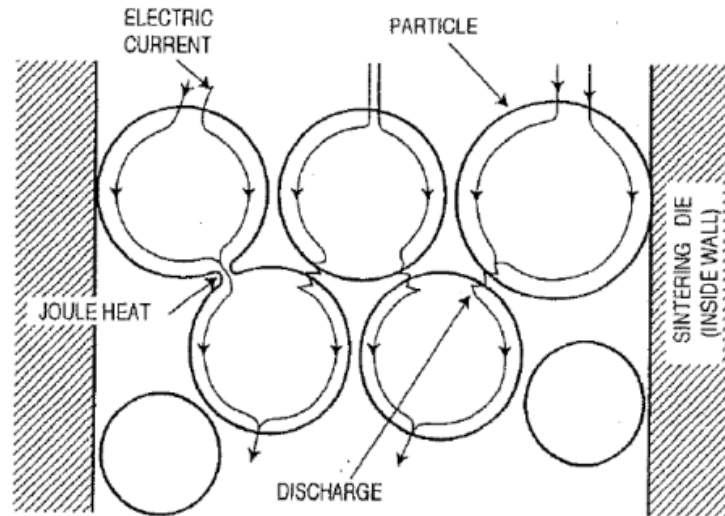
Figure 2.18 Flow of pulsed current through powder particles inside SPS [34]

(v) Hydraulic pressure

The high localized temperature at the inter-particle contacts under the influence of a uniaxial pressure allows the yield strength to be surpassed. Thus, particles start to deform plastically and in the process get consolidated.

2.5. Microstructural studies of compacted powder

Microstructural evaluation has been done for various Fe-9Cr ODS steels processed via MA, HIP and SPS. In the study by Q.X. Sun et al. [55], Fe-9Cr-0.3Y$_2$O$_3$ has been produced. The powder was produced by sol-gel and hydrogen reduction method resulting in the powder size to be around 100-300 nm (Figure 12.19(a)). After the process of SPS at 1150 ^{O}C for 5 min at 50 MPa pressure, it was found that the size of the oxide particles present on the matrix

varied from 14 nm to 20 nm (Figure 2.19(b)). The energy dispersive spectroscopy (EDS) during the microstructural evaluation by transmission electron microscope (TEM) analysis revealed the presence of Y-Ti-O complex particles (Figure 2.19(c-d)). The volume of the Y-Ti-O complex particles were more than the corresponding oxide particles.
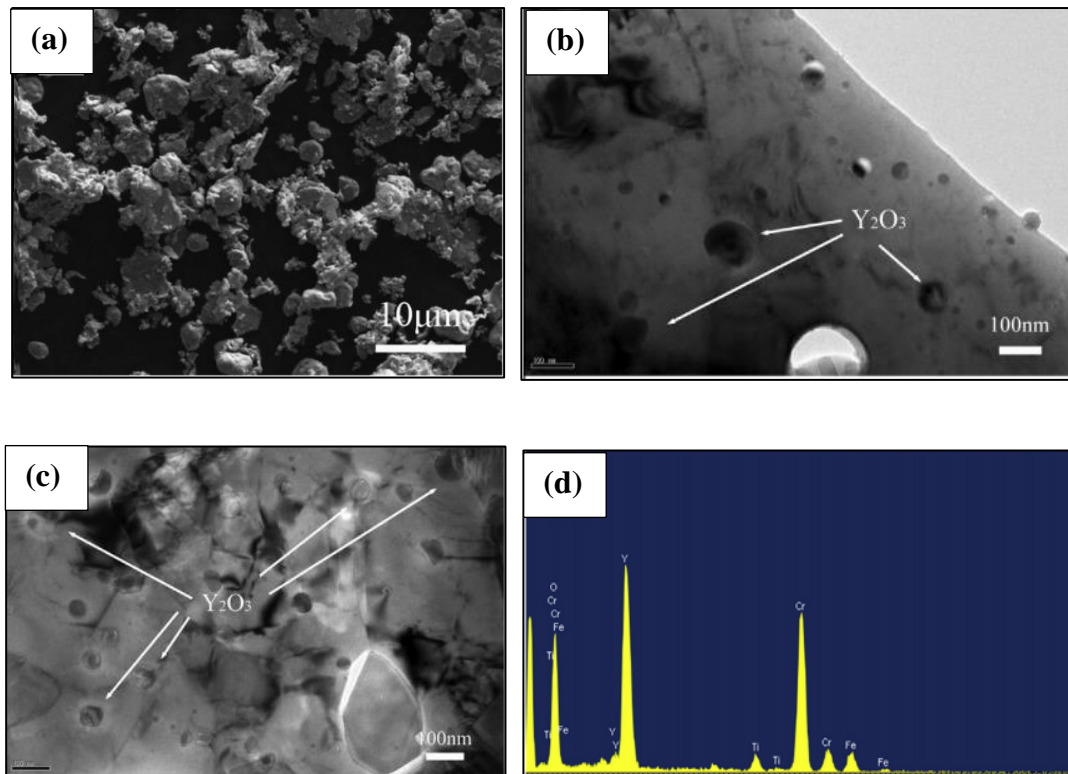
Figure 2.19: (a) SEM image of Powder particles, (b) TEM image showing oxide particles present on the matrix, (c) and (d) TEM imaging of the Y_2O_3 NP and corresponding EDS. (Courtesy of Elsevier) [55]

In the work by L. Toualbi et al. [14] the authors investigated Fe–9Cr–1W–0.2Ti–0.3Y_2O_3 alloy fabricated by MA and hot extrusion process. The alloy later passed through alternate heat treatment and cold rolling to be fabricated as SFR cladding tubes. The choice of lower tungsten content allows the control of the hardness levels all along the fabrication route without residual delta ferrite. In another work by L. Toualbi et al.[15], the author used Fe–9Cr–1W–0.1C–0.2Ti–0.3Y_2O_3 alloy produced by MA and hot extrusion process, followed by

cold rolling. Different cooling rates were used to understand the microstructure. Figure 2.20(a) shows the CCT diagram for the 9Cr steel and different cooling rates associated with it.
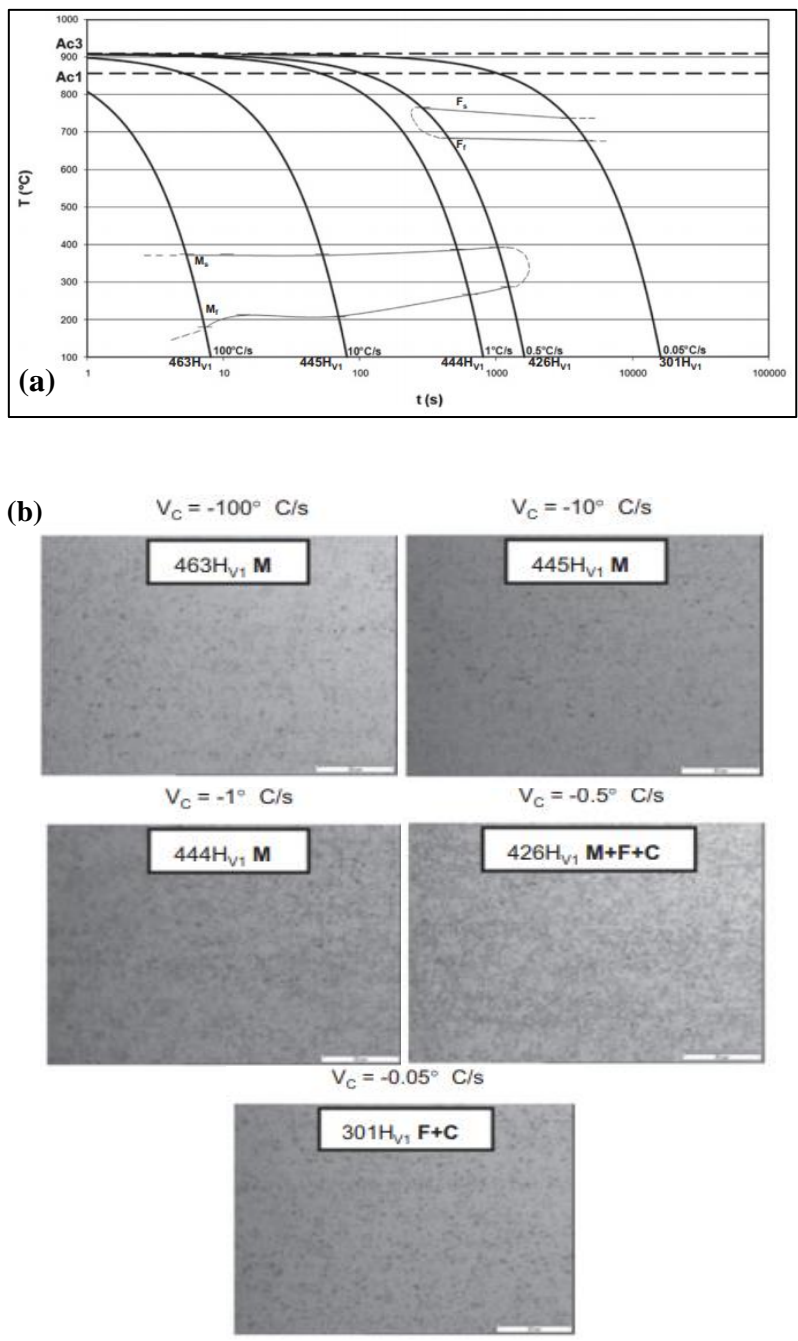
Figure 2.20: (a) CCT diagram of Fe-9Cr ODS alloy, (b) Different microstructure according to different cooling rates (Courtesy of Elsevier) [15]

Figure 2.21(a) and (b) shows the electron backscattered diffraction (EBSD) images (inverse pole figure) of mother tube after hot extrusion and annealing at 1050 ^{O}C for 30 min and 1250 ^{O}C for 30 min, respectively [15]. The grain sizes are seen to be around 2 µm for case (a) and around 5 µm for case (b).
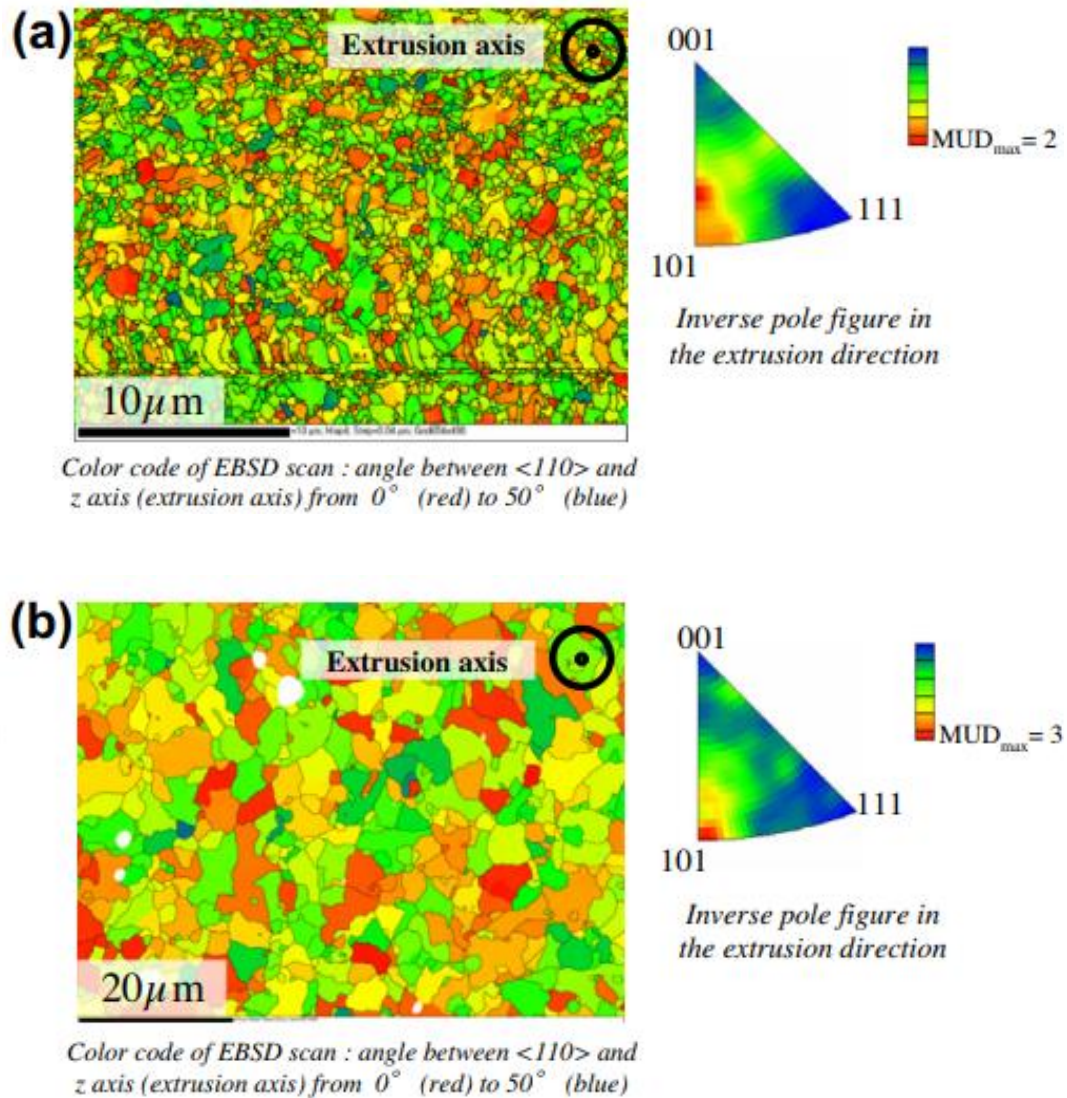
Figure 2.21: EBSD scans and related experimental inverse pole figure obtained on the transverse cross-section of mother tube after hot extrusion and annealing at (a) 1050 ^{O}C for 30 min and (b) 1250 ^{O}C for 30 min. (Courtesy of Elsevier) [15]

In the work by A. Chauhan et al. [56], the authors have produced Fe-9Cr ODS by MA and hot extrusion. Further heat treatment was performed on the sample to understand various properties of the material. The composition of the alloy used was Fe-9.1Cr-1.1W-0.3Ti-0.3Si-0.3Mn-0.2Ni-0.1C-0.25Y_2O_3. Figure 2.22 TEM imaging of the alloy. Figure 2.23(a) shows the EBSD map of the sample and Figure 2.23 (b) depicts the atom probe topography (APT) of the material.
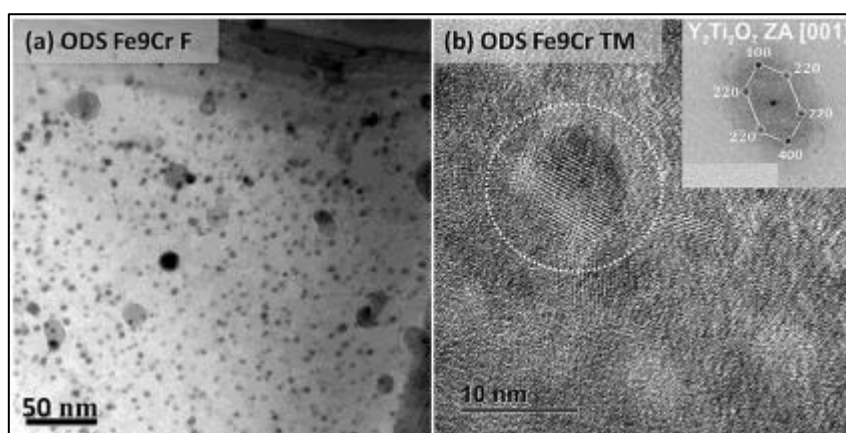
Figure 2.22 (a) TEM bright filed micrograph from as-received ODS Fe9Cr steel revealing region with homogeneous particle distribution. (b) High-resolution TEM micrograph from heat treated ODS Fe-9Cr steel shows a $Y_2Ti_2O_7$ particle lattice (encircled) with [001] zone axis having face centered cubic crystal structure and its corresponding fast Fourier transformation (FFT) power spectrum diffraction pattern in the inset. (Courtesy of Elsevier) [56]
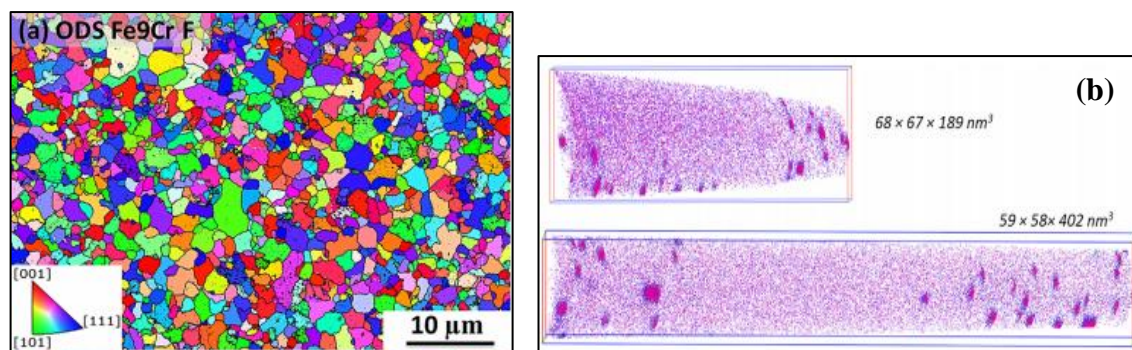
Figure 2.23 (a) Inverse pole figure maps obtained via EBSD for (a) as-received (step size: 72 nm) and (b) Two examples of 3D reconstructions of the ODS Fe9Cr extruded bar. Y is in red, TiO molecular ions are in purple and O is in blue. (Courtesy of Elsevier) [56]

2.6. Mechanical properties of sintered powder

A significant amount of work has been done on the evaluation of mechanical properties of Fe-9Cr ODS steel. Apart from microhardness, tensile testing, people have worked on understanding the strengthening mechanism caused due to the presence of oxide precipitates and the nanoclusters formed and present on the matrix. The strengthening mechanisms in ODS alloys include work hardening due to dislocation pile-up and dislocation – dislocation interactions, Hall – Petch strengthening due to grain refinement and grain boundary – dislocation interaction, solid solution due to lattice strain field. The presence of the oxide particles and a high number density of Y-Ti-O enriched nano clusters greatly helps in increasing the strength of the material by pinning the motion of the dislocation movement.

While there are different formalisms of predicting yield strength considering superposition of individual strengthening mechanisms, yield strength (σ_y) is often expressed using a linear summation relation [57]:

$$\sigma_y = \sigma_{P-N} + \sigma_{SS} + \sigma_{GB} + \sigma_P + \sigma_D \qquad (2.6)$$

where σ_{P-N} is the friction stress (Peierls-Nabarro stress), σ_{SS} is the solid solution strengthening, σ_{GB} is the grain boundary strengthening, σ_P is the precipitation strengthening and σ_D is the dislocation strengthening. Another way of expressing the total yield strength is based on the assumption that the obstacle strengths for dislocation strengthening and particle strengthening are of similar magnitude, and hence a non-linear additivity rule, as shown in Equation 4, should be used [58].

$$\sigma_y = \sigma_{P-N} + \sigma_{SS} + \sigma_{GB} + \sqrt{\sigma_P{}^2 + \sigma_D{}^2} \qquad (1.7)$$

The value of σ_{SS} is calculated using the following equation [59]:

$$\sigma_{SS} = \sum A_i\, C_i \qquad (2.8)$$

where A_i is the strengthening coefficient of alloying elements: and C_i is the wt% of the alloying elements.

The value of σ_{GB} is calculated using the well-known Hall-Petch equation [58]:

$$\sigma_{GB} = kd^{-\frac{1}{2}} \qquad (2.9)$$

where k is a constant and d is the average grain diameter as calculated.

The value of σ_P is calculated using the Orowan-Ashby equation [60]:

$$\sigma_p = \frac{0.538Gb\sqrt{f}}{dp}\ln\left(\frac{dp}{2b}\right) \qquad (2.10)$$

where G is the shear modulus, b is the Burgers vector, f is the volume fraction of the precipitates and d_p is the average diameter of the precipitates.

The strengthening (σ_D) due to dislocation density is obtained by the equation as follows [61]:

$$\sigma_D = \alpha MGb\sqrt{\rho} \qquad (2.11)$$

where α is a numerical constant which is usually taken as 0.3-0.6, M Taylor's factor (2.78 for BCC), G is the shear modulus, b the Burgers vector, and ρ the dislocation density as evaluated using the following equation [62, 63]:

$$\rho = 2\sqrt{3}\frac{\langle\xi^2\rangle^{0.5}}{d\times b} \qquad (2.12)$$

where $\langle\xi^2\rangle^{0.5}$ is the mean lattice strain obtained from the XRD pattern (by Williamson-Hall method) of the sintered specimen, d and b have already been defined.

According to the work by Q.X. Sun et al. [55], the authors found out that the yield strength and the ultimate tensile strength for the Fe–9Cr–1.5W–0.45Mn–0.1Ta–0.2V–0.01Si–0.2Ti–0.3Y$_2$O$_3$–0.1C ODS alloy processed via MA and hot extrusion are to be 725 and 734 MPa respectively. In the work by J.P. Wharry et al. [64], nanoindentation on Fe-9Cr ODS alloy shows hardness of almost 8.5 GPa at the top and with depth the hardness was almost 5.8 GPa. Haijian Xu et al. [65] have investigated the room temperature and high temperature tensile properties of Fe-9Cr-2W-0.3Y$_2$O$_3$ ODS alloy. This alloy was processed by MA and HIP process. Figure 2.24 shows the tensile stress-strain curve of the ODS alloy at 25 ^{O}C and at 700 ^{O}C. The ODS alloy shows that at 25 ^{O}C the UTS is around 1400 MPa and the total elongation is around 2.6%, whereas at 700 ^{O}C, the UTS turned out to be 210 MPa and the elongation increased to 16.5%.
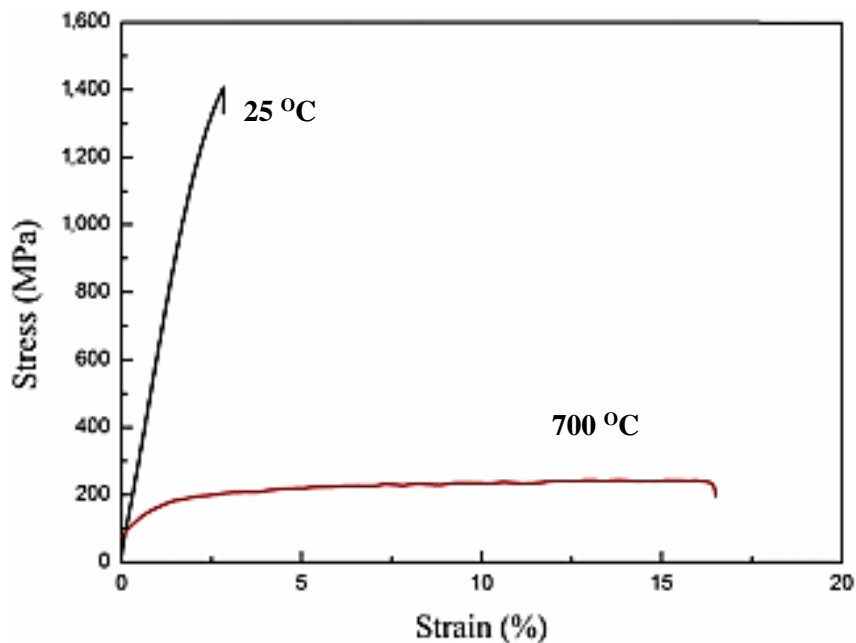
Figure 2.24. Tensile stress-strain curves of 9Cr-ODS steels at 25 ^{O}C and 700 ^{O}C (Courtesy to Elsevier) [65]

Figure 2.25 shows the contribution of different strengthening mechanism at 25 ^{O}C. The data obtained from theoretical calculation and that obtained from experimental value are almost equal [65].
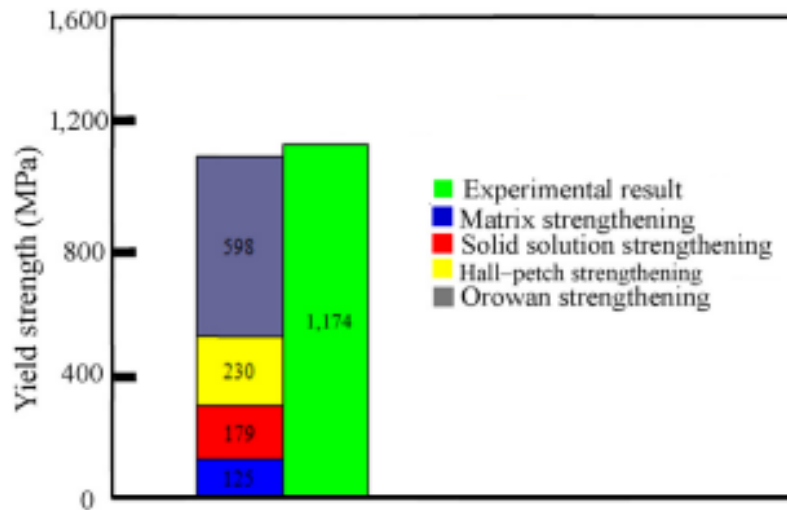
Figure 2.25. Contribution of different strengthening mechanism in 9Cr-ODS steels at 25 ^{O}C
(Courtesy to Elsevier) [65]

References

1. C. Suryanarayana, E. Ivanov, V.V. Boldyrev, The science and technology of mechanical alloying, Mater. Sci. Eng. A 304 (2001) 151.

2. W.D. Coolidge, Tungsten and method of making the same for use as filaments of incandescent electric amps and for other purposes, Patent # 6165412, U.S.A. (1913).

3. J.S. Benjamin, Dispersion strengthened superalloys by mechanical alloying, Metall. Trans. 1 (1970) 2943.

4. B. Reppich, On the attractive particle–dislocation interaction in dispersion-strengthened material, Acta Mater. 46 (1) (1998) 61.

5. A. Chauhan, D. Litvinov, Y. de Carlan and A. Jarir, Study of the deformation and damage mechanisms of a 9Cr-ODS steel: Microstructure evolution and fracture characteristics". Mater. Sci. and Eng. A. 658 (2016) 123.

6. UK-US Collaboration on Fossil Energy R&D Advanced Materials, http://us–uk.fossil.energy.gov/ (accessed on 12/31/2018).

7. G.R. Odette, M.J. Alinger, B.D. Wirth BD, Recent Developments in Irradiation-Resistant Steels, Annu. Rev. Mater. Res. 38 (2008) 471.

8. S. Ukai, Oxide Dispersion Strengthened Steels, https://www.slideshare.net /jufortunato84/oxide-dispersion-strengthened-steels?from_action=save (accessed 12/31/2018).

9. C. Topbasi, D. Kaoumi, A. T. Motta, M. A. Kirk, Microstructural evolution in NF616 (P92) and Fee9Cre0.1C-model alloy under heavy ion irradiation, J. Nucl. Mat. 466 (2015) 179.

10. S. Li, Y. Wang, X. Dai, F. Liu, J. Li and X. Wang, Evaluation of hardening behaviors in ion-irradiated Fe–9Cr and Fe–20Cr alloys by nanoindentation technique, J. Nucl. Mat. 478 (2016) 50.

11. K. Ono, K. Arakawa, H. Shibasaki, H. Kurata, I. Nakamichi and N. Yoshida, Release of helium from irradiation damage in Fe–9Cr ferritic alloy, J. Nucl. Mat. 329 (2004) 933.

12. K. Ono, H. Sasagawa, F. Kudo, M. Miyamoto and Y. Hidaka, Effects of tungsten on thermal desorption of helium from Fe–9Cr–2W ferritic alloy irradiated with low energy helium ions, J. Nucl. Mat. 417 (2011) 1026.

13. W. Eiichi, H. Akimichi, U. Kouji, K. Yasushi, T. Seiici and A. Kenji, Damage Structures and Mechanical Properties of High-Purity Fe–9Cr Alloys Irradiated by Neutrons, Mat. Trans. 41 (9) (2000) 1180.

14. L. Toualbi, C. Cayron, P. Olier, R. Logé and Y. de Carlan, Relationships between mechanical behavior and microstructural evolutions in Fe 9Cr–ODS during the fabrication route of SFR cladding tubes, J. Nucl. Mat. 442 (2013) 410.

15. L. Toualbi, C. Cayron, P. Olier, J. Malaplate, M. Praud, M.-H. Mathon, D. Bossu, E. Rouesne, A. Montani, R. Logé and Y. de Carlan, Assessment of a new fabrication route for Fe–9Cr–1W ODS cladding tubes, J. Nucl. Mat. 428 (2012) 47.

16. K. Rajan, T. Shanmugasundaram, V.S. Sarma, and B.S. Murty, Effect of Y_2O_3 on Spark Plasma Sintering Kinetics of Nanocrystalline 9Cr-1Mo Ferritic Oxide Dispersion-Strengthened Steels, Metall. Mater. Trans. A 44A (2013) 4037.

17. J.S. Benjamin, Mechanical Alloying, Sci. Amer. 234 (1976) 40.

18. J.S. Benjamin, E. Arzt and L. Schultz, New materials by mechanical alloying techniques, DGM Informationgesellschaft, (1989) 3.

19. J.S. Benjamin, Mechanical alloying – a perspective, Met. Powder Rep. 45 (1990) 122.

20. C. Suryanarayana, Mechanical alloying and milling, Prog. Mater. Sci. 46 (2001) 1.

21. P.Y. Lee, J.L. Yang and H.M. Lin, Amorphization behaviour in mechanically alloyed Ni—Ta powders, J. Mater. Sci. 33 (1998) 235.

22. H.K.D.H. Bhadeshia, Mechanically alloyed metals, Mater. Sci. Technol. 16 (2000) 1404.

23. P. Bala´z, Mechanochemistry in Nanoscience and Minerals Engineering, Springer-Verlag Berlin Heidelberg, 2008.

24. M. Brocq, B. Radiguet, S. Poissonnet, F. Cuvilly, P. Pareige and F. Legendre, Nanoscale characterization and formation mechanism of nanoclusters in an ODS steel elaborated by reactive-inspired ball-milling and annealing, J. Nucl. Mater. 409 (2) (2011) 80.

25. S. Pasebani, I. Charit, Y.Q. Wu, D.P. Butt and J.I. Cole, Mechanical alloying of lanthana-bearing nanostructured ferritic steels, Acta Mater. 61 (2013) 5605.

26. Blending and Mixing of the Powders & Compaction, Powder Metallurgy, Encyclopedia of Engineering, http://www.mechscience.com/blending-and-mixing-of-the-powders-compaction-powder-metallurgy/ (accessed 01/05/2019).

27. R.L. Coble, A model for boundary diffusion-controlled creep in polycrystalline materials, J. Appl. Phys. 34 (1963) 1679.

28. W. Sha and H.K.D.H. Bhadeshia, Modelling of recrystallisation in mechanically alloyed materials, Mater. Sci. Eng. A 223 (1997) 91.

29. Kennameta, Hot Isostatic Pressinh (HIP) Technology, https://www.kennametal. Com/hi/products/engineered-wear-solutions/engineered-components/hot-isostatic-pressing.html (accessed 01/06/2019).

30. H. Xu, Z. Lu, D. Wang and C. Liu, Effect of zirconium addition on the microstructure and mechanical properties of 15Cr-ODS ferritic Steels consolidated by hot isostatic pressing, Fusion Eng. Design 114 (2017) 33.

31. C-y Lu, Z. Lu and C-m Liu, Microstructure of nano-structured ODS CLAM steel by mechanical alloying and hot isostatic pressing, J. Nucl. Mat. 442 (2013) S148.

32. O. Guillon, Field-assisted sintering technology / spark plasma sintering: Mechanisms, Materials, and Technology Developments, Adv. Eng. Mat. 16 (2014) 830.

33. KU Leuven, SPS process modeling, https://www.mtm.kuleuven.be/Onderzoek/ Ceramics/research/sintering/spark-plasma (accessed 09/27/2018).

34. M. Suárez, A. Fernández, J.L. Menéndez, R. Torrecillas, H. U. Kessel, J. Hennicke, R. Kirchner and T. Kessel, Challenges and Opportunities for Spark Plasma Sintering: A Key Technology for a New Generation of Materials in Sintering Applications, 2013, http://dx.doi.org/10.5772/53706 (accessed 09/27/2018).

35. R. Orru, R. Licheri, A. M. Locci, A. Cincotti and G. Cao, Consolidation/synthesis of materials by electric current activated/assisted sintering, Mater. Sci. Eng. R 63 (2009) 127.

36. E. Olevsky, S. Y. Kandukuri and L. Froyen, Consolidation enhancement in spark-plasma sintering: Impact of high heating rates, J. Appl. Phys. 102 (2007) 114913.

37. A. G. Bloxam, An improved manufacture of electric incandescent lamp filaments from tungsten or molybdenum or an alloy, GB Patent 1906, No. 27,002.

38. K. Inoue, Method of electrically sintering discrete bodies, US Patent 1966, No. 3,250,892.

39. R. W. Boesel, M.I. Jackobson and I.S. Yoshioka, Spark sintering tames exotic P/M materials, Mater. Eng. 70 (1969) 32.

40. R. W. Boesel and C. G. Goetzel, Progress in spark sintering, Powder Metall. 3 (1) (1971) 38.

41. R. W. Boesel, Spark sintering- An unusual method (Spark sintering powder metallurgy using alternating and direct current plus pressure, discussing use in Be components production for aerospace applications), Metal. Prog. 99 (1971) 74.

42. C. G. Goetzel, Dispersion strengthened alloy: The possibilities for light metals, Mod. Dev. Powder Metall. 4 (1971) 425.

43. C. G. Goetzel, Tensile Properties of Titanium alloy Forgings made from Spark-Sintered Preforms, ASM Metals Eng. Quart. 11(2) (1971) 53.

44. C. G. Goetzel and V. S. Marchi, Electrically activated pressure-sintering (spark sintering) of titanium–aluminium–vanadium alloy powders, Powder Metall. Int. 3 (1971) 80.

45. Z.H. Zhang, Z.F. Liu, J.F. Lu, X.B. Shen, F.C. Wang and Y.D. Wang, The sintering mechanism in spark plasma sintering – Proof of the occurrence of spark discharge, Scripta. Mater. 81 (2014) 56.

46. R. Orru, R. Licheri, A.M. Locci, A. Cincotti and G. Cao, Consolidation/Synthesis of Materials by Electric Current Activated /Assisted Sintering, Mater. Sci. Eng. R 63 (2009) 127.

47. I. Bogomol, H. Borodianska, T. Zhao, T. Nishimura, Y. Sakka, P. Loboda, O. Vasylkiv, A dense and tough (B_4C–TiB_2)–B4C 'composite within a composite' produced by spark plasma sintering, Scripta Mater. 71 (2014) 17.

48. J.G. Santanach, A. Weibel, C. Estournès, Q. Yang, C. Laurent and A. Peigney, Spark plasma sintering of alumina: Study of parameters, formal sintering analysis and hypotheses on the mechanism(s) involved in densification and grain growth, Acta Mater. 59 (2011) 1400.

49. S.H. Lee, H.C. Oh, B.H. An and H.D. Kim, Ultra-low temperature synthesis of Al_4SiC_4 powder using spark plasma sintering, Scripta Mater. 69 (2013) 135.

50. R. Chaim, Densification mechanisms in spark plasma sintering of nanocrystalline ceramics, Mater. Sci. Eng. A 443 (2007) 25.

51. G. Molenat, L. Durand, J. Galy and A. Couret, Temperature Control in Spark Plasma Sintering: An FEM Approach, J. Metal.Vol. 2010, Article ID 145431.

52. J. Groza and A. Zavaliangos, Sintering activation by external electrical field, Mater. Sci. Eng. A 287 (2000) 171.

53. A.I. Raichenko, G.L. Burenkov and V.I. Leshchinsky, Theoretical analysis of the aluminium act of electric discharge sintering, Phys. Sinter. 5 (1976) 215.

54. H. Conrad, Thermally activated plastic flow of metals and ceramics with an electric field or current, Mater. Sci. Eng. A 322 (2002) 100.

55. Q.X. Sun et al., Development of 9Cr-ODS ferritic–martensitic steel prepared by chemical reduction and mechanical milling, J. Alloy. Comp. 598 (2014) 243.

56. A. Chauhan, F. Bergner, A. Etienne, J. Aktaa, Y. de Carlan, C. Heintze, D. Litvinov, M. Hernandez-Mayoral, E. Onorbe, B. Radiguet and A. Ulbricht, Microstructure

characterization and strengthening mechanisms of oxide dispersion strengthened (ODS) Fe-9%Cr and Fe-14%Cr extruded bars, J. Nucl. Mater. 495 (2017) 6.

57. D.R. Lesuer, C.K. Syn and O.D. Sherby, Influence of iron oxide particles on the strength of ball-milled iron, Mater. Trans. 47 (6) (2006) 1508.

58. A. Sittiho, V. Tungala, I. Charit, R. S. Mishra, Microstructure, mechanical properties and strengthening mechanisms of friction stir welded Kanthal APMT™ steel, J. Nucl. Mater. 509 (2018) 435.

59. S. Schmauder and C. Kohler, Atomistic simulations of solid solution strengthening of α-iron, Computational Mater. Sci. 50 (4) (2011) 1238.

60. M. A. Altuna, A. Iza-Mendia, I. Gutierrez, Precipitation strengthening produced by the formation in ferrite of Nb carbides, 3rd International Conference Thermomechanical Processing of Steels, organised by AIM; Padova, 10-12 September 2008.

61. W. Lia, H. Xu, X. Shac, J. Mengc, W. Wang, C. Kang, X. Zhanga and Z. Wang, Microstructural characterization and strengthening mechanisms of a 15Cr- ODS steel produced by mechanical alloying and Spark Plasma Sintering, Fusion Eng. And Design 137 (2018) 71.

62. K.G. Raghavendra, A. Dasgupta and P. Bhaskar, Synthesis and characterization of Fe-15 wt.% ZrO_2 nanocomposite powders by mechanical milling, Pow. Technol. 287 (2016) 190.

63. M. Mhadhbi, M. Khitouni, L. Escoda, J.J. Suñol and M. Dammak, Characterization of mechanically alloyed nanocrystalline Fe (Al): crystallite size and dislocation density, J. Nanomater. (2010) 8.

64. P. Wharry, M.J. Swenson, C.K. Dolph, K.H. Yano, Effect of irradiation on strengthening of a model Fe-9Cr oxide dispersion strengthened alloy, Conference Paper, Transactions of the American Nuclear Society, June 2016

65. Haijian Xu et al., Microstructure Refinement and Strengthening Mechanisms of a 9Cr Oxide Dispersion Strengthened Steel by Zirconium Addition, Nucl. Engg. Tech. 49 (2017) 178.

Chapter 3: Development of Fe-9Cr Alloy via High Energy Ball Milling and Spark Plasma Sintering

Arnab Kundu, Anumat Sittiho, Indrajit Charit, Brian Jaques and Chao Jiang

Abstract

Iron and chromium powders were mixed and mechanical alloyed via high energy ball milling for different time durations (2-20 h) to produce an alloy powder with a nominal composition of Fe-9Cr (wt%). The milled Fe-9Cr powders were analyzed using scanning electron microscopy (SEM), X-ray diffraction (XRD) and transmission electron microscopy (TEM) for understanding the impact of ball milling time on the characteristics of the milled powder. The optimized milled powder samples were then consolidated via spark plasma sintering (SPS) for different dwell times and temperatures. The density of the consolidated samples was measured following Archimedes principle and found to reach a maximum of 98%. Also, microstructural characterization of the SPSed samples were performed using optical microscopy, XRD, SEM, TEM and electron backscatter diffraction (EBSD). This study highlights the principles and importance of high energy ball milling and SPS of Fe-9Cr model alloy for the future development of more complex oxide dispersion strengthened alloys.

3.1. Introduction

High chromium (9-14 wt%) alloys are favourable for future sodium fast reactor fuel cladding materials [1-3], which require high radiation swelling resistance and resistance to attack from liquid sodium [4]. Oxide dispersion strengthened (ODS) steels based on Fe-(9-14)% Cr alloys are quite promising for such applications. Generally, the processing routes for making such steels involve mechanical alloying that incorporates rare earth oxides in the base Fe-Cr matrix. Mechanical alloying is a processing method that involves repeated fracturing, welding and re-fracturing of a mixture of powder particles, generally in a high-energy ball mill, to produce a controlled, extremely fine microstructure, which cannot be easily produced via conventional ingot metallurgy. The milled powder is then consolidated into bulk shapes and heat treated to obtain the desired characteristics [5]. It has been reported that the morphology, grain size distribution and contamination of the milled powders strongly depend on the process variables in mechanical alloying such as milling time, process control agent (PCA), ball to powder weight ratio (BPR), and milling atmosphere [6-12]. Mechanical alloying is a potential processing technique for producing nanocrystalline materials, amorphous and non-equilibrium phases. During this process, solid solubility significantly increases with increasing energy input. Solid solubility limit is determined by the ratio of intermixing (caused by shear forces) to the decomposition of the solid solution due to thermally activated jumps. If this ratio is very large, a fully random solid solution is achieved. Formation of nanostructures during milling has been established as the most effective mechanism to increase solid solubility due to higher fraction of atoms at the grain boundaries and enhanced (short circuit) diffusion path.

Sintering is the process of making objects from powder, by heating the material in a furnace below its melting point so that bonding takes place by diffusion of atoms. This leads to individual powder particles adhering to each other in a dense compact. Spark plasma sintering (SPS) is a thermal and pressure assisted compaction/sintering process. It is also known as field assisted sintering technique (FAST) [13] or pulsed electric current sintering (PECS) [14]. This process utilizes a combined action of a pulsed direct electrical current (DC) and pressure to perform high speed consolidation of powder. The direct way of heating allows very high heating rates, thus increasing densification due to enhanced diffusion [15-17]. It is regarded as a rapid sintering method in which the heating power is distributed over the volume of the powder compact and the heating power is dissipated exactly at the contact points of the powder particles. SPS systems offer many advantages over conventional techniques such as hot pressing (HP), hot isostatic pressing (HIP) or atmospheric furnaces, including ease of operation and accurate control of sintering energy resulting in lower temperature sintering and less time, and applicability to both electrically conductive and non-conductive materials.

Fe-9Cr alloy serves as a base matrix for Fe-9Cr ODS alloy that has attracted much interest [18-19]. Even though higher-Cr ODS alloys have better corrosion/oxidation resistance, they often suffer from thermal aging embrittlement and irradiation embrittlement because of alpha-prime phase formation [20]. However, Fe-9Cr based ODS steels are relatively free from such effects because of their lower Cr content. Thus, it is important to understand the Fe-9Cr matrix behaviour. However, Fe-9Cr alloy has been primarily made by casting [21,22], but less work has been reported on the powder metallurgy source Fe-9Cr alloy. In the work by Heintze *et al.* [23], they conducted high energy ball milling followed by SPS and HIP. However, the ball

milled powders for different milling durations were not fully analyzed and results were not interpreted. The present work was taken up to gain an understanding of the effects of ball milling and SPS on the microstructure and other morphological characteristics of the Fe-9Cr alloys. Furthermore, the effects of SPS temperature and time on the microstructural characteristics and microhardness of the sintered samples are investigated. Also, an effort has been made to understand the SPS process kinetics.

3.2. Material and Methods

Iron powder (99.9+% metal basis) of around 10 µm size and chromium powder (99.95% metal basis) of 50 µm size were weighed in ratio of 91:9 respectively and poured into a stainless steel vial along with stainless steel balls (milling medium) of 8 mm diameter under an argon atmosphere inside a glove box to prevent oxidation/contamination. No surfactant was added to the milling mixture. The ball to powder weight ratio was around 10:1 [24]. About half of the steel vial was empty after the mixture of powder and steel balls was poured. The filled vials were loaded in a shaker mill (SPEX 8000M) and milled for various durations (2, 5, 8, 10, 12, 15 and 20 h). The carbon and nitrogen content of the powders were found to be approximately 0.02 wt% and 0.024 wt%, respectively, estimated using combustion analysis. The chromium content of the 10 h ball milled sample was estimated by inductively coupled plasma (ICP) test and found to be 8.97 wt% which is essentially the target composition (i.e. 9 wt% Cr).

The milled powders were characterized in a Zeiss Supra 35 VP Field-Emission Gun Scanning Electron Microscope (FEG-SEM) to examine the powder size and morphology. X-ray diffraction (XRD) of ball milled powders were performed using Siemens 5000D

diffractometer with Cu $K\alpha$ X-ray radiation (wavelength of 0.1541 nm). Modifications such as adaptive smooth, $k\alpha_2$ Rachinger and background correction by Sonnerveld method were applied to XRD patterns using Powder–X software. Using the XRD data, lattice parameter of the milled powders was calculated based on the Nelson–Riley relation [25]. The crystallite size and lattice strain were evaluated using the Williamson–Hall equation [26]:

$$\beta_{hkl} = 0.94 \, (\lambda/L\cos\theta_{hkl}) + 4\varepsilon\tan\theta_{hkl} \qquad (3.1)$$

where β_{hkl} is the full width half maxima (FWHM) of the XRD peak, L is the crystallite size and ε is the lattice strain. Transmission electron microscopy was performed in JEOL 2010J transmission electron microscope at an accelerating voltage of 200 kV to study the inherent structure of the 10 h milled powder.

A Dr. Sinter Lab SPS-515S (SPS Syntex Inc., Kanagawa, Japan) available at the Center for Advanced Energy Studies (CAES), Idaho Falls, was used to consolidate the milled powder. A Tri-Gemini cylindrical graphite die with an inner diameter of 12.7 mm and outer diameter of 38 mm was used. The inner surface of the die was covered with a graphite foil with a thickness of 0.25 mm to facilitate sample removal. The milled powder was first cold-compacted inside the graphite die, and a 0.2 mm thick graphite foil was placed between the powder and punches. The die was wrapped in a 4 mm thick layer of graphite felt to minimize heat loss by thermal radiation. Degassing was performed by continually purging argon gas and pumping the chamber down to 7×10^{-3} Torr (9.33×10^{-7} MPa) and repeated at least thrice before starting the sintering process. The milled powder batches were heated in the vacuum chamber to four different temperatures (850 °C, 950 °C, 1000 °C and 1050 °C) at a rate of 100 °C/min and then held at each of the temperatures for 7, 15, 30 and 45 min. The temperature was monitored with a K-type thermocouple that was inserted through a hole in

the die. A constant uniaxial pressure of 80 MPa (~10 kN force) was applied to the milled powder during both heating and dwell time. The samples were then cooled to room temperature in the vacuum chamber by the rate of 50 ^{O}C/min. The final product was in the form of a disk with dimensions of 12.5 mm diameter and 4.8 mm thickness.

The density of the sintered samples was measured by Archimedes principle. The weight of the samples was taken in air and fully immersed condition in deionised water using an Ohaus Precision Balance (HRB-200). The density of deionised water (1 g/cm^3) and the density of air (0.0012 g/cm^3) at standard room temperature and pressure were used for density calculation.

The theoretical density of the sample was calculated based on the composition using the following equation:

$$\rho^{Th} = 100/(C_{Fe}/\rho_{Fe} + C_{Cr}/\rho_{Cr}) \qquad (3.2)$$

where, ρ^{Th} is the theoretical density of the sample, ρ_{Fe} is the density of iron (7.87 gm/cc), ρ_{Cr} is the density of chromium (7.19 gm/cc), C_{Fe} is the weight fraction of Fe (0.91) in the sample and C_{Cr} the weight fraction of Cr (0.09). The theoretical density of the sample was calculated to be around 7.81 gm/cc. The relative density was then estimated in terms of the percentage of theoretical density.

Vickers microhardness tests were performed on all the SPSed samples using a LECO 100M Microhardness Tester using a load of 0.5 kgf (~4.9 N) and a loading time of 15 s at 10 different random points. The same X-ray diffractometer and TEM was used for analysing the phase constituents and grain size of the SPSed samples. For preparing TEM specimens, an electro-jet polishing technique was used. A solution of CH_3OH – HNO_3 (80:20, by vol.%) was used as electrolyte at –40 ^{O}C and voltage of 25 V using a Fischione Model 110 Twin-Jet

Electropolisher. The electron backscatter diffraction (EBSD) analysis was carried out with Thermoscientific Quasor^{TM} system available in a Zeiss Supra 35 VP FEG-SEM at an accelerating voltage of 20 kV and at 70° tilt angle. The EBSD scanning used was used in resolution of 8 pixels × 8 pixels. A compression test was performed at room temperature under a strain rate of 10^{-3} s^{-1} using an Instron 5982 universal tester.

3.3. Results and Discussion

3.3.1. Microstructural Characteristics of the Milled Fe-9Cr Powders

The milled powder batches were examined by SEM. Figures 3.1(a), (b) and (c) show the representative SEM images of the powder samples ball milled for 2, 10 and 20 h, respectively. Powder size analysis revealed that the mean powder size decreased with increasing milling time as shown in Figure 3.2. Also, it can be noted that the powder size distribution became progressively narrower with increasing milling time. The process of ball milling involves mechanical collision process. Due to continuous collision of powder particles with the balls, the powder particles start breaking down into smaller particles. As seen in Figure 3.1(a), the mean powder size was around 50 ± 20 µm for the powder ball milled for 2 h. With increasing ball milling time, the time of collision and probability of collision also become greater. With continued deformation, the powder particles are work hardened and fracture by fatigue failure or impact fragmentation [27], and the mean powder size is found to be only 15 µm.
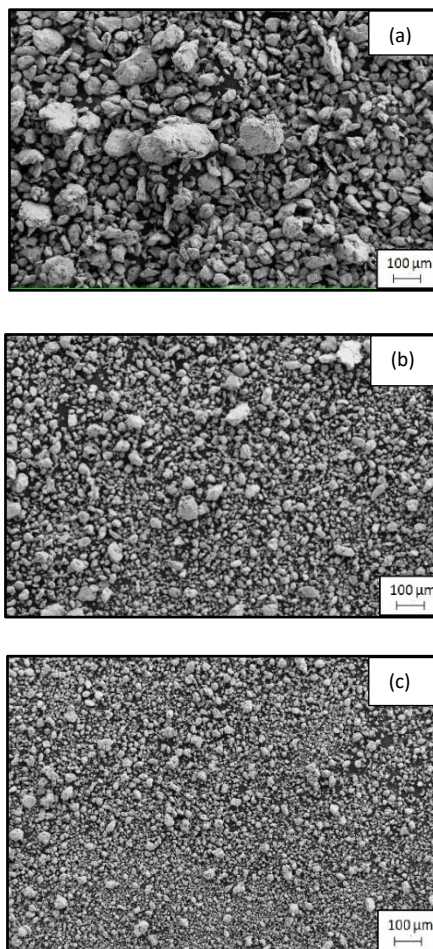
Figure 3.1. Secondary electron (SE) SEM images of Fe-9Cr powders ball milled for various time periods: (a) 2 h, (b) 10 h, and (c) 20 h
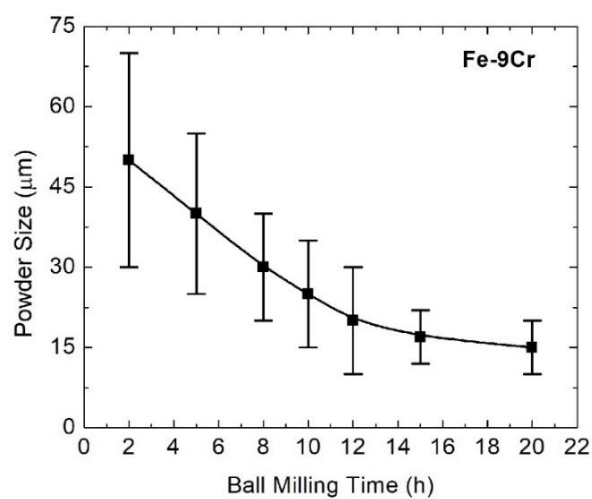
Figure 3.2. The variation of powder size as a function of milling time for Fe-9Cr powder batches (BPR of 10:1 and ball diameter of 8 mm)

Figure 3.3 shows the XRD patterns of the various milled powder samples. Prominent peaks are observed near the diffraction angles (2θ) of 44.91^0, 65.46^0 and 82.57^0. These peaks correspond to the planes {110}, {200} and {211} of BCC iron, respectively [28].
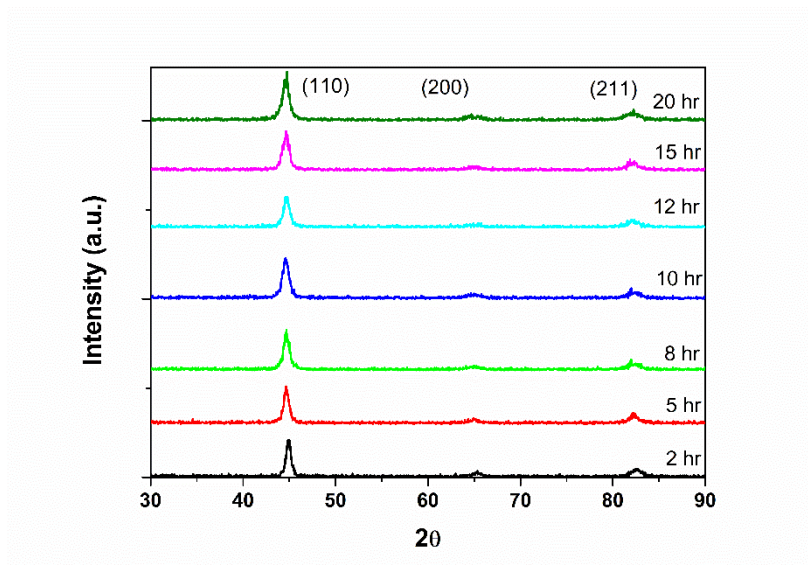
Figure 3.3. X-ray diffraction patterns of Fe-9Cr powder batches milled for various durations.

The broadening of the diffraction peaks is also observed with increasing milling time, which can be due to the introduction of strain and decrease of crystallite size of the powders [29]. A small shift of the peak positions toward the left is seen as a result of solid solutionizing of Cr in Fe and increasing strain during milling.

Table 3.1 shows the variation of lattice parameter, crystallite size and lattice strain with ball milling time. The lattice parameter on average is 2.880 ± 0.001 Å, which is in between that of iron (2.87 Å) and chromium (2.89 Å). According to Vegard's Law [30], the lattice parameter of Fe-9Cr solid solution should be to be 2.872 Å.

Table 3.1. Lattice parameter, crystallite size and lattice strain of the Fe-9Cr powder batches ball milled for various durations, as analyzed from the XRD data

Ball Milling Time (hr)	Lattice Parameter (Å)	Crystallite Size (nm)	Strain (%)
2	2.871 ± 0.001	14.91 ± 0.02	0.64 ± 0.02
5	2.882 ± 0.001	14.66 ± 0.02	0.66 ± 0.02
8	2.881 ± 0.001	13.27 ± 0.02	0.72 ± 0.02
10	2.891 ± 0.001	11.34 ± 0.02	0.84 ± 0.02
12	2.882 ± 0.001	10.97 ± 0.02	0.87 ± 0.02
15	2.872 ± 0.001	10.69 ± 0.02	0.89 ± 0.02
20	2.881 ± 0.001	10.35 ± 0.02	0.92 ± 0.02

The crystallite size analysis shows a decreasing trend with the increase in ball milling time. High energy ball milling is essentially a severe plastic deformation process. With increasing milling time, the process introduces progressively higher amount of strain leading to smaller crystallite size.

TEM imaging was done for the 10 hr-milled powder only. Figure 3.4(a) shows a bright field TEM image whereas its corresponding selected area diffraction (SAD) pattern of the milled powder is shown in Figure 3.4(b). The microstructure shows a uniform distribution of nanograins. The crystallite size measurement was done using the mean linear intercept method and average grain size was measured to be around 12 nm, which is consistent with the crystallite size determined from the XRD data (11.3 nm). The rings in the SAD pattern are from the ferritic matrix phase and no diffraction from any other phases is observed [31]. More or less equiaxed grain morphologies are observed in different regions of the microstructure, which is plausibly due to the very nature of local milling conditions that were not uniform throughout the whole volume of the material.
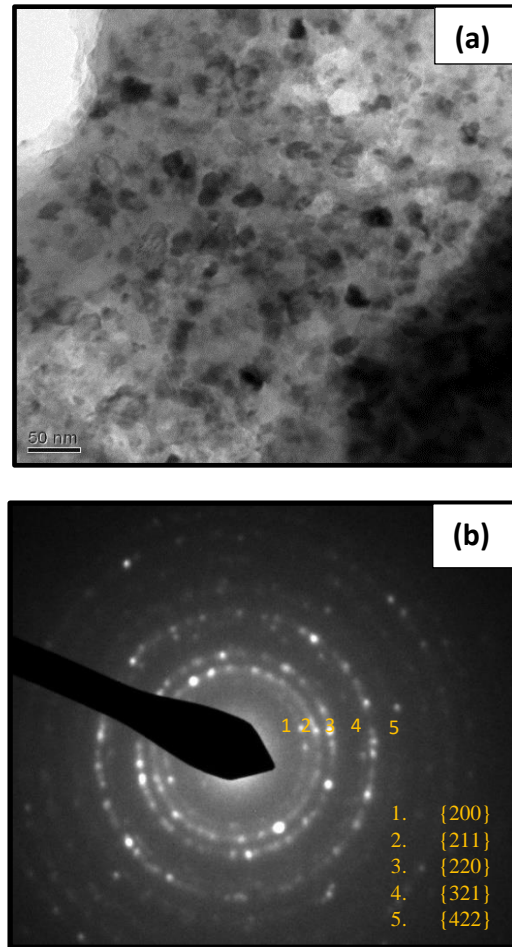
Figure 3.4. (a) TEM image of Fe-9Cr powder ball milled for 10 h and (b) SAD pattern of the same powder at 30 cm camera length.

3.3.2. Characteristics of Spark Plasma Sintered Fe-9Cr Samples

3.3.2.1. Evaluation of density and microhardness

In this section, results of SPSed Fe-9Cr alloys are presented and discussed. Figure 1.5(a) shows the variation of relative density of the sintered samples with sintering time. Sintering was conducted for four different dwell times (7, 15, 30 and 45 min) at a constant temperature of 950 °C and an applied pressure of 80 MPa. The results show that the density of the samples increases with increasing sintering time. The SPS process, being a diffusion controlled process, allows prolonged duration of diffusion to take place resulting in

progressive decrease in porosity. However, the effect of sintering temperature is found to be more effective on densification. Figure 3.5(b) shows the variation of relative density of the sintered samples as a function of sintering temperature. There are four sintering temperatures (850 $^{\circ}$C, 950 $^{\circ}$C, 1000 $^{\circ}$C and 1050 $^{\circ}$C), for which the sintering time and applied pressure were kept the same, i.e. 45 min and 80 MPa, respectively, for all temperatures. It can be noted that with increasing sintering temperature the relative density of the sintered specimens increases. Given the diffusional nature of sintering, higher temperature would lead to greater diffusivity leading to greater densification. The maximum density ($97.9 \pm 0.1\%$) is obtained for the sample sintered at 1000 $^{\circ}$C for 45 minutes.
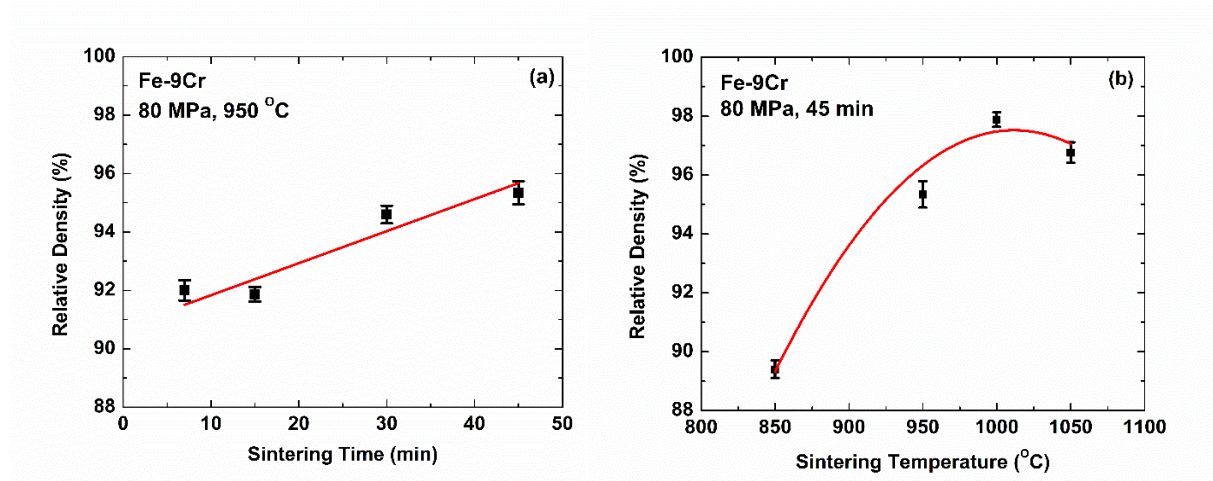
Figure 3.5. The variation of relative density of sintered samples with (a) sintering time and (b) sintering temperature

The microhardness of the samples was measured by Vickers microhardness testing. Figure 3.6(a) shows the variation of microhardness of the samples with sintering time. Four sintering times (7, 15, 30 and 45 min) all of which were done at a constant temperature of 950 $^{\circ}$C and 80 MPa pressure. Figure 3.6(b) shows the variation of microhardness of the sintered samples with sintering temperature. There are four sintering temperatures (850 $^{\circ}$C, 950 $^{\circ}$C, 1000 $^{\circ}$C and 1050 $^{\circ}$C), for which the sintering time and applied pressure were kept the same

at 45 min and 80 MPa, respectively, for all temperatures. The overall trend shows an increase

in microhardness with increasing sintering time and temperature.
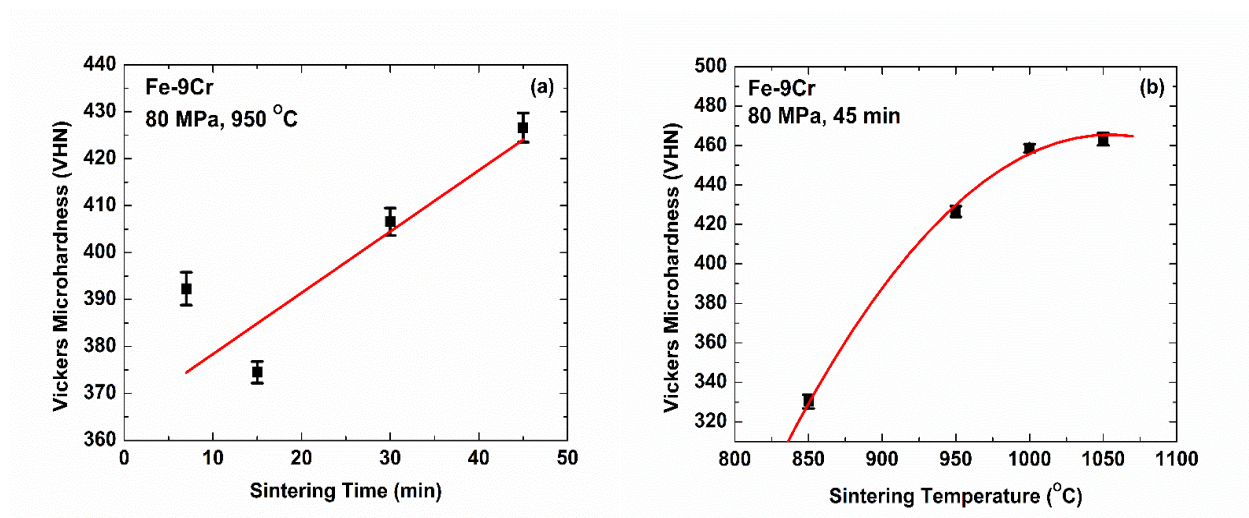
Figure 3.6. The variation of microhardness of SPSed Fe-9Cr samples as a function of (a)
sintering time and (b) sintering temperature

The reason behind is likely that with increasing sintering time, the powder gets more

time to get densified because of SPS is a diffusion-controlled process. Thus, with densification

(i.e. decrease in porosity) the hardness also increases. Sintering is an irreversible process in

which total free energy of the system is decreased by decreasing the total surface area; that is

replacing the solid-void interface with the solid-solid interfacial area.

3.3.2.2. *Microstructural characteristics of spark plasma sintered Fe-9Cr*

SEM imaging of the three Fe-Cr samples (10 h ball milled, sintered for 45 min at 950

°C, 1000 °C and 1050 °C) were performed. The specimen sintered at 850°C for 45 min yielded

low density and hardness compared to the others and so we did not do any SEM imaging for

that sample. Grain size analysis was done using mean linear intercept method. The average

grain size was found to be around 1.9±1.0 µm for the sample sintered at 950 °C, 2.0±1.0 µm

for the sample sintered at 1000 °C and 2.5±1.0 µm for the sample sintered at 1050 °C.

Therefore, it is clear that for the same sintering time only insignificant grain growth took place over the temperature range of 950 °C to 1050 °C. Figure 3.7 shows the secondary electron SEM images of the Fe-Cr processed (10 h ball milled 45 min and SPS at 950 °C, 1000 °C, and 1050 °C). Quantitative electron diffraction patterns at various points on the sample showed the presence of Cr in the range of 9 ± 1 wt%. So, we can conclude that there is relatively homogeneous distribution of chromium throughout the matrix.
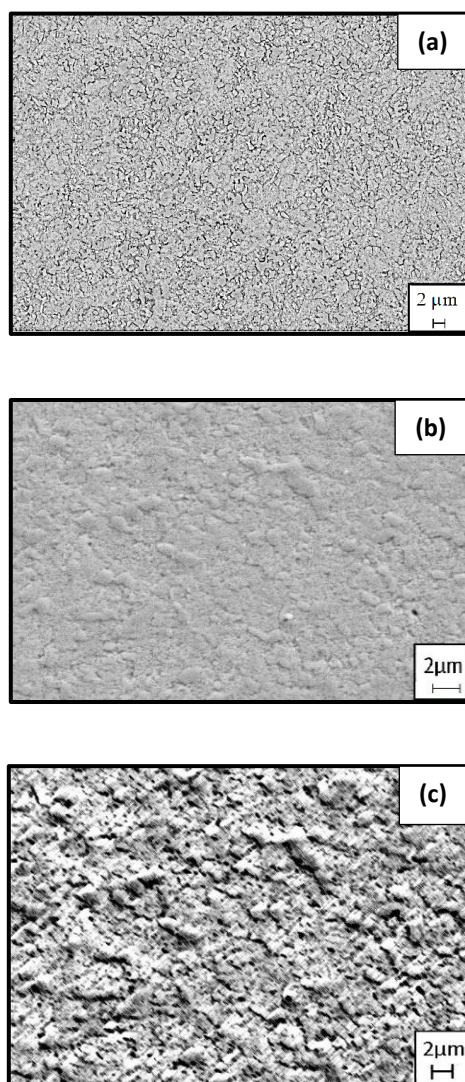
Figure 3.7. Secondary electron SEM images of Fe-9Cr alloy (10 h ball milled and SPSed for 45 min) at (a) 950 °C, (b) 1000 °C, and (c))1050 °C.

Figure 3.8(a) and 3.8(b) show the TEM images of the SPSed Fe-9Cr samples sintered at 950 ^{O}C and 1000 ^{O}C respectively. Importantly, both Fe-Cr samples appear to contain second phase particles even though a solution of Fe-9Cr is expected. It is clear that these particles were nucleated during ball milling and undergrown growth during the SPS process. This type of oxide particle formation is often seen because of the use of high energy ball milling. In other words, Fe-Cr alloy produced is not truly a single-phase solid solution alloy but is rather a Fe-Cr matrix with Cr-based oxide phases. Note that earlier studies on pure iron undergoing high energy ball milling and SPS reported formation of Fe-based oxide particles. Cr being more affinity for oxygen compared to Fe helped in forming Cr oxides [32]. Also, milling starting with constituent powder along with some oxygen present already on the surface and ingress of oxygen from the milling environment can help form the precursors of these oxides and they became clearly resolvable in TEM after SPS.
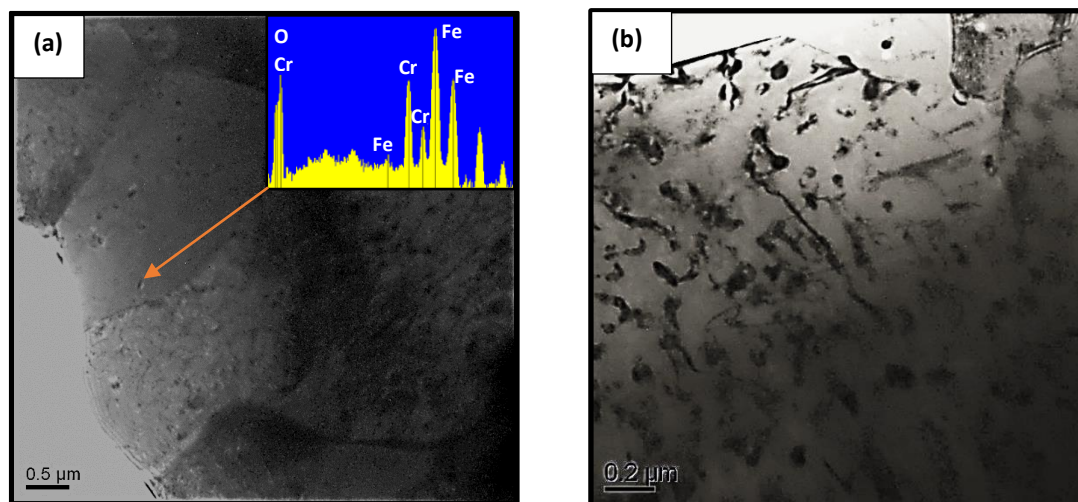
Figure 3.8. TEM image of the sample (10 h ball milled, 45 min sintering) at a SPS temperature of (a) 950 ^{O}C and (b) 1000 ^{O}C.

The relative density of the sample after 10 h ball milling, 45 min sintering at 1000 ^{O}C resulted in the highest relative density. The same process route is selected for further processing of Fe-9Cr alloy as this yielded the material with the highest densification, i.e.

lowest porosity. Further characterization of the Fe-9Cr alloy has been done on the samples produced by the aforementioned process route.

Figure 3.9 shows the XRD pattern of the SPSed sample (after 10 h ball milling and 45 min sintering at 1000 °C). The pattern shows the presence of ferrite that has a body centred cubic (BCC) structure.
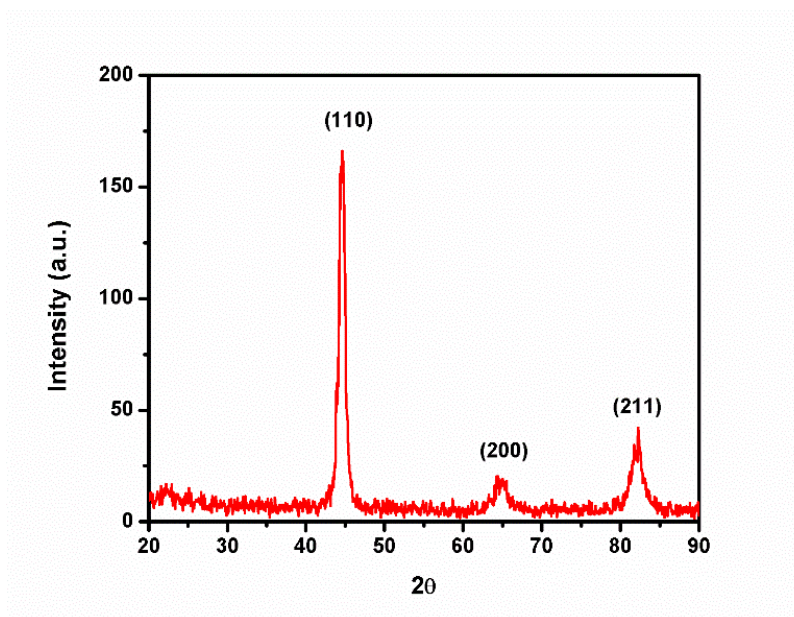
Figure 3.9. XRD pattern of the Fe-9Cr sample (10 h ball milled and sintered at 1000 °C for 45 min).

Figure 3.10 shows the inverse pole figure map of the Fe-9Cr alloy sintered at 1000 °C for 45 min under an applied pressure of 80 MPa. The orientation of the crystal planes in the normal direction i.e. the direction in which the pressure was applied during the SPS process. The grains are found to be randomly oriented throughout the matrix, which confirms that the SPS maintains fairly random texture [33].
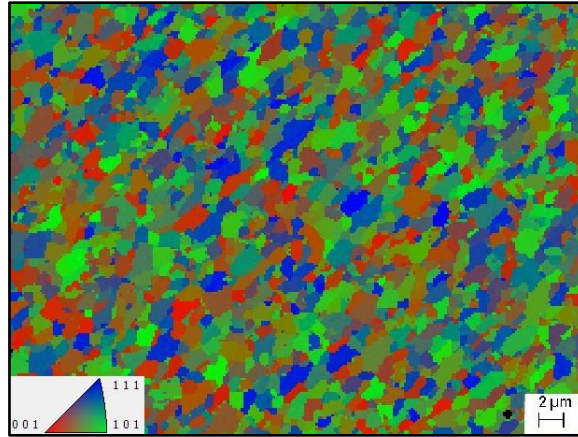
Figure 3.10. Inverse pole figure map of the Fe-9 Cr alloy sintered at 1000 $^{\circ}$C for 45 min under a pressure of 80 MPa

Figure 3.11 shows the direct pole figures of the Fe-9Cr alloy for three low index family

of planes. Here also it can be seen that there is no preferred texture in the material. The crystals

are randomly oriented in all the directions.
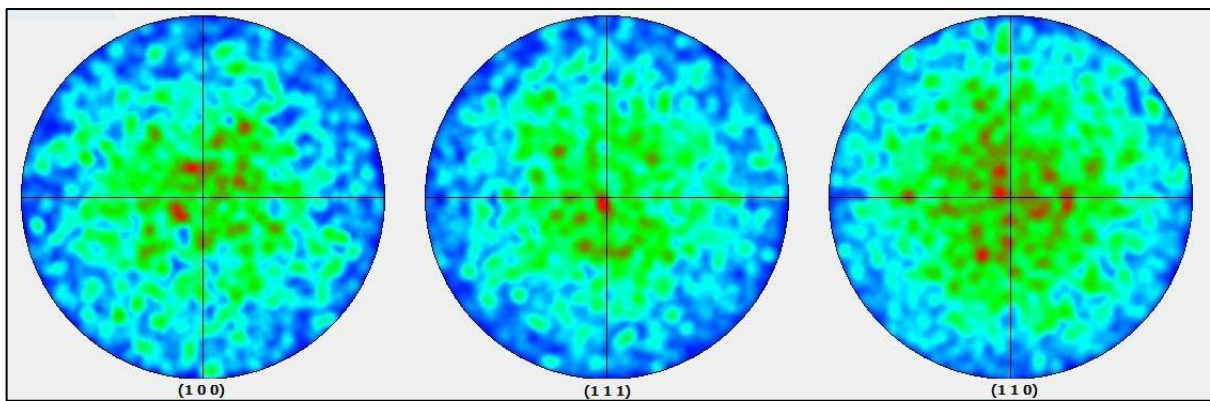
Figure 3.11. Pole figures of the Fe-9Cr alloy sample sintered at 1000 $^{\circ}$C for 45 min under 80 MPa pressure.

Figure 3.12(a) shows the grain boundary misorientation map of the same sample and

Figure 3.12(b) shows the corresponding grain boundary misorientation histogram. Both the

figures show that the low angle grain boundaries resolved is only a small fraction of the total

grain boundaries.
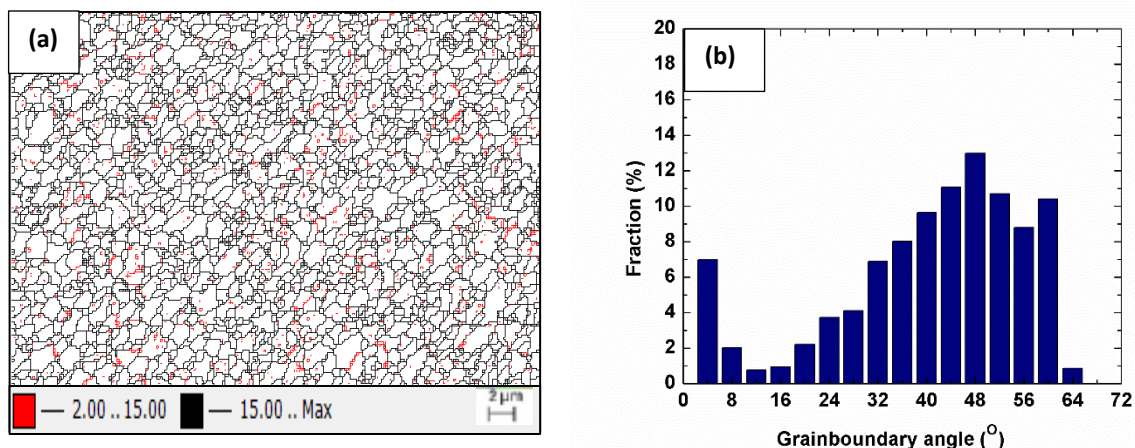
Figure 3.12. (a) Grain boundary misorientation maps, and (b) histogram showing grain boundary misorientation distributions of Fe-9Cr alloy sample sintered at 1000 ^{O}C for 45 min.

Figure 3.13 shows the grain size distribution of the same Fe-9Cr sample. The grain size was found to range from 0.4 µm to about 10 µm. However, the mean grain size was found to be about 2 µm, which is almost similar as measured from optical microscopy and TEM.
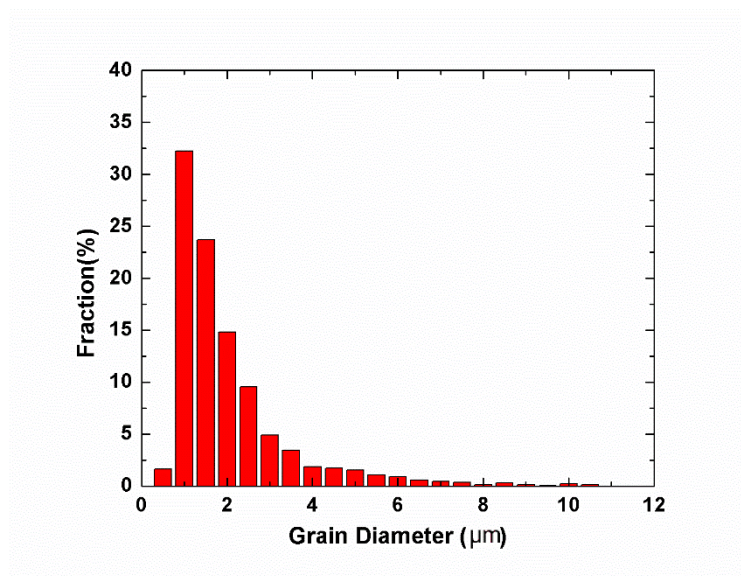
Figure 3.13. Grain size distribution of the Fe-9Cr alloy sample sintered at 1000 ^{O}C for 45 min under a pressure of 80 MPa.

3.3.2.3. Evaluation of compression properties of the spark plasma sintered Fe-9Cr alloy

True stress – true plastic strain curve of the SPSed Fe-9Cr in compression is shown in Figure 3.14. From the figure, the yield stress was determined to be about 642 MPa. Using Hollomon's equation, the strain hardening exponent was found to be 0.127.
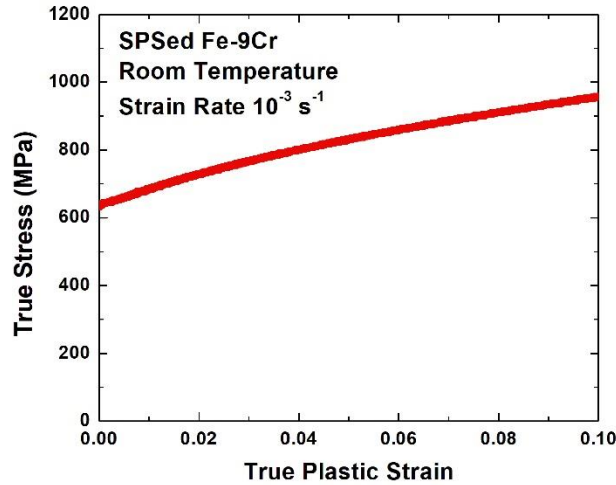
Figure 3.14. Compression stress-strain curve (true stress vs. true plastic strain) of the Fe-9Cr alloy sample sintered at 1000 $^{\circ}$C for 45 min under a pressure of 80 MPa.

3.3.3. Spark Plasma Sintering Kinetics

In order to understand the SPS kinetics, the model proposed by Young and Cutler [34] has been used. In their study, non-isothermal equations for volume and grain boundary diffusion have been modified. The equations represent the relationship between the shrinkage (*Y*) and diffusion coefficient (*D*), where *c* represents the heating ramp rate in units of K.s^{-1} [34]:

$$ln(YT\frac{dY}{dT}) = ln(\frac{2.63\gamma\Omega D_o^V}{ka^3c}) - \frac{Q_V}{RT} \qquad (3.3)$$

$$ln(Y^2T\frac{dY}{dT}) = ln(\frac{0.71\gamma b\Omega D_o^B}{ka^4c}) - \frac{Q_B}{RT} \qquad (3.4)$$

where Y is the linear shrinkage ($\Delta l/l_o$), Ω is the volume of vacancy (m³), γ is the surface energy (J/m²), D_V is the volume diffusion coefficient given by $D_V = D_0{}^V \exp(-Q_V /RT)$ (m².s⁻¹), bD_B is the product of the grain boundary thickness 'b' and grain boundary diffusion coefficient 'D_B' given by $bD_B = bD_0{}^B \exp(-Q_B /RT)$ (m³.s⁻¹), k is the *Boltzmann* constant (J/K), T is the temperature (K), a is the particle radius (m) and t is time (s). Q_V and Q_B are the activation energy for volume diffusion and grain boundary diffusion, respectively. The activation energies for volume diffusion and grain boundary diffusion can be obtained from the slope of the plots between ln ($YT(dY/dT)$) versus $1/T$ and ln ($Y^2T(dY/dT)$) versus $1/T$, respectively.

Figure 3.15 depicts the displacement profile curve of the SPSed sample. Constant heating
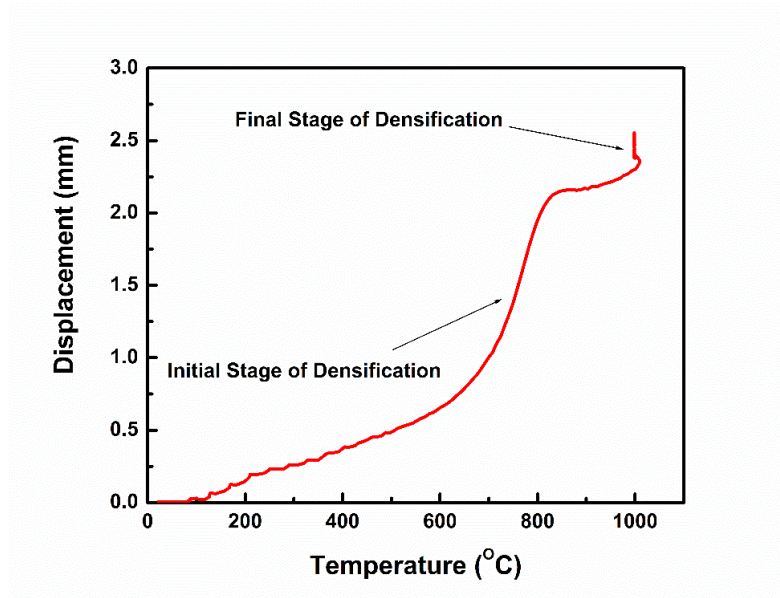
Figure 3.15. Displacement profile curve of the Fe-9Cr alloy sample sintered at 1000 °C for 45 min under a pressure of 80 MPa.

Rate has been used during the SPS process. The temperature at which densification begins (T_s) and the temperature at which maximum densification rate occurs (T_{max}) is calculated from the displacement curve and its first derivative respectively [35]. From the data obtained, it has

been seen that the densification starts around 600 ^{O}C and reaches the maximum densification rate at 825 ^{O}C which is close to the value obtained by previous studies [36].

From the slope of the ln (YT dY/dT) versus 1/T plots shown in Figure 3.16(a), the volume diffusion activation energy for the 10 h milled Fe-9Cr sintered at 1000 ^{O}C was estimated to be 130±3 kJ/mol. From the slope of the ln (Y^2T dY/dT) versus 1/T plots shown in Figure 1.16(b), the
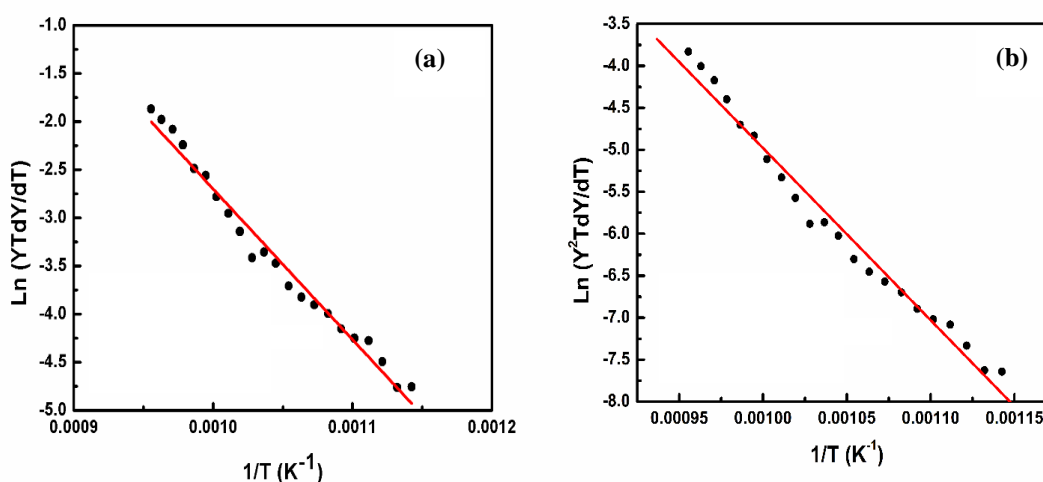
Figure 3.16. Activation energy profiles for (a) volume diffusion, and (b) grain boundary diffusion of the Fe-9Cr alloy sample sintered at 1000 ^{O}C for 45 min under a pressure of 80 MPa.

Grain boundary diffusion activation energy for the 10 h milled Fe-9Cr sintered at 1000 ^{O}C alloy was estimated to be 170±6 kJ/mol. The activation energy for volume diffusion and grain boundary diffusion of pure α–Fe was 251 and 174 kJ/mol, respectively [37]. The nanograin boundary diffusion for Fe powder was estimated to be 187 kJ/mol according to Lee et al. [38].

Considering the above scenario, one can hypothesize that in the initial phase of sintering i.e. from 600 to 850 ^{O}C, the grain boundary diffusion is found to be the dominant mechanism. The plausible reason for this could be preponderance of boundaries due to the nanocrystalline

crystallite size produced during high energy ball milling. However, during the process of SPS, various mechanisms can occur as reported in previous studies [15]. One of the reasons that in the initial phase, surface diffusion is the dominant mechanism because electric charge is concentrated mainly on the outer surface of the particles leading to capacitive nature between two nearby particles thus producing enough heat for the surface diffusion to take place. In the later stage when enough particles have joined with each other, then the volume diffusion or the lattice diffusion might come into play as depicted in Figure 3.15, but the exact mechanism of the final stage of densification is yet unknown.

3.3.4. Analysis of strengthening mechanisms

While there are different formalisms of predicting yield strength considering superposition of individual strengthening mechanisms, yield strength (σ_y) is often expressed using a linear summation relation [39]:

$$\sigma_y = \sigma_{P-N} + \sigma_{SS} + \sigma_{GB} + \sigma_P + \sigma_D \qquad (3.5)$$

where σ_{P-N} is the friction stress (Peierls-Nabarro stress), σ_{SS} is the solid solution strengthening, σ_{GB} is the grain boundary strengthening, σ_P is the precipitation strengthening and σ_D is the dislocation strengthening. Another way of expressing the total yield strength is based on the assumption that the obstacle strengths for dislocation strengthening and particle strengthening are of similar magnitude, and hence a non-linear additivity rule, as shown in Equation 4, should be used [40].

$$\sigma_y = \sigma_{P-N} + \sigma_{SS} + \sigma_{GB} + \sqrt{\sigma_P^2 + \sigma_D^2} \qquad (3.6)$$

In this study, the value of σ_{P-N} is for pure iron is taken as 50 Mpa [41]. The value of σ_{SS} is calculated using the following equation [42]:

$$\sigma_{SS} = \sum A_i\, C_i \qquad (3.7)$$

where A_i is the strengthening coefficient of alloying elements: C (5544 MPa/wt%) [43] and Cr (8.5 MPa/wt%) [44]. C_i is the wt% of the alloying elements.

The value of σ_{GB} is calculated using the well-known Hall-Petch equation [41]:

$$\sigma_{GB} = kd^{-\frac{1}{2}} \qquad (3.8)$$

where k is a constant (310 MPa $\mu m^{1/2}$) [41] and d is the average grain diameter as calculated (2 μm).

The value of σ_P is calculated using the Orowan-Ashby equation [45]:

$$\sigma_p = \frac{0.538 Gb\sqrt{f}}{dp} \ln\left(\frac{dp}{2b}\right) \qquad (3.9)$$

where G is the shear modulus of iron (60 GPa), b is the Burgers vector (0.248 nm), f is the volume fraction of the precipitates (0.05) and d_p is the average diameter of the precipitates (0.1 μm).

The strengthening (σ_D) due to dislocation density is obtained by the equation as follows [46]:

$$\sigma_D = \alpha MGb\sqrt{\rho} \qquad (3.10)$$

where α is a numerical constant which is usually taken as 0.3-0.6, M Taylor's factor (2.78 for BCC), G is the shear modulus, b the Burgers vector, and ρ the dislocation density (0.89×10^{14} m^{-2}) as evaluated using the following equation [47, 48]:

$$\rho = 2\sqrt{3}\frac{\langle\xi^2\rangle^{0.5}}{d\times b} \qquad (3.11)$$

where $\langle\xi^2\rangle^{0.5}$ is the mean lattice strain (0.013%) obtained from the XRD pattern (by Williamson-Hall method) of the sintered specimen, d and b have already been defined.

Summing up all the calculated individual strengthening mechanism contributions following Equations 3 and 4, the predicted yield strength values are included in Table 3.2 alongside estimated individual strengthening mechanism contributions. The predicted yield strength from the linear superposition rule came to be around 651 MPa, which is closer to the experimentally determined value (642 MPa). On the other hand, the non-linear superposition resulted in a yield strength value of 594 MPa.

Table 3.2. Comparison of predicted yield strength and experimental yield strength for the SPSed Fe-9Cr alloy

Strengthening Mechanisms	σ_{P-N} (MPa)	σ_{SS} (MPa)	σ_{GB} (MPa)	σ_p (MPa)	σ_D (MPa)	Predicted σ_y – Eqn. 3 (MPa)	Predicted σ_y – Eqn. 4 (MPa)	Calculated σ_y – Experimental (MPa)
Values	50	187	219	94	101	651	594	642

Previously, Fe-9Cr alloys have been made via casting [49]. The cast structures had microhardness of about 390 VHN although it had martensitic structure with precipitates MX, e.g., (Nb, Ta, V) (C, N), $M_{23}C_6$, Laves phase, and Z phase. But due to the very small grain size of sintered sample compared to that of the cast sample (around 20 µm), the hardness was higher than that of the cast Fe-9Cr alloy. Previous studies [50-52] have stated formation of martensitic structure when the alloy is cast and air cooled. Also, large elongated segregations of Cr rich phases have been seen in those alloys plausibly because of the very nature of

solidification involved in casting [53]. But after consolidation by SPS we could not find any such martensitic structure in the Fe-9Cr alloy processed as the material under study has a very low carbon content. EDS analysis has been done on various regions of the consolidated sample, but no Cr-rich segregations have been found. Fe-9Cr ODS steel has been prepared also by ball milling process and for 10 h and 20 h ball milling times, the mean powder size is close to what we achieved as reported by Xu et al. [54]. Heintze et al. [23] reported that Fe-9Cr ODS produced by a combined process of ball milling, SPS and hot isostatic pressing had a relative density level of 98.1%, which is quite close to 97.9% that we obtained by ball milling and SPS.

3.4. Conclusions

The main objective of this study was to understand the effect of ball milling and SPS on the microstructure and mechanical properties of Fe-9Cr model alloy. This work involved optimization of the ball milling and SPS parameters.

1. The high energy ball milling of Fe-9Cr samples for longer durations resulted in decreased powder size and nanocrystalline crystallite size in the milled powder.

2. With increasing milling time, the powder size decreases and the distribution of mean powder particle size also became narrower. The lattice parameter remains statistically the same and shows only slight variation with the ball milling time.

3. The SPS parameters also played a significant role in the consolidation process. With increasing sintering temperature, the diffusion process increased and at higher temperature the densification process became almost constant. Based on the parameters observed, a ball milling time of 10 h, and SPS temperature of 1000 $^{\circ}$C and sintering time of 45 min are found to be optimum for producing the Fe-9Cr alloy.

4. TEM analysis showed the presence of some Cr-based, fine oxide particles present in the matrix, which adds to the high hardness of the material due to particle hardening.

5. EBSD analysis showed no preferred texture throughout the optimized SPSed Fe-9Cr alloy.

6. Kinetics study indicates that in the initial stage of SPS grain boundary diffusion is the dominant mechanism for the consolidation process.

7. Analysis of strengthening mechanisms using linear superposition revealed the best correlation between the predicted yield strength and the experimentally obtained yield strength.

Data availability

The raw/processed data required to reproduce these findings cannot be shared at this time as the data also forms part of an ongoing study.

Acknowledgement

References

1. A. Kohyama, A. Hishinuma, D.S. Gelles, R.L. Klueh, W. Diets and K. Ehrich, Auger spectroscopy study of the stress enhanced impurity segregation in a Cr-Mo-V steel, J. Nucl. Mater. 138 (1996) 233.

2. F.A. Garner, M.B. Toloczko and B.H. Sencer, Comparison of swelling and irradiation creep behaviour of fcc-austenitic and bcc-ferritic/martensitic alloys at high neutron exposure, J. Nucl. Mater. 276 (2000) 123.

3. R.L. Klueh and D.H. Harries, High-chromium ferritic and martensitic steels for nuclear applications, ASTM, Book 3, July 1, 2001.

4. B. Raj, S. L. Mannan, P. Rao and M. D. Mathew, Development of fuels and structural materials for fast breeder reactors, Sadhana 7 (2002) 527.

5. C. Suryanarayana, Mechanical alloying and milling, Prog. Mater. Sci. 46 (2001) 1.

6. C.L. Chen and Y. M. Dong, Effect of mechanical alloying and consolidation process on microstructure and hardness of nanostructured Fe–Cr–Al ODS alloys, Mater. Sci. Eng. A 528 (2011) 8374.

7. C. Suryanarayana, E. Ivanov and V.V. Boldyrev, Mater. Sci. Eng. A 304 (2001) 151.

8. J.B. Fogagnolo, F. Velasco, M.H. Robert and J.M. Torralba, The science and technology of mechanical alloying, Mater. Sci. Eng. A 342 (2003) 131.

9. M. Zawrah and L. Shaw, Microstructure and hardness of nanostructured Al/Fe/Cr/Ti alloys through mechanical alloying, Mater. Sci. Eng. A 355 (2003) 37.

10. R. Juarez, J.J. Sunol, R. Berlanga, J. Bonastre and L. Escoda, The effects of process control agents on mechanical alloying behaviour of a Fe–Zr based alloy, J. Alloys Compd. 434 (2007) 472.

11. Z. Oksiuta and N. Baluc, Effect of mechanical alloying atmosphere on the microstructure and Charpy impact properties of an ODS ferritic steel, J. Nucl. Mater. 386 (2009) 426.

12. X.L. Wang, G.F. Wang and K.F. Zhang, Effect of mechanical alloying on microstructure and mechanical properties of hot-pressed Nb–16Si alloys, Mater. Sci. Eng. A 527 (2010) 3253.

13. O. Guillon, Field-assisted sintering technology / spark plasma sintering: Mechanisms, Materials, and Technology Developments, Adv. Eng. Mat. 16 (2014) 830.

14. KU Leuven, SPS process modeling, https://www.mtm.kuleuven.be/Onderzoek/Ceramics/research/sintering/spark-plasma (accessed 09/27/2018).

15. M. Suárez, A. Fernández, J.L. Menéndez, R. Torrecillas, H. U. Kessel, J. Hennicke, R. Kirchner and T. Kessel, Challenges and Opportunities for Spark Plasma Sintering: A Key Technology for a New Generation of Materials in Sintering Applications, 2013, http://dx.doi.org/10.5772/53706 (accessed 09/27/2018).

16. R. Orru, R. Licheri, A. M. Locci, A. Cincotti and G. Cao, Consolidation/synthesis of materials by electric current activated/assisted sintering, Mater. Sci. Eng. R 63 (2009) 127.

17. E. Olevsky, S. Y. Kandukuri and L. Froyen, Consolidation enhancement in spark-plasma sintering: Impact of high heating rates, J. Appl. Phys. 102 (2007) 114913.

18. L. Toualbi, C. Cayron, P. Olier, J. Malaplate, M. Praud, M.-H. Mathon, D. Bossu, E. Rouesne, A. Montani, R. Logé and Y. de Carlan, Assessment of a new fabrication route for Fe–9Cr–1W ODS cladding tubes, J. Nucl. Mater. 428 (2012) 47.

19. S. Noh, A. Kimura and T. K. Kim, Diffusion bonding of 9Cr ODS ferritic/martensitic steel with a phase transformation, Fusion Eng. Des. 89 (2014) 1746.

20. S.A. Briggs, P.D. Edmondson, K.C. Littrell, Y. Yamamoto, R.H. Howard, C.R. Daily, K.A. Terrani, K. Sridharan and K.G. Field, A combined APT and SANS investigation of α' phase precipitation in neutron-irradiated model FeCrAl alloys, Acta Mater. 129 (2017) 217.

21. S. Li, Y. Wang, X. Dai, F. Liu, J. Li and X. Wang, Evaluation of hardnening behaviors in ion-irradiated Fe-9Cr and Fe-20Cr alloys by nanoindentation technique, J. Nucl. Mater. 478 (2016) 50.

22. K. Ono, K. Arakawa, H. Shibasaki, H. Kurata, I. Nakamichi and N. Yoshida, Release of helium from irradiation damage in Fe-9Cr ferritic alloy, J. Nucl. Mater. 329 (2004) 933.

23. C. Heintze, M. Hernandez-Mayoral, A. Ulbricht, F. Bergner, A. Shariq, T. Weissgarber and H. Frelinghaus, Nanoscale characterization of Fe-9%Cr model alloys compacted by spark plasma sintering, J. Nucl. Mater. 428 (2012) 139.

24. M. Zakeri, M. Ramezani and A. Nazari, Prediction of the mean grain size of MA-synthesized nanopowders by artificial neural networks, Mater. Res. 15 (2012) 6.

25. J.B. Nelson and D.P. Riley, An experimental investigation of extrapolation methods in the derivation of accurate unit-cell dimensions of crystals, Proc. Phys. Soc. 57 (1945) 160.

26. G.K. Williamson and W.H. Hall, X-ray line broadening from filed aluminium and wolfram, Acta Metall. 1 (1953) 22.

27. Y. Zhenhua, X. Weihao, Y. Ming and P. Qianyun, Effects of mechanical alloying on characteristics of nanocrystalline Fe-Cr-W-Ti-Y_2O_3 powders, J. Nucl. Mater. 403 (2010) 198.

28. X.T.A. Chu, B.N. Ta, L.T.H. Ngo, M.H. Do, P.X. Nguyen and D.N.H. Nam, Microwave Absorption Properties of Iron Nanoparticles Prepared by Ball-Milling, J. Electron. Mater. 45 (2016) 2311.

29. R.K. Khatirkar and B.S. Murty, Structural changes in iron powder during ball milling, Mater. Chem. Phys. 123 (2010) 247.

30. A.R. Denton and N.W. Ashcroft, Vegard's law, Phys. Rev. A. 43 (6) (1991) 3161.

31. S. Pasebani, I. Charit, D.P. Butt and J.I. Cole, A Preliminary study on the development of La_2O_3-bearing nanostructured ferritic steels, J. Nucl. Mater. 434 (2013) 282.

32. B. Arh and F. Tehovnik, The oxidation and reduction of chromium during the elaboration of stainless steels in an electric arc furnace, Mater. And Technol. 41 (5) (2007) 203.

33. B.Srinivasarao, K.Oh-ishi, T.Ohkubo and K.Hono, Bimodally grained high-strength Fe fabricated by mechanical alloying and spark plasma sintering, Acta Mater. 57 (11) (2009) 3277.

34. W.S. Young and I.B. Cutler, Initial sintering with constant rates of heating, J. Am. Ceram. Soc. 53 (1970) 659.

35. J. Guyon, A. Hazotte, J.P. Monchoux and E. Bouzy, Effect of powder state on spark plasma sintering of TiAl alloys, Intermetallics 34 (2013) 94.

36. S. Pasebani, I. Charit, D. P. Butt, J. I. Cole, Y. Wu and J. Burns, Sintering Behavior of Lanthana-Bearing Nanostructured Ferritic Steel Consolidated via Spark Plasma Sintering, Adv. Engg. Mat. 18 (2) (2016) 324.

37. H.J. Frost, and M.F. Ashby: Fundamental aspects of structural alloy design, Plenum, 1977.

38. J.S. Lee, J.P. Choi and G.Y. Lee, Consolidation of Hierarchy-Structured Nanopowder Agglomerates and Its Application to Net-Shaping Nanopowder Materials, Mater. 6 (2013) 4046.

39. D.R. Lesuer, C.K. Syn and O.D. Sherby, Influence of iron oxide particles on the strength of ball-milled iron, Mater. Trans. 47 (6) (2006) 1508.

40. A. Sittiho, V. Tungala, I. Charit and R. S. Mishra, Microstructure, mechanical properties and strengthening mechanisms of friction stir welded Kanthal APMT™ steel, J. Nucl. Mater. 509 (2018) 435.

41. W.C. Leslie, Iron and its dilute substitutional solid solutions, Metall. Trans. 3 (1) (1972) 5.

42. S. Schmauder and C. Kohler, Atomistic simulations of solid solution strengthening of α-iron. Computational Mater. Sci. 50 (4) (2011) 1238.

43. G.E. Totten, L. Xie and K. Funatani, Handbook of Mechanical Alloy Design, New York, 2003.

44. J. Wang, W. Yuan, R.S. Mishra and I. Charit, Microstructure and mechanical properties of friction stir welded oxide dispersion strengthened alloy, J. Nucl. Mater. 432 (1) (2013) 274.

45. M. A. Altuna, A. Iza-Mendia and I. Gutierrez, Precipitation strengthening produced by the formation in ferrite of Nb carbides, 3rd International Conference Thermomechanical Processing of Steels, organised by AIM; Padova, 10-12 September 2008.

46. W. Lia, H. Xu, X. Shac, J. Mengc, W. Wang, C. Kang, X. Zhanga and Z. Wang, Microstructural characterization and strengthening mechanisms of a 15Cr- ODS steel produced by mechanical alloying and Spark Plasma Sintering, Fusion Eng. And Design 137 (2018) 71.

47. K.G. Raghavendra, A. Dasgupta and P. Bhaskar, Synthesis and characterization of Fe-15 wt.% ZrO2 nanocomposite powders by mechanical milling, Powd. Technol. 287 (2016) 190.

48. M. Mhadhbi, M. Khitouni, L. Escoda, J.J. Suñol and M. Dammak, Characterization of mechanically alloyed nanocrystalline Fe(Al): crystallite size and dislocation density, J. Nanomater. (2010) 8.

49. O. Boshko, O. Nakonechna, N. Belyavina, M. Dashevskyi and S. Revo, Nanocrystalline Fe–C composites obtained by mechanical alloying of iron and carbon nanotubes, Adv. Powder Technol. 28 (2017) 964.

50. Z. Hou, Study of precipitation in martensitic Fe-C-Cr alloys during tempering: Experiments and modelling, https://www.diva-portal.org/smash/get/diva2:866846/FULLTEXT01.pdf, (accessed 09/27/2018).

51. T. Shrestha, S. F. Alsagabi, I. Charit, G. P. Potirniche and M. V. Glazoff, Effect of heat treatment on microstructure and hardness of Grade 91 Steel, Metals 5 (2015) 131.

52. S. H. Babu, G. Amarendra, R. Rajaraman and C.S. Sundar, Microstructural characterization of ferritic/martensitic steels by positron annihilation spectroscopy, J. Phys. Conference Series 443 (2013) 012010.

53. V. Kuksenko, Model oriented irradiation experiments in Fe-Cr model alloys, Mater. Sci., Université de Rouen, 2011.

54. H. Xua, Z. Lua, D. Wanga and C. Liua, Microstructural evolution in a new Fe based ODS alloy processed by mechanical alloying, Nucl. Mater. And Energy 7 (2016) 1.

Chapter 4: Microstructural Evolution and Corrosion Behavior of Spark Plasma Sintered Fe-Cr Based Alloys: Effect of Cr Concentration

Arnab Kundu, Nikunja Shrestha, Alen Korjenic, Krishnan S. Raja and Indrajit Charit

Abstract

Iron (Fe) and chromium (Cr) powders at various concentrations of Cr (6, 9, 12 and 14 wt%) were mechanically alloyed via high energy ball milling for 10 h. The milled Fe-Cr alloy powders were analyzed using scanning electron microscopy (SEM) and X-ray diffraction (XRD) for understanding the impact of varying chromium content on the characteristics of the milled powder. The powder samples were then consolidated via spark plasma sintering (SPS) at 1000 ^{O}C for 45 min at 80 MPa pressure. The density of the consolidated samples was measured and found to reach a maximum of 98%. Microstructural characterization of the SPSed samples were performed using SEM and XRD. Electrochemical corrosion tests were performed on SPSed samples in 0.5M H_2SO_4, 0.05M NaH_2PO_4 and 1M NaOH solutions using potentiodynamic polarization, electrochemical impedance spectroscopy (EIS) and Mott Schottky (MS) analysis. The corrosion behavior of the SPSed materials was compared with that of a wrought HT9 steel (12Cr based ferritic-martensitic steel). The work presented here is a comparative study of microstructural and corrosion behavior between the different SPSed Fe-Cr model alloys and wrought HT9 steel.

Keywords: Spark plasma sintering; Fe-Cr; XRD; Corrosion; EIS; Mott-Schottky

4.1. Introduction

High chromium (9-14 wt%) containing steels have potential for structural and fuel cladding applications in advanced nuclear reactors including sodium cooled fast reactors [1-3], which require high radiation swelling resistance and resistance to attack from liquid sodium [4]. Oxide dispersion strengthened (ODS) steels based on Fe- (9-14) wt% Cr alloys are also promising for such applications. The processing routes of such steels involve mechanical alloying that incorporates rare earth oxides such as yttrium oxide in the base Fe-Cr matrix. Mechanical alloying is a processing method that involves repeated fracturing, welding and re-fracturing of a mixture of powder particles, generally in a high-energy ball mill, to produce a controlled, extremely fine microstructure, which cannot be easily produced via conventional ingot metallurgy. The milled powder is then consolidated into bulk shapes and heat treated to obtain the desired characteristics [5]. It has been reported that the morphology, grain size distribution and contamination of the milled powders strongly depend on the process variables in mechanical alloying such as milling time, process control agent (PCA), ball to powder weight ratio (BPR), and milling atmosphere [6-12]. Mechanical alloying is a potential processing technique for producing nanocrystalline materials, amorphous and non-equilibrium phases. During this process, solid solubility significantly increases with increasing energy input. Solid solubility limit is determined by the ratio of intermixing (caused by shear forces) to the decomposition of the solid solution due to thermally activated jumps. If this ratio is very large, a fully random solid solution is achieved. Formation of nanostructures during milling has been established as the most effective

mechanism to increase solid solubility due to higher fraction of atoms at the grain boundaries and enhanced (short circuit) diffusion path.

Spark plasma sintering (SPS) is compaction/sintering process that utilizes a combined action of a pulsed direct electrical current (DC) and pressure to perform fast consolidation of powder. The direct way of heating allows high heating rates, thus increasing densification due to enhanced diffusion [13-15]. It is regarded as a rapid sintering method in which the heating power is distributed over the volume of the powder compact and the heat is dissipated exactly at the locations in the microscopic scale, where energy is required for the sintering process, mainly at the contact points of the powder particles. SPS systems offer many advantages over conventional systems using hot pressing (HP), hot isostatic pressing (HIP) or atmospheric furnaces, including ease of operation and accurate control of sintering energy resulting in lower temperature sintering and less time, and applicability to both electrically conductive and non-conductive materials.

The nature of the passive oxide film on as cast iron has been the subject of investigation since Schonbein and Faraday [16] first developed the theory of protective oxide skin. Recent studies have shown that the passivity is due to the presence of a thin oxide film 1-4 nm thick which isolates the metal surface from a corrosive aqueous environment. A lot of work has been done regarding the chemical composition and structure of passive films formed on as cast ferrous alloys [17–23]. But the study on the electrochemical and transport properties of these films are not done extensively. An increase in transpassive dissolution tendency with increasing chromium content in a Fe-Cr alloy was reported by Betova et al [24]. Nonetheless, the reason behind the complex nature of the passive film formed at the interfaces of metal and

the electrolyte is yet to be fully understood. This complexity has made it difficult to predict the kinetic and transport parameters of the passive layer.

Fe-Cr alloys have been primarily made by casting followed by thermomechanical processing and heat treatment [25, 26], but only limited work has been reported on the powder metallurgy source Fe-Cr alloys. In the work by Heintze *et al.* [27], high energy ball milling was conducted followed by SPS and HIP. However, the ball milled powders for different milling durations were not fully analyzed and results were not interpreted. Also, corrosion study has not been done on spark plasma sintered simple Fe-Cr alloy system. Although analyses of corrosion and microstructural behavior have been done on complex Fe-Cr-X alloy systems previously [28-30], a comparative study of the corrosion behavior between a SPSed Fe-Cr based alloys has not been done yet. Hence, the present work was undertaken to obtain an understanding of the microstructural evolution and corrosion characteristics of the Fe-xCr alloys processed via high energy ball milling and SPS, as a function of composition.

4.2. Material and Methods

4.2.1. Processing methods and metallographic characterization

Iron powder (99.9+% metal basis) of around 10 µm size and chromium powder (99.95% metal basis) of 50 µm size were weighed in order to make a nominal composition of Fe-xCr powder batches with 6, 9, 10 and 12 wt% Cr, which were poured into stainless steel vials along with stainless steel balls (milling medium) of 8 mm diameter under an argon atmosphere inside a glove box to prevent oxidation/contamination. No surfactant was added to the milling mixture. The ball to powder weight ratio was around 10:1 [31]. The filled vials

were loaded in a shaker mill (SPEX 8000M) and milled for 10 h. The carbon and nitrogen content of the powders were estimated to be approximately 0.020 wt% and 0.024 wt%, respectively, using combustion analysis.

The milled powders were characterized in a Zeiss Supra 35 VP Field-Emission Gun Scanning Electron Microscope (FEG-SEM) to examine the powder size and morphology. X-ray diffraction (XRD) of ball milled powders were performed using Siemens 5000D diffractometer with Cu $K\alpha$ X-ray radiation (wavelength of 0.1541 nm). Using the XRD data, lattice parameters of the milled powders were calculated based on the Nelson–Riley relation [32]. The crystallite size and lattice strain were evaluated using the Williamson–Hall equation [33]:

$$\beta_{hkl} = 0.94\,(\lambda/L\cos\theta_{hkl}) + 4\varepsilon\tan\theta_{hkl} \qquad (4.1)$$

where β_{hkl} is the full width half maxima (FWHM) of the XRD peak, L is the crystallite size and ϵ is the lattice strain.

All the 10 h ball milled powder batches were consolidated via SPS at an applied pressure of 80 MPa for 45 min at 1000 ^{O}C. The heating rate used was 100 ^{O}C/min and the cooling rate was 40 ^{O}C/min. Density of the sintered samples was measured by Archimedes principle. The weight of the samples was taken in air and fully immersed condition in deionised water using an Ohaus Precision Balance (HRB-200). The density of deionised water (1 g/cm^3) and the density of air (0.0012 g/cm^3) at standard room temperature and pressure were used for density calculation. The theoretical density of the sample was calculated based on the composition using the following equation:

$$\rho^{Th}_{sample} = 100/(C_{Fe}/\rho_{Fe} + C_{Cr}/\rho_{Cr}) \qquad (4.2)$$

where, ρ^{Th}_{sample} is the theoretical density of the sample, ρ_{Fe} is the density of iron (7.87 gm/cc), ρ_{Cr} is the density of chromium (7.19 gm/cc), C_{Fe} is the wt fraction of Fe in the sample and C_{Cr} is the weight fraction of Cr in the sample. The relative density was then estimated in terms of the percentage of theoretical density.

Vickers microhardness tests were performed on the SPSed samples using a LECO 100M Microhardness Tester using a load of 0.5 kgf load and a loading time of 15 s. The same X-ray diffractometer and the SEM was used to analyze the phase constituents and grain size of the SPSed samples.

4.2.2. Corrosion characterization

Electrochemical corrosion testing on the SPSed samples was carried out using a potentiostat (Versa STAT MC, Ametek). Highly pure deionized water having a resistivity of 18.2 MΩ-cm was used for preparing electrolyte solutions for all the corrosion tests. A three-electrode system was used for the test. The working electrode was polished to 0.5 µm finish. (Fe-Cr samples with a surface area of 1 cm^2), the reference electrode was Ag/AgCl (199 mV vs Standard Hydrogen Electrode) and the counter-electrode was a platinum wire having a surface area of 2 cm^2. The corrosion test was performed in three different aqueous solutions such as 0.5M H_2SO_4, 0.05M NaH_2PO_4 and 1M NaOH. One ingot-metallurgy (wrought) HT9 alloy (Fe-12Cr-1Mo-0.5W-0.5Ni-0.25V-0.2C), a high strength ferritic-martensitic stainless steel was also investigated for comparison.

Corrosion potential was recorded for about 30 min. After reaching a steady state open circuit potential (OCP), linear polarization (LP) was carried out by scanning the potential within a potential window of ± 25 mV with respect to OCP with a scan rate of 1 mV/s. After LP, potentiodynamic polarization (PD) was performed by scanning the potential in the range of -0.5 V to +1.5V with respect to OCP at a rate of 1 mV/s. In order to understand the passivation behavior of the specimens, potentiostatic tests were carried out. Freshly polished samples were passivated for 1 h by applying a constant potential corresponding to the middle potential of the passive range from the anodic polarization plot. The electrochemical impedance spectroscopy (EIS) was carried out at the passivation potential by scanning the frequency in the range of 0.01Hz to 10,000 Hz. Mott-Schottky analyses was carried out at 1 kHz by scanning the potentials in the cathodic direction at 50 mV intervals from the passivation potential to OCP. All the corrosion tests have been duplicated and sometimes triplicated to verify reproducibility. The tabulated values are the average values of the test runs and the plots depict the best condition.

4.3. Results and Discussion

4.3.1 Microstructural Characterization of the Milled Fe-Cr Powders

The milled powder batches were examined by SEM. Figures 4.1(a)-(d) show the secondary electron (SE) SEM images of the powder samples ball milled for 10 h having different Cr content (6, 9, 12, and 14 wt%), respectively.
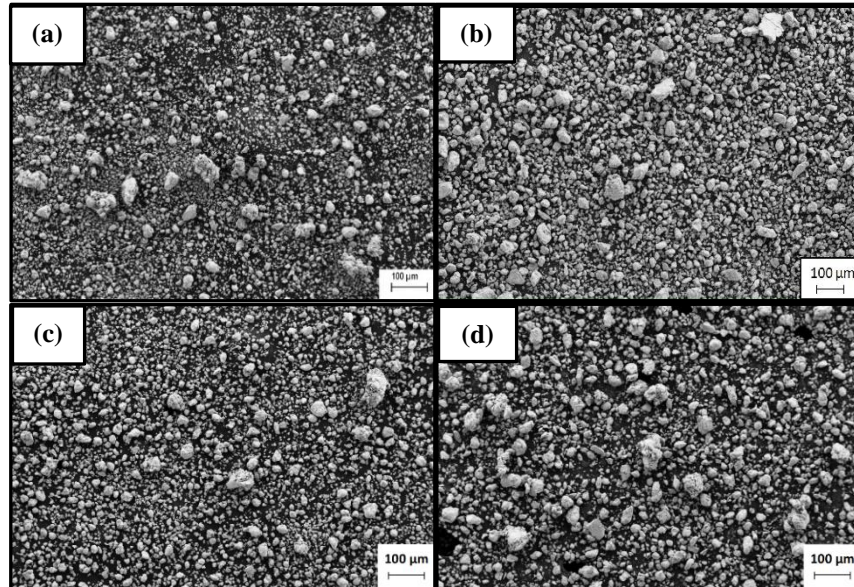
Figure 4.1. Secondary electron SEM images of (a) Fe-6Cr, (b) Fe-9Cr, (c) Fe-12Cr and (d) Fe-14Cr powders ball milled for 10 hr

Powder size analysis revealed that the mean powder size increased as a function of increasing chromium content as shown in Figure 4.2. Also, the powder size distribution became progressively wider with increasing Cr content. It can be inferred that with increasing Cr during milling, the Fe-Cr alloy becomes more solid solution hardened [34] and consequently both the powder size and powder size distribution increases.
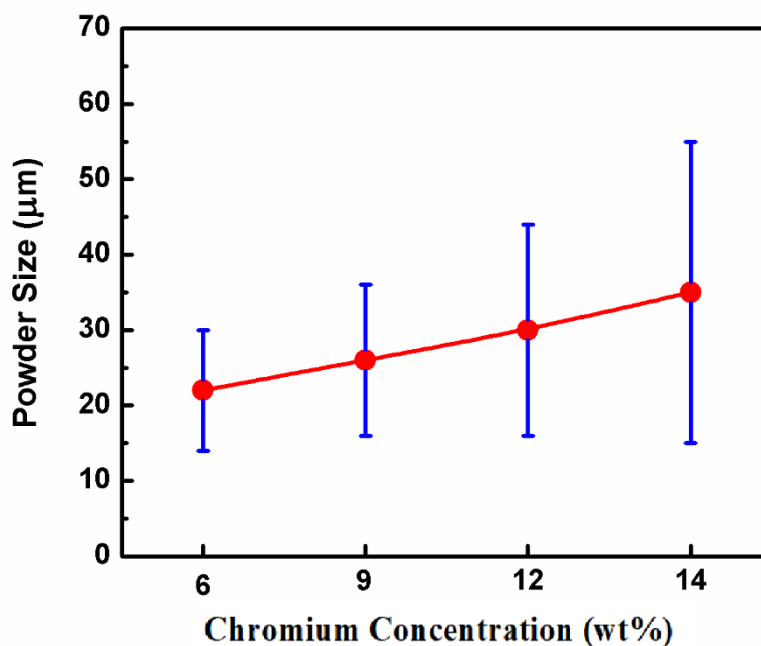
Figure 4.2. Powder Size distribution of Fe-Cr powders ball milled for 10 hr

Figure 4.3 shows XRD patterns of the various milled powder samples. Prominent peaks are observed near the diffraction angles (2θ) of 44.91°, 65.46° and 82.57°. These peaks correspond to the planes {110}, {200} and {211} of BCC Fe, respectively [35]. The lattice parameter of α-Fe is 2.87 Å and that of Cr is 2.89 Å. A slight shift of the peaks to the left is observed with increasing Cr, which signifies progressive dissolution of Cr into the Fe matrix. Also, from Table 4.1 it can be noted that with increasing the chromium concentration, the lattice parameter of the Fe-Cr powders increases which is another indication that Cr is getting incorporated into the matrix. Although the lattice parameter decreases, the strain does not vary significantly with change in the Cr content.
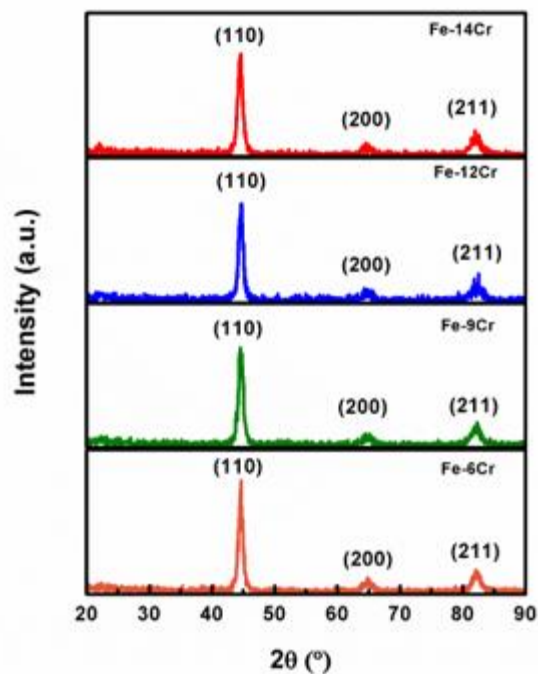
Figure 4.3. X-ray diffraction patterns of milled Fe-Cr powder batches.

Table 4.1. Lattice parameter, crystallite size and lattice strain of the Fe-Cr powder batches as analyzed from the XRD data

Sample description	Lattice parameter (Å)	Crystallite size (nm)	Strain (%)
Fe-6Cr	2.871 ± 0.001	11.59 ± 0.02	0.607
Fe-9Cr	2.873 ± 0.001	11.13 ± 0.02	0.616
Fe-12Cr	2.879 ± 0.001	10.81 ± 0.02	0.621
Fe-14Cr	2.882 ± 0.001	10.78 ± 0.02	0.626

4.3.2. Characteristics of Spark Plasma Sintered Fe-Cr Samples

4.3.2.1. Evaluation of density and microhardness

In this section, density and Vickers microhardness results of SPSed Fe-xCr alloys are presented and discussed. Figure 4.4 shows the variation of relative density of the sintered samples with increasing Cr content. With an increase in Cr concentration, the relative density keeps on decreasing. The reason behind this trend is that with the milled powder size increased with increasing Cr content. Bigger powder size results in lower compaction and thus during the consolidation process via spark plasma sintering the porosity level increased resulting in lower density for the higher chromium counterparts.
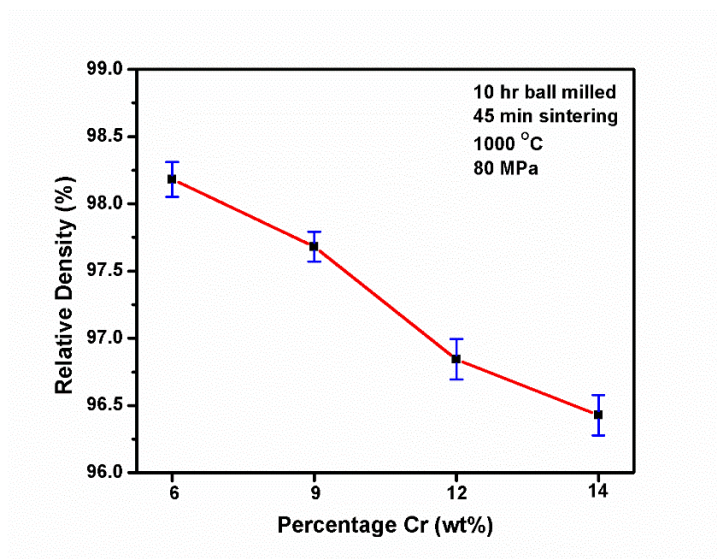
Figure 4.4. The variation of relative density with increasing Cr content

Figure 4.5 shows the variation of microhardness with increase in Cr content. It is known that with increasing chromium percentage the alloy becomes more solid solution strengthened. According to solid solution strengthening equation [34]:

$$\sigma_{SS} = \sum A_i C_i \qquad (4.3)$$

where A_i is the strengthening coefficient of alloying elements Cr (8.5 MPa/wt%) [36] and C_i is the concentration of the alloying elements in wt%. So, with increase in Cr the microhardness of the material should increase.
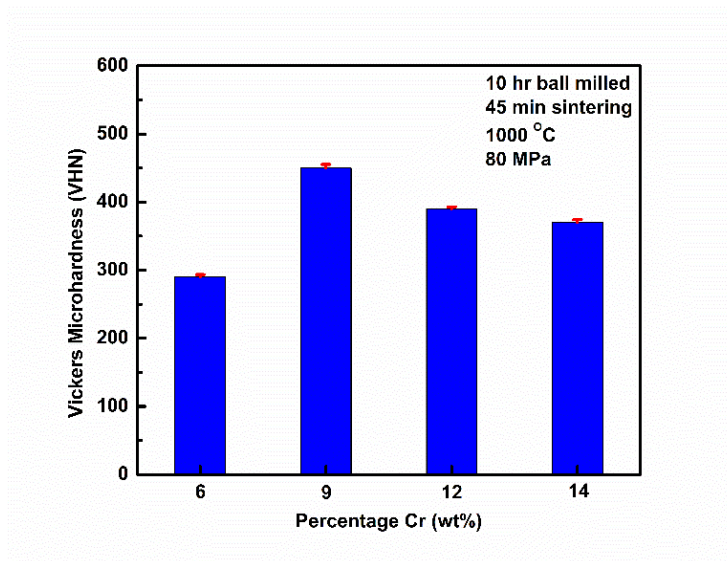
Figure 4.5. The variation of microhardness of Fe-Cr alloys with increasing Cr content

The microhardness is found to increase significantly from 6 wt% to 9 wt% Cr samples. But the hardness decreased as we increased the chromium content from 9 to 14 wt%. One of the reasons behind this is that due to the decrease in relative density, the porosity in the material increases which plays a significant role in decreasing the microhardness value of the subsequent materials. That effect of increase in porosity could not be counteracted by the solid solution strengthening along with other modes of strengthening mechanisms imparted by slightly smaller crystallize sizes.

4.3.2.2. Evaluation of XRD pattern

Figure 4.6 shows the XRD pattern of the sintered specimens. The peaks clearly show the presence of ferrite (BCC). Since iron and chromium peaks are almost similar, they cannot be distinguished.
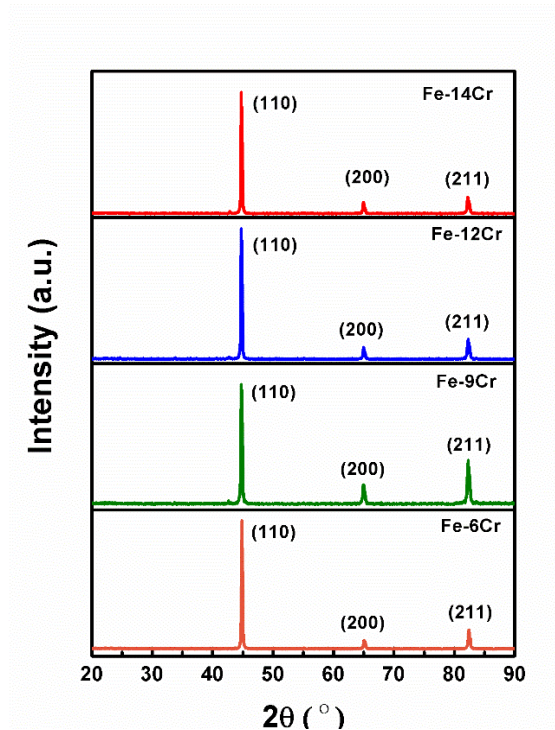
Figure 4.6. X-ray diffraction patterns of SPSed Fe-Cr samples

4.3.2.3. Sintering kinetics

In order to understand the SPS kinetics, the model proposed by Young and Cutler [37] has been used. In their study, non-isothermal equations for volume and grain boundary diffusion have been modified. The equations represent the relationship between the shrinkage (Y) and diffusion coefficient (D), where c represents the heating rate in units of $K.s^{-1}$ [37]:

$$ln(YT\frac{dY}{dT}) = ln(\frac{2.63\gamma\Omega D^0{}_v}{ka^3c}) - \frac{Q_v}{RT} \qquad (4.4)$$

$$ln(Y^2T\frac{dY}{dT}) = ln(\frac{0.71\gamma b\Omega D^0{}_b}{ka^4c}) - \frac{Q_b}{RT} \qquad (4.5)$$

where Y is the linear shrinkage ($\Delta l/l_o$), Ω is the volume of vacancy (m³), γ is the surface energy (J/m²), D_V is the volume diffusion coefficient given by $D_V = D_0{}^V \exp(-Q_V /RT)$ (m².s⁻¹), bD_B is the product of the grain boundary thickness 'b' and grain boundary diffusion coefficient 'D_B' given by $D_B = D_0{}^B \exp(-Q_B /RT)$ (m³.s⁻¹), k is the *Boltzmann* constant (J/K), T is the temperature (K), a is the particle radius (m) and t is time (s). Q_V and Q_B are the activation energy for volume diffusion and grain boundary diffusion, respectively. The activation energies for volume diffusion and grain boundary diffusion can be obtained from the slope of the plots between ln $(YT(dY/dT))$ versus $1/T$ and ln $(Y^2T(dY/dT))$ versus $1/T$, respectively.
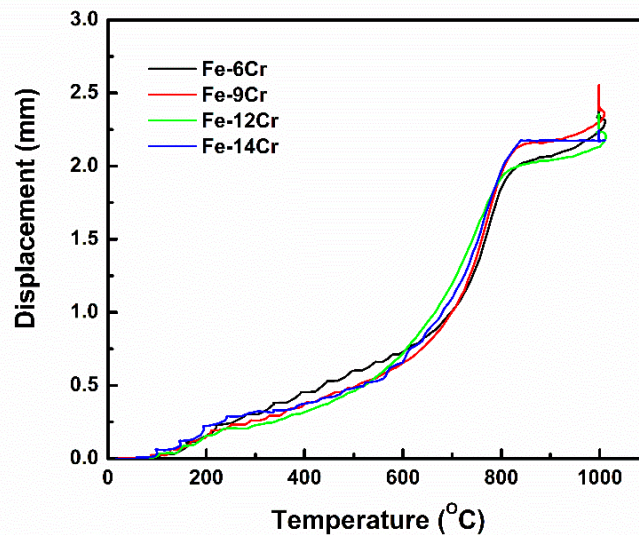
Figure 4.7. Displacement profile curve of the Fe-Cr alloy samples sintered at 1000 °C for 45 min under a pressure of 80 MPa.

Figure 4.7 depicts the displacement profile curves of the SPSed samples. Constant heating rate was used during SPS. The temperature at which densification begins (Ts) and the temperature at which maximum densification rate occurs (T_{max}) is calculated from the displacement curve and its first derivative respectively [38] and are listed in Table 4.2. It is found that densification starts at around 600 ^{O}C and reaches the maximum rate at 825 ^{O}C which is similar to the values obtained by previous studies [39]. From the slope of the ln (YT dY/dT) versus 1/T plots shown in Figure 4.8(a), the volume diffusion activation energy for the 10 h milled Fe-xCr sintered at 1000 ^{O}C was estimated. From the slope of the ln (Y^2T dY/dT) versus 1/T plots shown in Figure 4.8(b), the grain boundary diffusion activation energy for the 10 h milled Fe-xCr sintered at 1000 ^{O}C alloy was estimated. The calculated data is tabulated in Table 2.2. The activation energy for volume diffusion and grain boundary diffusion of pure α–Fe is 251 and 174 kJ/mol, respectively [40]. The nanograin boundary diffusion for Fe powder was estimated to be 187 kJ/mol according to Lee et al. [41].
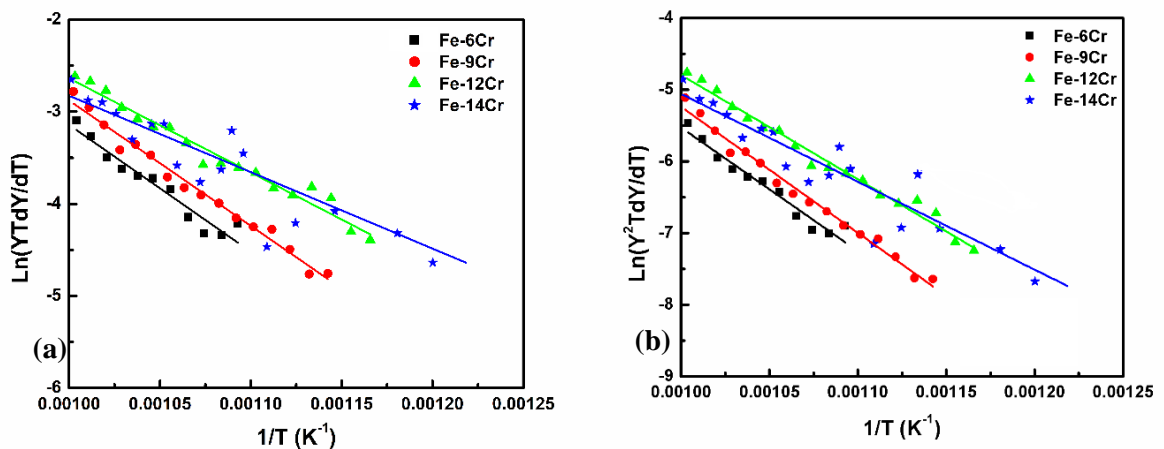
Figure 4.8. Activation energy profiles for (a) volume diffusion and (b) grain boundary diffusion of the Fe-Cr alloy sample sintered at 1000 ^{O}C for 45 min under a pressure of 80 MPa.

Table 4.2. Kinetic parameters of Fe-Cr alloy as calculated from the displacement data during SPS process

Sample description	Sintering Start Temperature (^{O}C)	Sintering Finish Temperature (^{O}C)	Activation Energy for Volume diffusion ($Kjmol^{-1}K^{-1}$)	Activation Energy for Grain Boundary diffusion ($Kjmol^{-1}K^{-1}$)
Fe-6Cr	640	820	115	146
Fe-9Cr	600	825	130	170
Fe-12Cr	585	833	86	121
Fe-14Cr	550	841	69	102

Considering the above scenario, one can hypothesize that in the initial phase of sintering the grain boundary diffusion is found to be the dominant mechanism. The plausible reason for this could be preponderance of boundaries due to the nanocrystalline crystallite size produced during high energy ball milling. However, during the process of SPS, various mechanisms can occur as reported in previous studies [15]. One of the reasons that in the initial phase, surface diffusion is the dominant mechanism because electric charge is concentrated mainly on the outer surface of the particles leading to capacitive nature between two nearby powder particles producing enough heat for the surface diffusion to take place. In the later stage when enough particles have joined with each other, the volume diffusion or the lattice diffusion might come into play as depicted in Figure 4.8, but the exact mechanism of the final stage of densification is yet unknown. With increasing chromium percentage, it is seen that GB diffusion activation energy is increasing from 6 to 9 wt% Cr and then decreasing. Thus, the higher chromium alloy starts diffusion at lower temperature compared to their lower chromium counterparts. Also, the temperature range for the GB diffusion increases with increasing chromium percentages.

4.3.2.4. Corrosion Analysis

Open circuit potential (OCP or simply corrosion potential) represents a mixed potential at which the anodic reaction rate is equal to the cathodic reaction rate. More negative OCP of a specimen indicates higher activity for corrosion in a given environment. OCP profiles (OCP versus time) of the Fe-xCr alloys and Alloy HT-9 in 0.5M H_2SO_4, 0.05M NaH_2PO_4 solution and 1M NaOH solution are shown in Figure 4.9(a)-(c), respectively. The OCP increased with increase in the Cr content in the 0.5 M H2SO4 solution as seen Figure 4.9(a). It is observed that a steady state of OCP was reached quickly for HT-9. A steady state of OCP was observed for Fe-9Cr after about 600 s. Fe-6Cr showed a decreasing trend whereas Fe-12Cr and Fe14Cr specimens exhibited increasing trend of OCP with time. Since OCP is influenced by exchange current densities and Tafel slopes of both anodic and cathodic reactions, the variations in the OCP could be attributed to change of these parameters individually and in combination. The exchange current density and Tafel slope of cathodic reaction are catalyzed by surface. Therefore, these parameters will be influenced by the composition of the specimens. There are two possible cathodic reactions in the sulfuric acid solution which is not de-aerated, namely:

$$2H^+ + 2e^- \rightarrow H_2$$

$$4H^+ + O_2 + 4e^- \rightarrow 2H_2O$$
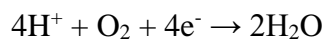
The anodic reaction is given by $M \rightarrow M^{n+} + ne^-$. If the kinetics of the cathodic reactions were the same for all the specimens in this study (which may not be true), the decrease in the OCP values with time and lower OCP of Fe-6Cr could be attributed to absence

of a passive layer in the 0.5M H_2SO_4 solution that increased the exchange current density and decreased Tafel slope for anodic reaction. Increase in Cr content in the alloy increased the anodic Tafel slope and decreased the exchange current density. The increase in the OCP with time for Fe-12Cr and Fe-14Cr could be attributed to the formation and thickening of a passive film that subsequently increased the anodic Tafel slope.

In case of 0.05M NaH_2PO_4 solution (Figure 4.9(b)), due to the formation of complex oxide layer possibly containing PO_4^{3-} ions, the nature of OCP starts varying. Porosity in the materials starts playing an important role here. Since HT 9 is a wrought material, the porosity level in the material is very low and forms a relatively defect free surface layer. Therefore, it has a higher OCP value compared to other alloys. The SPSed materials show an increase in OCP values with increase in Cr content. However, since Fe-14Cr has a higher porosity level than Fe-12Cr, the former has a lower OCP value. In the 1M NaOH solution (Figure 4.9(c)), the formation of hydroxide layer is more probable [42]. In this solution, Fe-6Cr and Fe-9Cr exhibit a surprising characteristic compared to the other alloys. This may be related to the formation of a thicker iron oxyhydroxide layer. Fe-12Cr and HT9 alloy have the same amount of chromium but the latter one having lower porosity has a higher OCP. Although Fe-14Cr has higher Cr content than Fe-12Cr, the porosity level in Fe-14Cr is higher than in Fe-12Cr resulting in lower OCP than the latter. Linear polarization resistance (Rp) is the resistance of the specimen to charge transfer across the electrochemical interface during the application of an external potential [43]. The lower the value of the Rp, higher is the corrosion rate of the material. Table 4.3 shows the Rp values of the alloys in various solutions. The Rp values show a general trend of increase with increasing Cr content of Fe-Cr alloy samples in a particular

solution. The pH of the solution influenced the *Rp* values significantly. The specimens showed

higher *Rp* values in high pH solution. The corrosion resistance was low when the pH was low.
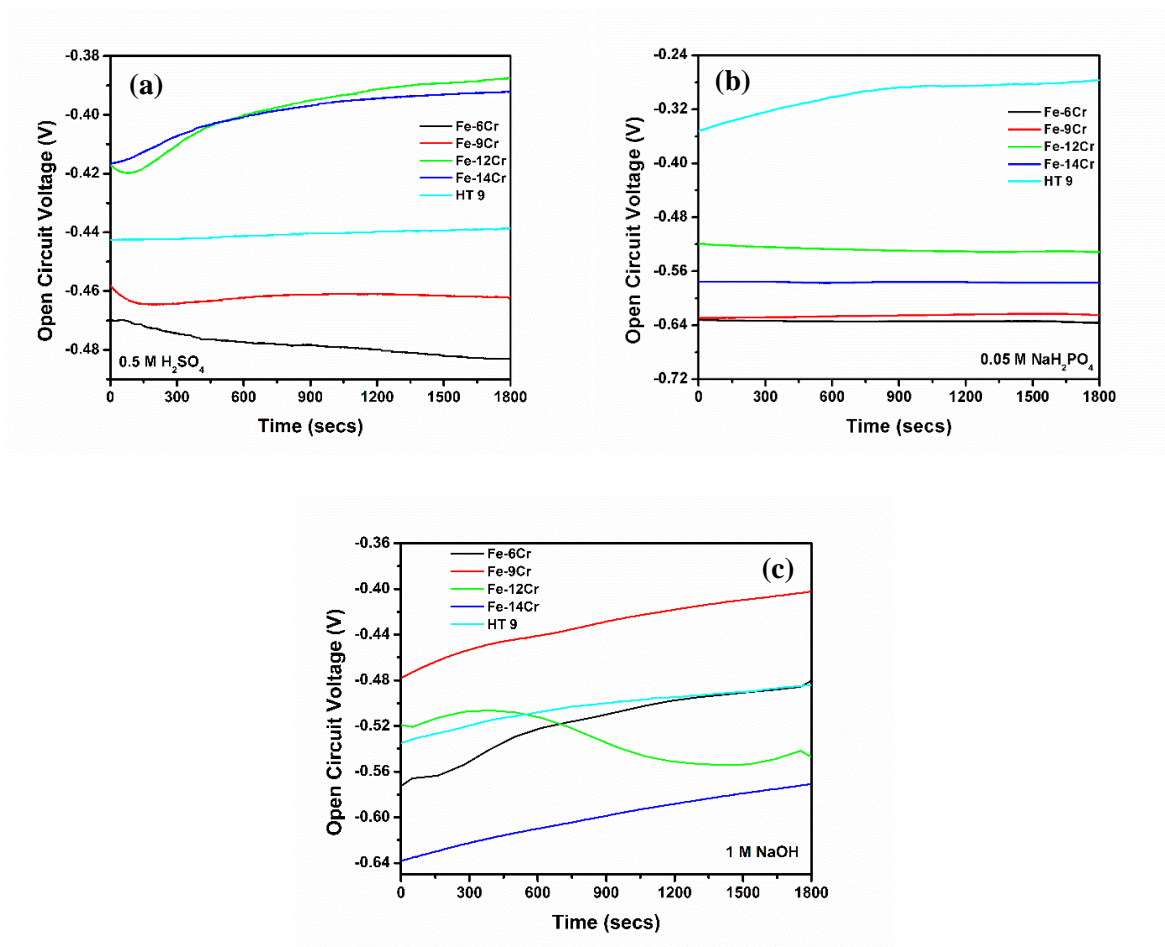
Figure 4.9. OCP in (a) 0.5M H_2SO_4, (b) 0.05M NaH_2PO_4 solution and (c) 1M NaOH solution

Table 4.3. Resistance values of different alloys in the three different solutions.

Solution	Material	Linear Polarization Resistance (Rp) $(\Omega.cm^2)$
0.5 M H$_2$SO$_4$	Fe-6Cr	12.73
	Fe-9Cr	16.78
	Fe-12Cr	20.02
	Fe-14Cr	20.37
	HT 9	20.07
0.05M NaH$_2$PO$_4$	Fe-6Cr	272.63
	Fe-9Cr	1272.34
	Fe-12Cr	1536.05
	Fe-14Cr	1450.99
	HT 9	62877.7
1 M NaOH	Fe-6Cr	39507.78
	Fe-9Cr	53883.63
	Fe-12Cr	56059.98
	Fe-14Cr	127953.11
	HT 9	82388.78

Figures 4.10 (a) – (c) illustrate the potentiodynamic polarization behavior of the specimens in 0.5M H$_2$SO$_4$, 0.05M NaH$_2$PO$_4$, and 1M NaOH solutions, respectively. All the specimens showed more or less similar cathodic polarization behavior in the 0.5M H$_2$SO$_4$ solution. Whereas, the anodic polarization behavior was widely different between different specimens which was a strong function of porosity level. The HT-9 showed good passivation behavior with a passive current density lower than 10 µA/cm^2 between -0.2 to 1.2 V$_{Ag/AgCl}$. The Fe-Cr SPSed specimens do not show passivation in 0.5M H$_2$SO$_4$ solution. With increasing Cr, a passivation layer is formed on Fe-12Cr and Fe-14Cr as seen from the OCP results but absence of a passive region during anodic polarization could be attributed to not attaining the critical current density for achieving passivity. For example, HT9 showed a critical current

density of about 32 mA/cm^2 to attain passivity. This current density was recorded at a potential of -0.4 V$_{Ag/AgCl}$. On the other hand, SPSed Fe-12Cr and Fe-14Cr showed passivity only above 0.8 V when the current density was about 100 mA/cm^2. The Fe-6Cr and Fe-9Cr specimens did not show passivity plausibly because the critical current density for passivation could not be achieved in the potential range during anodic potential scan at a rate of 1 mV/s. In 0.05M NaH$_2$PO$_4$ solution, due to the buffering nature of the solution, the alloys behave differently. Distinct passive regions are revealed in the anodic polarization plots of specimens except for Fe-9Cr as seen in Figure 4.10(b). HT9 showed the lowest passive current density. All the specimens showed a critical current density to attain the passivation which increased as the Cr-content of the alloy decreased. The critical current density was recorded at around 0 V$_{Ag/AgCl}$ in most of the specimens, and this value increased with decrease in the Cr level. The critical current density was orders of magnitude larger than the passive current density in case of Fe-6Cr or Fe-14Cr, whereas HT9 and Fe-12Cr showed almost similar order of critical current density and passive current density. The Fe-9Cr specimen did not reveal passivation until 1.5 V$_{Ag/AgCl}$ beyond which the current started decreasing. Therefore, it could be argued that the Fe-9Cr specimen required very large critical current density to attain passivity. The higher critical current density requirement could be attributed to the relatively faster scan rate of the potential (1 mV/s). In 1M NaOH solution, all the alloys showed similar passivation behaviors. It has been reported in previous studies [44] that formation of Cr(III) oxide and its slow dissolution rate in alkaline solution are responsible for the excellent passive behavior of high-Cr Fe based alloys.
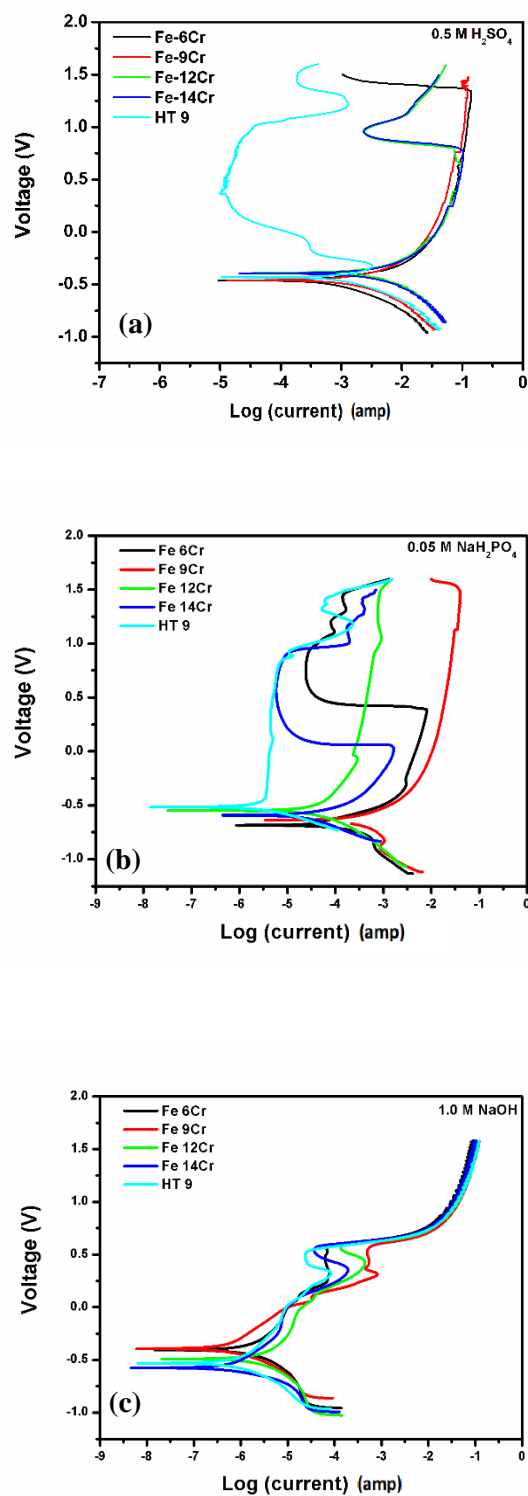
Figure 4.10. Potentiodynamic study in (a) 0.5M H_2SO_4, (b) 0.05M NaH_2PO_4 solution and (c) 1M NaOH solution

Potentiostatic passivation was carried out on the Fe-xCr alloys and Alloy HT-9 in 0.5M H_2SO_4, 0.05M NaH_2PO_4 solution and1M NaOH solution for 1 h and the results are shown in Figures 4.11(a)-(c), respectively. Figure 4.11(a) shows the passive current transients recorded in the 0.5M H_2SO_4 solution at a potential which is the middle potential of the passivation zone as obtained from Figure 4.10(a). It is interesting to note that during potentiodynamic polarization, a large current (in the order of 100 mA/cm^2) is recorded on the Fe-Cr alloys which precluded a passivation behavior. On the other hand, under potentiostatic conditions a current decay behavior is observed which implied formation of a surface layer that resulted in passivation. Fe-6Cr and Fe-9Cr showed a delayed passivation. During the first 200-300 s of potentiostatic conditioning, the current decay is slow with an exponent of 0.07. After about 500 s, an abrupt current decay is observed. This behavior could be attributed to passivation by dissolution and reprecipitation mechanism. It can be argued that during the initial 500 s dissolution occurred because of the high current density which increased the ionic strength at the electrode/electrolyte interface. When the ionic strength reaches super saturation because of slow convection or local change in the pH, precipitation of a surface layer occurs which causes abrupt current decay. The Fe-12Cr and Fe-14Cr specimens showed an instantaneous current decay behavior with the application of a constant potential with a decay exponent of about 0.68.
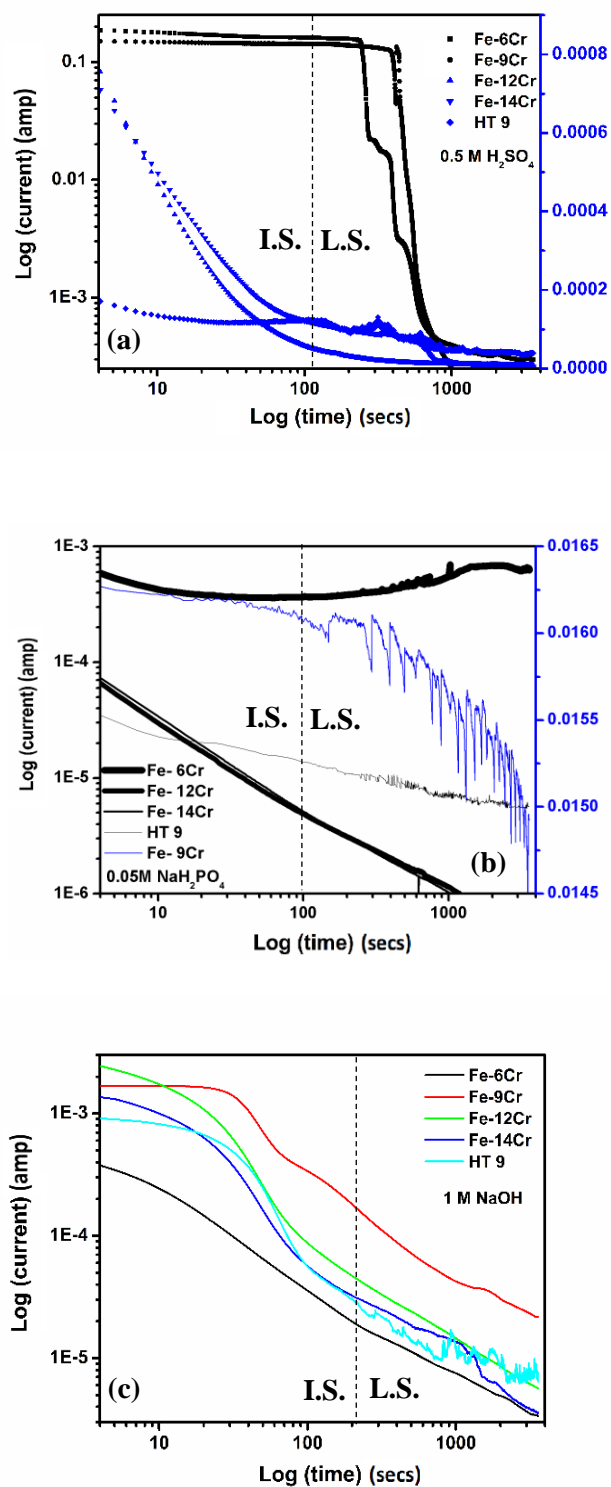
Figure 4.11. Passivation study in (a) 0.5M H_2SO_4, (b) 0.05M NaH_2PO_4 solution and (c) 1M NaOH solution. (I.S: Initial stage; L.S: Later Stage.)

Figure 4.11(b) shows the current decay behaviors of the Fe-Cr alloys in the 0.05M NaH$_2$PO$_4$ solution. A similar behavior is seen for the Fe-6Cr and Fe-9Cr alloy specimens like in the 0.5M H$_2$SO$_4$ solution. Both of these alloys exhibit a delayed passivation, although Fe-6Cr initially showed a corrosion tendency. Figure 4.11(c) shows the current decay behaviors of Fe-Cr alloys in the 1 M NaOH solution. The passivation in alkaline solution is observed occur with three different slopes for all the specimens except for Fe-6Cr. In the absence of surface chemical analysis data, it is difficult to delineate the possible surface reactions for each slope. The overall reactions could be formation of a Cr-rich oxide, Fe-Cr containing spinel oxide, and conversion of the Fe-Cr based oxide into its oxyhydroxide.

The passive current decay can be represented using the following equation [45]:

$$I = I_0 t^{-\alpha} \qquad (4.6)$$

where, I is the passivation current at time t, I_0 is initial current density of the fresh specimen surface in the test environment and α is the passivation kinetic exponent. The value of α gives us an idea about how quickly the surface gets passivated in an environment. Higher the value of α, faster is the passivation kinetics. Negative value indicates passivity layer breakage. The values of the α for the different alloys in different solutions are summarized in Table 4.4.

Table 4.4. Passivation kinetic exponent values of different alloys in the three different solutions.

Solution	Material	Passivation kinetic exponent (α)	
		Initial stage	Later stage
0.5M H_2SO_4	Fe-6Cr	0.0697	0.2778
	Fe-9Cr	0.0003	0.5832
	Fe-12Cr	0.6834	0.1867
	Fe-14Cr	0.6881	0.2352
	HT 9	0.2434	0.6481
0.05M NaH_2PO_4	Fe-6Cr	0.0072	-0.0031
	Fe-9Cr	0.0033	0.0285
	Fe-12Cr	0.0136	0.0142
	Fe-14Cr	0.0159	0.0163
	HT 9	0.0082	0.0062
1 M NaOH	Fe-6Cr	0.6921	0.7385
	Fe-9Cr	0.4832	0.7432
	Fe-12Cr	0.5881	0.8781
	Fe-14Cr	0.4362	0.9291
	HT 9	0.4041	0.8047

From Table 4.4 we can deduce that the passivation kinetics of the alloys is slower in the low pH solution than in the alkaline pH. Passivation kinetics increases with increasing Cr content in all the solutions. Also, the passivation depends on the porosity level. Fe-12Cr showed faster passivation kinetics than HT9 in spite of having almost similar Cr content. This could be attributed to the finer grain size of the SPSed Fe-12Cr. Therefore, the passivation reaction could be associated with possible grain boundary diffusion of Cr.

EIS was carried out followed by the potentiostatic passivation and the results are given in Figures. 4.12(a)-(c) in the form of Bode plots. Nyquist plots and phase angle vs. frequency

plots are included in the supporting information as shown in Figures A.2(a)-(c) and Figures A.3(a)-(c) respectively. Figure 4.12(a) shows the impedance moduli of Fe-Cr alloys and HT9 in 0.5M H_2SO_4. The HT9 specimen showed the highest impedance and all Fe-Cr alloys other than Fe-6Cr showed almost similar impedance in the sulfuric acid solution. It is noted that the impedance results could not be directly related with the potentiostatic passive current decay behaviors. The impedance results of the specimens in the dihydrogen phosphate solution are shown in Figure 4.12(b). In this case, the Fe-9Cr shows the lowest impedance. This could be associated with the formation of defective surface layer during the potentiostatic conditioning that shows highly oscillating current decay behavior as seen in Figure 4.12(b). With the exception of Fe-9Cr, other Fe-Cr specimens show increasing impedance with increase in the Cr content in the neutral pH condition. Here also, the HT9 sample shows the highest impedance in this environment. Figure 4.12(c) shows the impedance characteristics of the specimens in the high pH solution. The impedance values are higher by an order of magnitude for all the specimens in the 1M NaOH solution than in low pH solutions. Among Fe-Cr specimens, the Fe-6Cr specimen shows the highest impedance. No direct correlation between Cr content of Fe-Cr alloy and the impedance magnitude is observed. The HT9 specimen shows very high impedance in all the pH conditions.
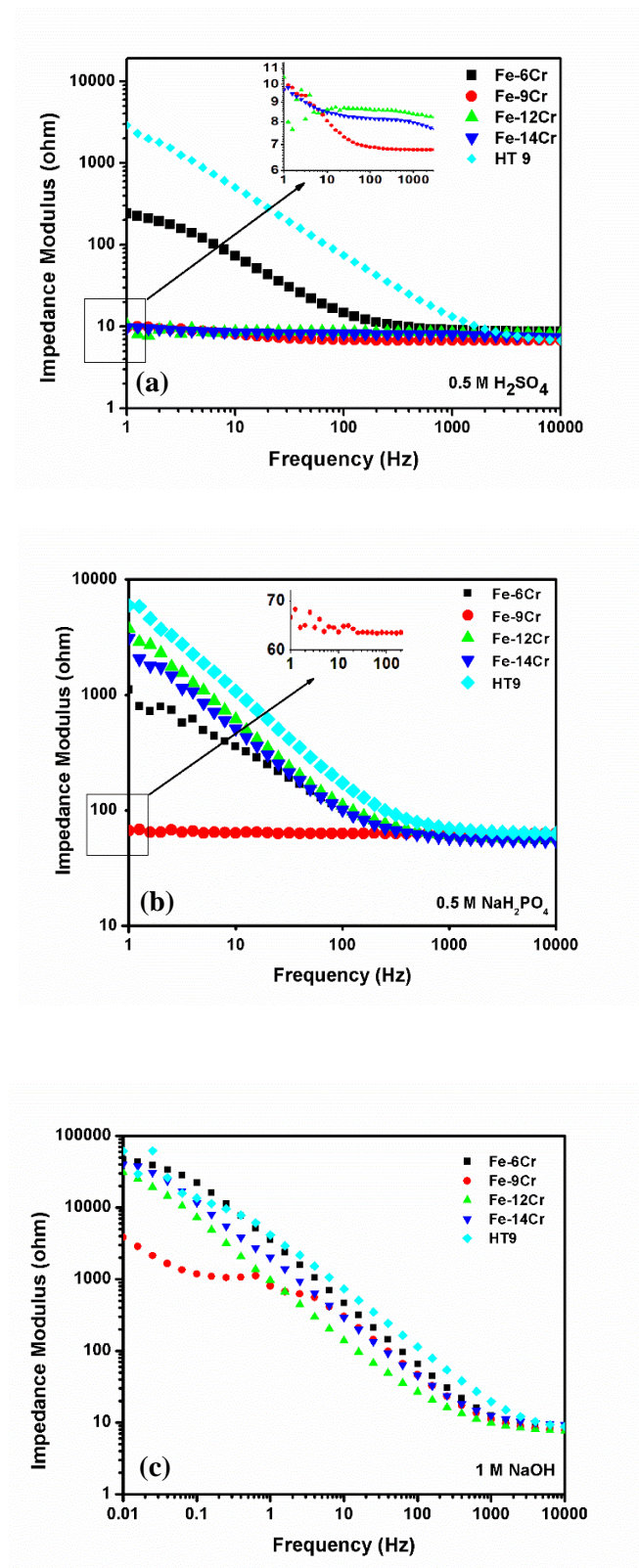
Figure 4.12. Bode plots in (a) 0.5M H$_2$SO$_4$, (b) 0.05M NaH$_2$PO$_4$ solution and (c) 1M NaOH solution

Figure 4.13 shows the Mott-Schottky plots of Fe-Cr alloys and HT-9 in different pH solutions. The potentiostatically formed passive layers on these specimens showed both n-type and p-type semiconductivity depending on the potential range. This phenomenon indicates that the Fe-Cr alloys contained a duplex layer with an inner *p*-type layer (Cr-rich oxide or $Fe_{1-x}O$) and an outer *n*-type layer (defective Fe_2O_3 type). The *n*-type semiconductivity could be attributed to possible presence of oxygen vacancies in the oxide layer, and the p-type could be assigned to metal cation vacancies [46,47]. The p-type behaviour observed at high anodic potentials (oxygen evolution potential range) could also be attributed to possible formation of an inversion layer with enhanced hole concentration at the surface level due to large upward band bending [48]. In addition, oxygen evolution occurring on the specimen surface could result in further oxidation of M^{3+} cations to higher valence states that leads to introduction of cation vacancies and p-type conductivity [49]. If p-type semiconductivity is observed at low anodic potentials, it could be associated with the formation of $Fe_{1-x}O$ or Cr_2O_3 type oxides that show inherent p-type semiconductivity [50].
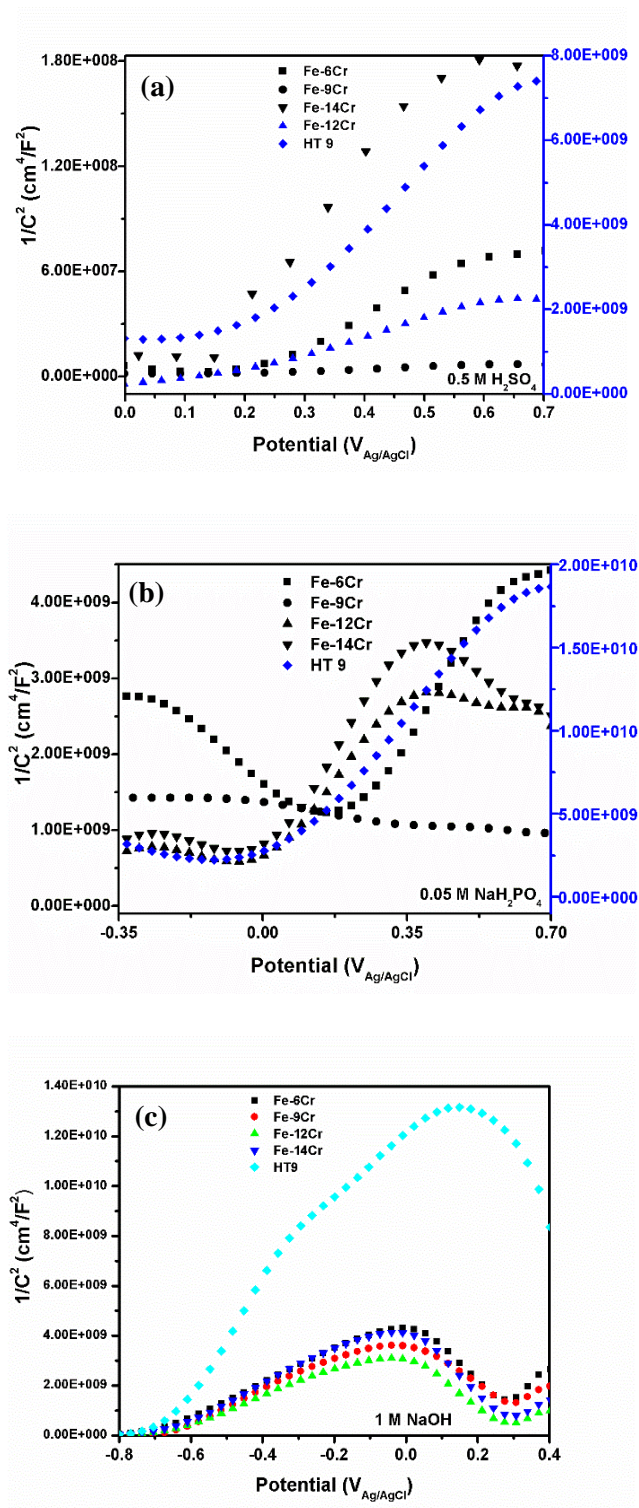
Figure 4.13. Mott-Schottky plot in (a) 0.5M H_2SO_4, (b) 0.05M NaH_2PO_4 solution and (c) 1M NaOH solution

Figure 4.13(a) shows the Mott-Schottky plots of Fe-Cr alloys in 0.5M H_2SO_4 solution. Predominantly an n-type surface layer is observed on these specimens in the sulfuric acid solution because of the positive slopes. Steeper is the slope of the $1/C^2$ Vs. potential, the lower is the charge carrier density (less defective is the surface layer). The slope of the Mott-Schottky plots increased with increase in the Cr-content, in general. Figure 4.13(b) shows the Mott-Schottky plots in the NaH_2PO_4 solution. Both n-type and p-type behaviours can be noted in this environment. Interestingly the Fe-6Cr showed predominantly the p-type characteristics in the investigated potential range. The reason for these characteristics is not known. One possible reason could be that the n-type layer of the duplex surface layer formed on this specimen became degenerate under the polarization and therefore exhibited only *p*-type semiconductivity.

Table 4.5 summarizes the charge carrier density of the passive films of different specimens in different pH solutions. Higher the charge carrier density, higher is the electrical conductivity and defect concentration which may lead to lower corrosion resistance. The SPSed specimens showed higher charge carrier density than the wrought HT9 specimen in all the pH conditions. This could be attributed to inherent porous nature of the bulk specimen and small grain sizes encountered in the SPSed specimens. Fine grain size promotes faster diffusion (short circuit diffusion through grain boundaries) of metal that ionized forming more cations. When the cation formation occurs fast under potentiostatic conditions, not enough oxygen anions are available at the interface to form stoichiometric oxide which leads to inherent oxygen vacancies. No direct correlation is observed between the Cr content of Fe-Cr alloys and the charge carrier density.

Table 4.5. Charge carrier density values of different alloys in the three different solutions.

Solution	Material	Region (V)	Charge Carrier Density (cm^{-3})
0.5 M H_2SO_4	Fe-6Cr	(-0.15 to 0.1)	-3.57 x 10^{21}
		(0.2 to 0.75)	1.17 x 10^{21}
	Fe-9Cr	(-0.15 to 0.1)	5.18 x 10^{22}
		(0.2 to 0.75)	5.03 x 10^{21}
	Fe-12Cr	(-0.15 to 0.1)	1.06 x 10^{21}
		(0.2 to 0.75)	1.67 x 10^{21}
	Fe-14Cr	(-0.15 to 0.1)	5.79 x 10^{21}
		(0.2 to 0.75)	2.38 x 10^{21}
	HT 9	(-0.15 to 0.1)	-7.95 x 10^{20}
		(0.2 to 0.75)	4.44 x 10^{20}
0.05 M NAH$_2$PO$_4$	Fe-6Cr	(-0.25 to 0.1)	-3.36 x 10^{20}
		(0.2 to 0.75)	1.82 x 10^{20}
	Fe-9Cr	(-0.1 to 0.5)	-3.00 x 10^{21}
	Fe-12Cr	(-0.25 to 0.1)	-2.29 x 10^{21}
		(0.1 to 0.4)	2.08 x 10^{20}
		(0.4 to 0.7)	-1.09 x 10^{21}
	Fe-14Cr	(-0.25 to 0.1)	-1.07 x 10^{21}
		(0.1 to 0.4)	1.37 x 10^{20}
		(0.4 to 0.7)	-3.52 x 10^{20}
	HT 9	(-0.8 to -0.1)	-5.46 x 10^{20}
		(0.0 to 0.7)	2.42 x 10^{20}
1 M NaOH	Fe-6Cr	(-0.8 to -0.1)	9.25 x 10^{20}
		(0 to 0.2)	-3.98 x 10^{20}
		(0.3-0.4)	4.34 x 10^{20}
	Fe-9Cr	(-0.8 to -0.1)	1.18 x 10^{21}
		(0 to 0.2)	-8.24 x 10^{20}
		(0.3-0.4)	8.98 x 10^{20}
	Fe-12Cr	(-0.8 to -0.1)	1.07 x 10^{21}
		(0 to 0.2)	-5.56 x 10^{20}
		(0.3-0.4)	1.05 x 10^{21}
	Fe-14Cr	(-0.8 to -0.1)	4.75 x 10^{20}
		(0 to 0.2)	-4.02 x 10^{20}
		(0.3-0.4)	4.52 x 10^{20}
	HT 9	(-0.8 to 0.2)	3.44 x 10^{20}
		(0.3 to 0.6)	-1.41 x 10^{20}

4.4. Conclusions

The main objective of this study was to understand the microstructural evolution and corrosion property of Fe-Cr alloy processed via ball milling and SPS. From the work the following salient features can be concluded.

1. The high energy ball milling of Fe-Cr samples resulted in nanocrystalline crystallite size in the milled powder.

2. With increasing chromium percentages, the powder size increased and powder size distribution became broader. The lattice parameter and lattice strain showed only slight variation with change in Cr content.

3. During SPS for 45 min at 1000 ^{O}C and 80 MPa pressure, it is seen that with increasing Cr content the relative density decreased which is attributed to the increase in powder particle size during ball milling.

4. Kinetics study indicates that in the initial stage of SPS, grain boundary diffusion is the dominant mechanism for the initial stage of consolidation process. Also, with increasing Cr content, it is seen that GB diffusion activation energy is decreasing and thus in the higher Cr alloy diffusion starts at lower temperature compared to their lower chromium counterparts. Also, the temperature range for the GB diffusion increases with increasing chromium percentages.

5. Corrosion analysis shows that with increasing pH of the solution, the passive layer formation occurs faster in the wrought HT-9 compared to the SPSed materials with even higher chromium contents.

6. Though at lower pH solution Fe-6Cr and Fe-9Cr alloys start passivating at longer time, at higher pH the passivation rate becomes almost similar for all the alloys

7. The passive layers formed under potentiostatic conditions on these specimens showed both n-type and p-type semiconductivity.

8. The SPSed specimens showed higher charge carrier density than the wrought HT-9 specimen in all the pH conditions.

Data availability

The raw/processed data required to reproduce these findings cannot be shared at this time as the data also forms part of an ongoing study.

Acknowledgement

References

1. A. Kohyama, A. Hishinuma, D.S. Gelles, R.L. Klueh, W. Diets and K. Ehrich, Auger spectroscopy study of the stress enhanced impurity segregation in a Cr-Mo-V steel, J. Nucl. Mater. 233 (1996) 138.

2. F.A. Garner, M.B. Toloczko and B.H. Sencer, Comparison of swelling and irradiation creep behavior of fcc-austenitic and bcc-ferritic/martensitic alloys at high neutron exposure, J. Nucl. Mater. 276 (2000) 123.

3. R.L. Klueh and D.H. Harries, High-Chromium Ferritic and Martensitic Steel for Nuclear Applications, ASTM, 2014.

4. K.S. Rajan, Selection of Materials for Reactor Internals, School of Chemical & Biotechnology, SASTRA University, 2014, www.nptel.ac.in/courses/103106101/Module%20-%204/Lecture%20-%202.pdf.

5. C. Suryanarayana, Mechanical alloying and milling, Progress Mater. Sci. 46 (2001) 1.

6. C.-L. Chen and Y.-M. Dong, Effect of mechanical alloying and consolidation process on microstructure and hardness of nanostructured Fe–Cr–Al ODS alloys, Mater. Sci. Eng. A 528 (2011) 8374.

7. C. Suryanarayana, E. Ivanov and V.V. Boldyrev, The science and technology of mechanical alloying, Mater. Sci. Eng. A 304 (2001) 151.

8. J.B. Fogagnolo, F. Velasco, M.H. Robert and J.M. Torralba, Effect of mechanical alloying on the morphology, microstructure and properties of aluminium matrix composite powders, Mater. Sci. Eng. A 342 (2003) 131.

9. M. Zawrah and L. Shaw, Microstructure and hardness of nanostructured Al/Fe/Cr/Ti alloys through mechanical alloying, Mater. Sci. Eng. A 355 (2003) 37.

10. R. Juarez, J.J. Sunol, R. Berlanga, J. Bonastre and L. Escoda, The effects of process control agents on mechanical alloying behavior of a Fe–Zr based alloy, J. Alloys Compd. 434 (2007) 472.

11. Z. Oksiuta and N. Baluc, Effect of mechanical alloying atmosphere on the microstructure and Charpy impact properties of an ODS ferritic steel, J. Nucl. Mater. 386 (2009) 426.

12. X.L. Wang, G.F. Wang and K.F. Zhang, Effect of mechanical alloying on microstructure and mechanical properties of hot-pressed Nb–16Si alloys, Mater. Sci. Eng. A 527 (2010) 3253.

13. O. Guillon, Field-Assisted Sintering Technology / Spark Plasma Sintering: Mechanisms, Materials, and Technology Developments, Adv. Eng. Mat. 16 (2014) 830

14. KU Leuven, SPS process modeling, https://www.mtm.kuleuven.be/Onderzoek/Ceramics/research/sintering/spark-plasma (accessed 09/27/2018).

15. M. Suárez, A. Fernández, J.L. Menéndez, R. Torrecillas, H. U. Kessel, J. Hennicke, R. Kirchner and T. Kessel, Challenges and Opportunities for Spark Plasma Sintering: A Key Technology for a New Generation of Materials in Sintering Applications, 2013, http://dx.doi.org/10.5772/53706 (accessed 09/27/2018).

16. C.F. Schonbein and M. Faraday, On a peculiar voltaic condition of iron, Phil. Mag. 53 (9) (1836) 122.

17. L.J. Oblonsky, A.J. Davenport, M.P. Ryan, H.S. Isaacs and R.C. Newman, In Situ X-Ray Absorption Near Edge Structure Study of the Potential Dependence of the

Formation of the Passive Film on Iron in Borate Buffer, J. Electrochem. Soc. 144 (1997) 2398.

18. M.F. Toney, A.J. Davenport, L.J. Oblonsky, M.P. Ryan and C.M. Vitus, Atomic structure of the passive oxide film formed on iron, Phys. Rev. Lett. 79 (1997) 4282.

19. L.J. Oblonsky, M.P. Ryan and H.S. Isaacs, In Situ Determination of the Composition of Surface Films Formed on Fe-Cr Alloys, J. Electrochem Soc. 145 (1998) 1922.

20. V. Schroeder and T. Devine, Surface enhanced Raman Spectroscopy Study of the Galvanostatic Reduction of the Passive Film of Iron, J. Electrochem. Soc. 146 (1999) 4061.

21. S. Virtanen, P. Schmuki, M. Buechler and H.S. Isaacs, Electrochemical Behavior of Fe in Phosphate Solutions Studied by In Situ X-Ray Absorption Near Edge Structure, J. Electrochem. Soc. 146 (1999) 4087.

22. L.J. Oblonsky, M.P. Ryan and H.S. Isaacs, In situ XANES study of the formation and reduction of the passive film formed on Fe in acetate solution, Corros. Sci. 42 (2000) 229.

23. P. Schmuki, S. Virtanen, A.J. Davenport and C.M. Vitus, Transpassive Dissolution of Cr and Sputter-Deposited Cr Oxides Studied by In Situ X-Ray Near-Edge Spectroscopy, J. Electrochem. Soc. 143 (1996) 3997.

24. I. Betova, M. Bojinov, A. Englund, G. Fabricius, T. Laitinen, K. Makela, T. Saario and G. Sundholm, Contact electric impedance and resistance studies of the conduction mechanism in passive films on ferrous alloys, Electrochimica Acta 46 (2001) 3627.

25. S. Li, Y. Wang, X. Dai, F. Liu, J. Li and X. Wang, Evaluation of hardening behaviors in ion-irradiated Fe-9Cr and Fe-20Cr Alloys by Nanoindentation Technique, J. Nucl. Mater. 478 (2016) 50.

26. K. Ono, K. Arakawa, H. Shibasaki, H. Kurata, I. Nakamichi and N. Yoshida, Release of Helium from Irradiation Damage in Fe-9Cr Ferritic Alloy, J. Nucl. Mater. 329 (2004) 933.

27. C. Heintze, M. Hernandez-Mayoral, A. Ulbricht, F. Bergner, A. Shariq, T. Weissgarber, and H. Frelinghaus, Nanoscale characterization of Fe-9%Cr model alloys compacted by spark plasma sintering, J. Nucl. Mater. 428 (2012) 139.

28. J. Liu and W. Chen, Microstructure, mechanical properties and corrosion behavior of an Fe-10Cr-2.7B-5.5Al-13Mn alloy prepared by spark plasma sintering, J. Alloys and Comp. 741 (2018) 348.

29. F.M. Kgoete, A.P.I. Popoola and O.S.I. Fayomi, Influence of spark plasma sintering on microstructure and corrosion behaviour of Ti-6Al-4V alloy reinforced with micron-sized Si_3N_4 powder, Defence Technology 14 (2018) 403.

30. G. Marnier, Clément Keller, Jacques Noudem and Eric Hug, Functional properties of a spark plasma sintered ultrafine-grained 316L steel, Mater. and Design 63 (2014) 633.

31. M. Zakeri, M. Ramezani and A. Nazari, Prediction of the Mean Grain Size of MA-Synthesized Nanopowders by Artificial Neural Networks, Mater. Res. 15 (2012) 6.

32. J.B. Nelson and D.P. Riley, An Experimental Investigation of Extrapolation Methods in the Derivation of Accurate Unit-Cell Dimensions of Crystals, Proc. Phys. Soc. 57 (1945) 160.

33. G.K. Williamson and W.H. Hall, X-ray Line Broadening from Filed Aluminium and Wolfram, Acta Metall. 1 (1953) 22.

34. S. Schmauder and C. Kohler, Atomistic simulations of solid solution strengthening of α-iron. Computational Mater. Sci. 50 (4) (2011) 1238.

35. X.T.A. Chu, B.N. Ta, L.T.H. Ngo, M.H. Do, P.X. Nguyen and D.N.H. Nam, Microwave Absorption Properties of Iron Nanoparticles Prepared by Ball-Milling, J. Electron. Mater. 45 (2016) 2311.

36. G.E. Totten, L. Xie, K. Funatani, Handbook of Mechanical Alloy Design, New York, 2003.

37. W.S. Young and I.B. Cutler, Initial sintering with constant rates of heating, J. Am. Ceram. Soc. 53 (1970) 659.

38. J. Guyon, A. Hazotte, J.P. Monchoux and E. Bouzy, Effect of powder state on spark plasma sintering of TiAl alloys, Intermetallics 34 (2013) 94.

39. S. Pasebani, I. Charit, D. P. Butt, J. I. Cole, Y. Wu and J. Burns, Sintering Behavior of Lanthana-Bearing Nanostructured Ferritic Steel Consolidated via Spark Plasma Sintering, Adv. Engg. Mat. 18 (2) (2016) 324.

40. H.J. Frost and M.F. Ashby: Fundamental aspects of structural alloy design, Plenum, 1977.

41. J.S. Lee, J.P. Choi and G.Y. Lee, Consolidation of Hierarchy-Structured Nanopowder Agglomerates and Its Application to Net-Shaping Nanopowder Materials, Mater. 6 (2013) 4046.

42. Garciela B. Reartes, Pedro J. Morando, and Miguel A. Blesa, Reactivity of Chromium Oxide in 1. Aqueous Solutions. 2. Acid Dissolution, Langmuir 11 (1995) 2277.

43. Y. Toshev, V. Mandova, N. Boshkov, D. Stoychev, P. Petrov and N. Tsvetkova, Protective coating of zinc and zinc alloys for industrial applications, International Conference on Multi-Material Micro Manufacture Grenoble, France, 2006.

44. H.W. Hoppe, S. Haupt and H. H. Strehblow, Combined surface analytical and electrochemical study of the formation of passive layers on Fe/Cr alloys in 1M NaOH, Surface and Interface Analysis 21 (1994) 514.

45. G.T. Burstein and D.H. Davis, Reactions of Scratched Copper Electrodes in Aqueous Solutions, J. Electrochem. Soc. 128 (33) (1981) 2270.

46. M. Sanchez, J. Gregori, C. Alonso, J.J. Garcia-Jareno, H. Takenouti and F. Vicente, Electrochemical impedance spectroscopy for studying passive layers on steel rebars immersed in alkaline solutions simulating concrete pores, Electrochim. Acta 52 (2007) 7634.

47. S. Scharrifi-Asl, F. Mao, P. Lu, B. Kursten and D.D. Macdonald, Exploration of the effect of chloride ion concentration and temperature on pitting corrosion of carbon steel in saturated $Ca(OH)_2$ solution, Corros. Sci. 98 (2015) 708.

48. J. Williamson and O.B. Isgor, The effect of simulated concrete pore solution composition and chlorides on the electronic properties of passive films on carbon steel rebar, Corros. Sci. 106 (2016) 82.

49. K.G.U. Wijayantha, S. Saremi-Yarahmadi and L.M. Peter, Kinetics of oxygen evolution at α-Fe2O3 photoanodes: a study by photoelectrochemical impedance spectroscopy, Phys. Chem. Chem. Phys. 13 (2011) 5264.

50. C. B. Carter, M.G. Norton, Ceramic Materials Science and Engineering, 2nd Ed., Springer, New York, 556 (2013).

Chapter 5: Effect of Ceria, Lanthana and Yttria in development of Fe-9Cr Based ODS Alloys via High Energy Ball Milling and Spark Plasma Sintering

Arnab Kundu, Nathan Jerred, Indrajit Charit, Brian Jaques and Chao Jiang

Abstract

Iron, chromium, tungsten and titanium powders were mixed along with different rare earth (RE) oxide powders (lanthana, yttria and ceria) and mechanical alloyed via high energy ball milling for 10 h. The milled powders were analyzed using scanning electron microscopy (SEM) and X-ray diffraction (XRD) for understanding the impact of ball milling time on the characteristics of the milled powder. The milled powder samples were then consolidated via spark plasma sintering (SPS) for 45 min at 1000 ^{O}C at 80 MPa pressure. The density of the consolidated oxide dispersion strengthened (ODS) alloys was found to reach a maximum of 97.2%. The ODS alloy containing Ceria showed the highest hardness of 867 VHN. Microstructural characterization of the SPSed samples using XRD, SEM, and transmission electron microscopy (TEM) revealed nanocrystalline grain structure. Second phase particles such as $Cr_{0.875}Ti_{0.125}$ is observed along with nanometric Ti-Cr-O-RE type precipitates. This study highlights the principles and importance of high energy ball milling and SPS of Fe-9Cr ODS alloy for the future development of more complex ODS alloys.

Keywords: metals and alloys; mechanical alloying; spark plasma sintering; microstructure; XRD; TEM; kinetics

5.1. Introduction

Concepts for the next generation of nuclear power reactors designed to meet increasing world-wide demand for energy include water-cooled, gas-cooled, and liquid-metal-cooled reactors. Depending on operating conditions, some of the designs favour the use of elevated-temperature ferritic/martensitic steels for in-core and out-of-core applications. High chromium (9-14 wt%) alloys are favourable for future sodium fast reactor fuel cladding materials [1-3], which require high radiation swelling resistance and resistance to attack from liquid sodium [4]. Much progress has been made concerning the development of 9Cr based ferritic/martensitic steels. However, their usage is limited to a maximum range of 550–650 °C working temperature due to inferior tensile and creep strength at higher temperature (>700 °C). In order to achieve higher plant operation temperature without losing the merits inherent in ferritic/martensitic steels, efforts have been devoted in developing oxide dispersion strengthened (ODS) steels because of their (a) high, stable dislocation sink strengths and especially large numbers of stable, nanometer-scale precipitates that trap He in fine-scale bubbles to avoid swelling and protect grain boundaries; and (b) high creep strength, permitting operation at temperatures above the displacement damage regime. Oxide dispersion strengthened (ODS) steels based on Fe-(9-14) % Cr alloys are quite promising for such applications. Generally, the processing routes for making such steels involve mechanical alloying that incorporates rare earth (RE) oxides in the base Fe-Cr matrix. Mechanical alloying (MA) is a processing method that involves repeated fracturing, welding and re-fracturing of a mixture of powder particles, generally in a high-energy ball mill, to produce a controlled, extremely fine microstructure, which cannot be easily produced via conventional ingot metallurgy. The milled powder is then consolidated into bulk shapes and heat treated to obtain

the desired characteristics [5]. It has been reported that the morphology, grain size distribution and contamination of the milled powders strongly depend on the process variables in mechanical alloying such as milling time, process control agent (PCA), ball to powder weight ratio (BPR), and milling atmosphere [6-12]. Mechanical alloying is an effective processing technique for producing nanocrystalline materials, amorphous and non-equilibrium phases. During this process, solid solubility significantly increases with increasing energy input. Solid solubility limit is determined by the ratio of intermixing (caused by shear forces) to the decomposition of the solid solution due to thermally activated jumps. If this ratio is very large, a fully random solid solution is achieved. Formation of nanostructures during milling has been established as the most effective mechanism to increase solid solubility due to higher fraction of atoms at the grain boundaries and enhanced (short circuit) diffusion path.

Spark plasma sintering (SPS) is a thermal and pressure assisted compaction/sintering process. It is also known as field assisted sintering technique (FAST) [13] or pulsed electric current sintering (PECS) [14]. This process utilizes a combined action of a pulsed direct electrical current (DC) and pressure to perform high speed consolidation of powder. The direct way of heating allows very high heating rates, thus increasing densification due to enhanced diffusion [15-17]. SPS systems offer many advantages over conventional techniques such as hot pressing (HP), hot isostatic pressing (HIP) or atmospheric furnaces, including ease of operation and accurate control of sintering energy resulting in lower temperature sintering and less time, and applicability to both electrically conductive and non-conductive materials.

Fe-9Cr alloy serves as a base matrix for Fe-9Cr ODS alloy that has attracted much interest [18-19]. Even though higher-Cr ODS alloys have better corrosion/oxidation resistance, they often suffer from thermal aging embrittlement and irradiation embrittlement because of alpha-

prime phase formation [20]. However, Fe-9Cr based ODS steels are relatively free from such effects because of their lower Cr content. Recent development in ODS steels allow them to be used as fuel cladding material in upcoming sodium-cooled fast reactors because oxide particles dispersed in the ferritic or ferritic/martensitic matrix improve the radiation resistance and creep resistance at high temperatures. The ODS steels do not only have the nanosize oxide particles composed of Y–Ti–O atoms but also micron-size grain morphology. The main problem that people have been facing with tube fabrication was in low hoop strength because of elongated fine grains parallel to the rolling/extrusion direction [21]. To solve the problem, ferritic/martensitic 9Cr-ODS steels are being developed. The 9Cr ODS steels have been previously developed by melting, casting and a combined process of MA and extrusion. Although Fe-9Cr ODS alloys have been previously investigated in the areas of microstructural characterization, mechanical properties, voids formation after irradiation, damage structure before and after irradiation [22-29], but only limited work has been reported on using the processing of Fe-9Cr ODS alloy via a combined route of MA and SPS. The work presented here gives us an insight into the importance of MA and SPS process in the development of these nanostructured ferritic ODS alloys. In the present work, we have examined the effect of various rare earth oxides (RE) introducing a new rare earth oxide Ceria.

5.2. Material and Methods

The present study deals with a comparative study of five different alloys which are produced via MA and SPS. The alloys used are shown below in Table 5.1 and 5.2. Tungsten (W) is added as it imparts solid solution strengthening and Titanium (Ti) helps in forming nanoclusters combining with Chromium (Cr) and rare earth (RE) oxides. Same wt % of all

rare earth oxides are added in order to understand the effect of the different RE oxides in Fe-9Cr based ODS alloy.

Table 5.1. Different alloy compositions (in wt %)

Alloy	Composition (wt%)						
	Cr	W	Ti	CeO$_2$	La$_2$O$_3$	Y$_2$O$_3$	Fe
Fe-9Cr	9	-	-	-	-	-	Bal.
Fe-9Cr-3W-0.3Ti	9	3	0.3	-	-	-	Bal.
Fe-9Cr-3W-0.3Ti-0.9CeO$_2$	9	3	0.3	0.9	-	-	Bal.
Fe-9Cr-3W-0.3Ti-0.9La$_2$O$_3$	9	3	0.3	-	0.9	-	Bal.
Fe-9Cr-3W-0.3Ti-0.9Y$_2$O$_3$	9	3	0.3	-	-	0.9	Bal.

Table 5.2. Different alloy compositions according to atom %

Alloy	Composition (Atom%)						
	Cr	W	Ti	CeO$_2$	La$_2$O$_3$	Y$_2$O$_3$	Fe
Fe-9Cr	9.6	-	-	-	-	-	Bal.
Fe-9Cr-3W-0.3Ti	9.8	0.91	0.35	-	-	-	Bal.
Fe-9Cr-3W-0.3Ti-0.9CeO$_2$	9.88	0.92	0.36	0.16	-	-	Bal.
Fe-9Cr-3W-0.3Ti-0.9La$_2$O$_3$	9.88	0.92	0.36	-	0.16	-	Bal.
Fe-9Cr-3W-0.3Ti-0.9Y$_2$O$_3$	9.87	0.92	0.36	-	-	0.23	Bal.

Iron powder (99.9+% metal basis), chromium powder (99.95% metal basis), tungsten powder (99.93+% metal basis), titanium powder (99.92+% metal basis) and rare earth oxides were weighed and poured into a stainless steel vial along with stainless steel balls (milling medium) of 8 mm diameter under an argon atmosphere inside a glove box to prevent oxidation/contamination. No surfactant was added to the milling mixture. The ball to powder weight ratio was around 10:1 [30]. About half of the steel vial was empty after the mixture of powder and steel balls was poured. The filled vials were loaded in a shaker mill (SPEX 8000M) and milled for 10 h. The carbon and nitrogen content of the powders were found to be approximately 0.02 wt% and 0.024 wt%, respectively, as estimated using combustion

analysis. The chromium content of the milled sample was estimated by inductively coupled plasma (ICP) test and found to be around 8.97 wt% which is essentially the target composition (i.e. 9 wt% Cr).

The milled powders were characterized in a Zeiss Supra 35 VP Field-Emission Gun Scanning Electron Microscope (FEG-SEM) to examine the powder size and morphology. X-ray diffraction (XRD) of ball milled powders were performed using Siemens 5000D diffractometer with Cu $K\alpha$ X-ray radiation (wavelength of 0.1541 nm). Modifications such as adaptive smooth, $k\alpha_2$ Rachinger and background correction by Sonnerveld method were applied to XRD patterns using Powder–X software. Using the XRD data, lattice parameter of the milled powders was calculated based on the Nelson–Riley relation [31]. The crystallite size and lattice strain were evaluated using the Williamson–Hall equation [32]:

$$\text{\ss}_{hkl} = 0.94 \, (\lambda/L\cos\theta_{hkl}) + 4\varepsilon\tan\theta_{hkl} \qquad (5.1)$$

where $\text{\ss}_{hkl}$ is the full width half maxima (FWHM) of the XRD peak, L is the crystallite size and ε is the lattice strain. Transmission electron microscopy was performed in JEOL 2010J transmission electron microscope at an accelerating voltage of 200 kV to study the inherent structure of the 10 h milled powder.

A Dr. Sinter Lab SPS-515S (SPS Syntex Inc., Kanagawa, Japan) available at the Center for Advanced Energy Studies (CAES), Idaho Falls, was used to consolidate the milled powder. A Tri-Gemini cylindrical graphite die with an inner diameter of 12.7 mm and outer diameter of 38 mm was used. The inner surface of the die was covered with a graphite foil with a thickness of 0.25 mm to facilitate sample removal. The milled powder was first cold-compacted inside the graphite die, and a 0.2 mm thick graphite foil was placed between the powder and punches. The die was wrapped in a 4 mm thick layer of graphite felt to minimize

heat loss by thermal radiation. Degassing was performed by continually purging argon gas and pumping the chamber down to 7×10^{-3} Torr (9.33×10^{-7} MPa) and repeated at least thrice before starting the sintering process. The milled powder batches were heated in the vacuum chamber to 1000 ^{O}C at a rate of 100 ^{O}C/min and then isothermally held for 45 min. The temperature was monitored with a K-type thermocouple that was inserted through a hole in the die. A constant uniaxial pressure of 80 MPa (~10 kN force) was applied to the milled powder during both heating and dwell time. The samples were then cooled to room temperature in the vacuum chamber at the rate of 50 ^{O}C/min. The final product was in the form of a disk with dimensions of 12.5 mm diameter and 4.8 mm thickness.

The density of the sintered samples was measured by Archimedes principle. The weight of the samples was taken in air and fully immersed condition in deionised water using an Ohaus Precision Balance (HRB-200). The density of deionised water (1 g/cm^3) and the density of air (0.0012 g/cm^3) at standard room temperature and pressure were used for density calculation.

The theoretical density of the sample was calculated based on the composition using the following equation:

$$\rho^{Th} = 100/\sum C_i/\rho_i \qquad (5.2)$$

where, ρ^{Th} is the theoretical density of the sample, ρ_i is the density of components present and C_i is the corresponding weight fraction of corresponding component. The relative density was then estimated in terms of the percentage of theoretical density.

Vickers microhardness tests were performed on all the SPSed samples using a LECO 100M Microhardness Tester using a load of 0.5 kgf (~4.9 N) and a loading time of 15 s at 10

different random points in a given sample. The same X-ray diffractometer was used for analysing the phase constituents and grain size of the SPSed samples. Transmission electron microscopy was also performed using Technai TF30-FEG STEM operating at 300 kV to understand the nanoclusters and precipitates present in the matrix. For preparing TEM specimens, an electro-jet polishing technique was used. A solution of $CH_3OH – HNO_3$ (80:20, by vol.%) was used as electrolyte at –40 ^{O}C and voltage of 25 V using a Fischione Model 110 Twin-Jet Electropolisher. Compression testing was performed at room temperature and 700 ^{O}C under a strain rate of 10^{-3} s^{-1} using an Instron 5982 universal tester.

5.3. Results

In order to understand the Fe-9Cr ODS alloy system, one should perceive every aspect starting right from the beginning i.e. fabrication.

5.3.1. Characteristics of the Milled Fe-9Cr and Fe-9Cr ODS Powders

The as received and milled powder batches were examined by SEM to obtain an understanding of the powder size and morphology. Figures 5.1(a) – (g) show the secondary electron (SE) images of the as received iron, chromium, tungsten, titanium, ceria, lanthana and yttria, respectively. The mean powder size of the as received powders are tabulated in Table 5.3.
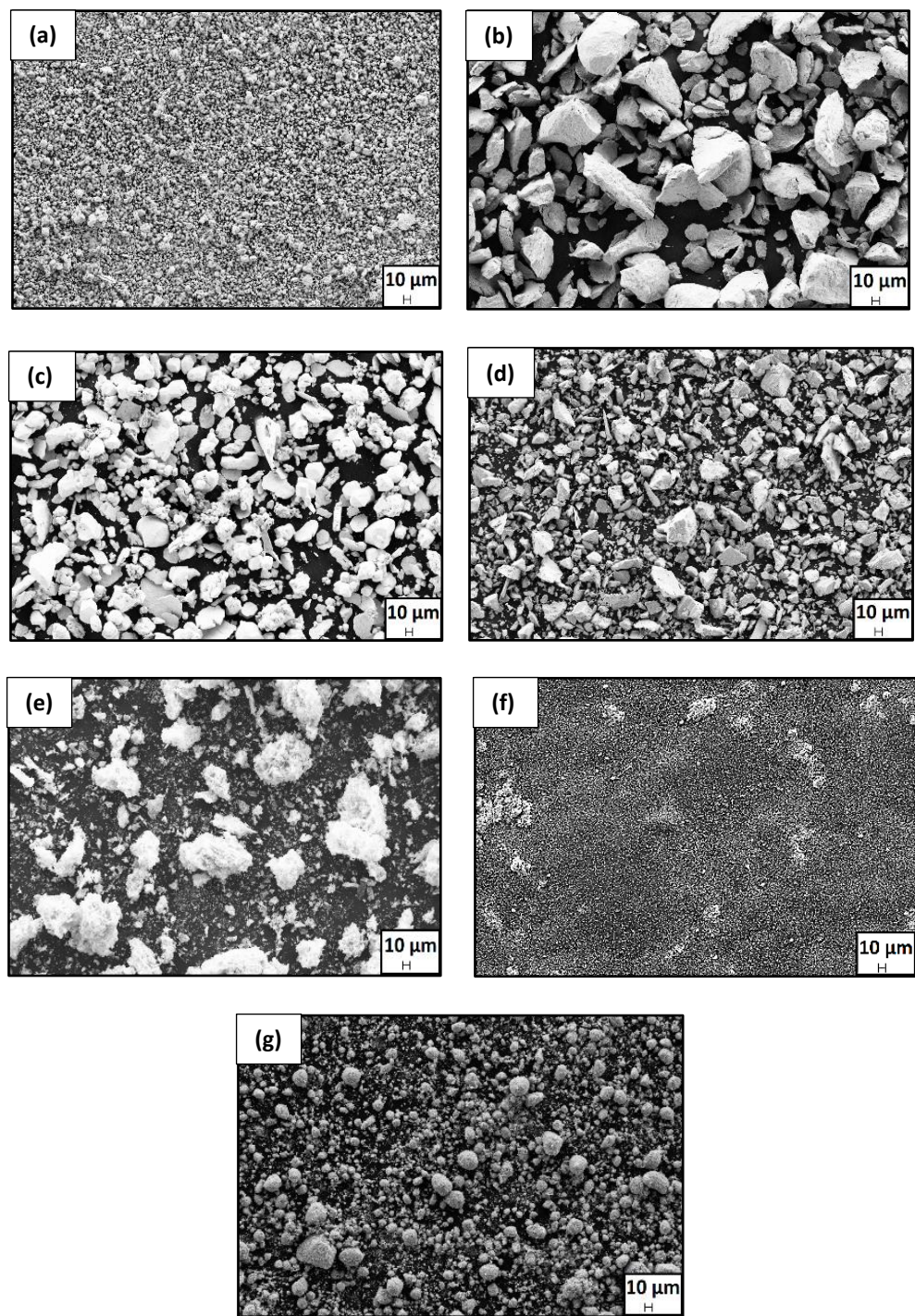
Figure 5.1. SE images of 10 hr ball milled powders for the alloys: (a) Fe, (b) Cr, (c) W, (d) Ti, (e) CeO_2, (f) La_2O_3 and (g) Y_2O_3

Table 5.3. Mean powder size of the as received powders

Powder	Fe	Cr	W	Ti	CeO_2	La_2O_3	Y_2O_3
Mean Powder Size(µm)	12 ± 3	30 ± 15	15 ± 5	17 ± 8	$0.1 \pm .02$	$0.2 \pm .015$	$0.15 \pm .01$

Figures 5.2 (a)-(e) represent the SE SEM images of 10 hr milled powder batches for each of the alloys Fe-9Cr, Fe-9Cr-3W-0.3Ti, Fe-9Cr-3W-0.3Ti-0.9CeO_2, Fe-9Cr-3W-0.3Ti-0.9La_2O_3 and Fe-9Cr-3W-0.3Ti-0.9Y_2O_3, respectively. The powder size distribution shows a bimodal structure for each of the alloys, though the bimodality characteristics increases with the addition of rare earth oxides as seen in Figures 5.2(c)-(e).
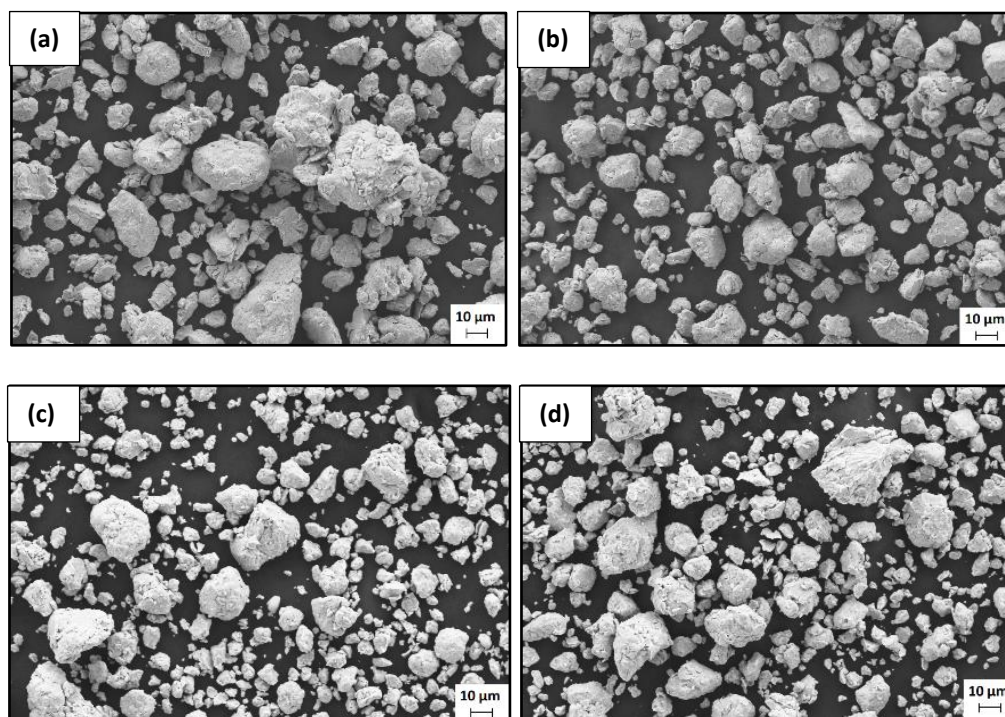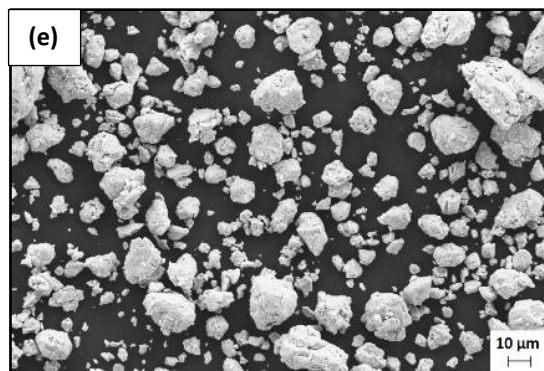
Figure 5.2. SE-SEM images of 10 hr ball milled powders for the alloys: (a) Fe-9Cr, (b) Fe-9Cr-3W-0.3Ti (c) Fe-9Cr-3W-0.3Ti-0.9CeO$_2$, (d) Fe-9Cr-3W-0.3Ti-0.9La$_2$O$_3$ and (e) Fe-9Cr-3W-0.3Ti-0.9Y$_2$O$_3$

Powder size analysis revealed that the mean powder size decreased with addition of alloying elements and rare earth oxides as shown in Figure 5.3. Also, it can be noted that the powder size distribution became progressively broader.
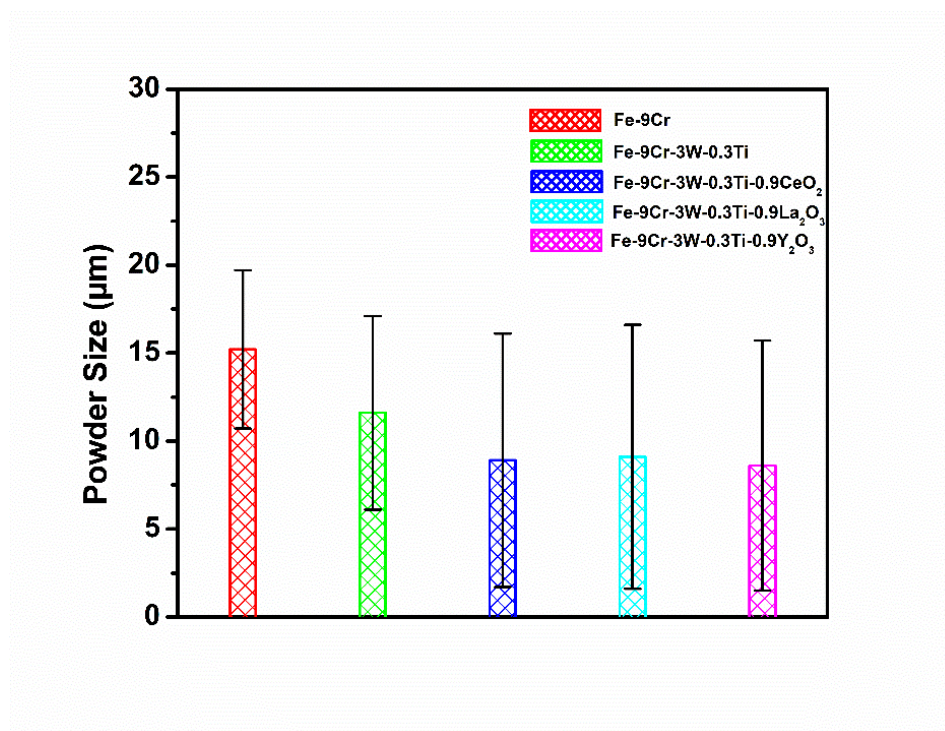
Figure 5.3. The variation of powder size for Fe-9Cr ODS powder batches milled for 10 hr

Figure 5.4 shows the XRD patterns of the various milled powder samples. Prominent peaks are observed near the diffraction angles (2θ) of 44.91^0, 65.46^0 and 82.57^0. These peaks correspond to the planes {110}, {200} and {211} of BCC iron, respectively [33].
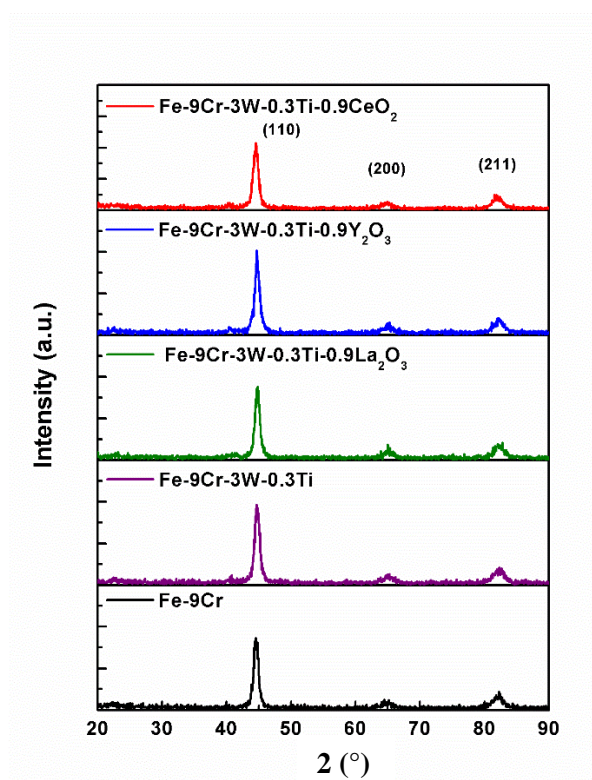
Figure 5.4. X-ray diffraction patterns of 10 hr milled Fe-9Cr ODS powder batches

Table 5.4 shows the variation of lattice parameter, crystallite size and lattice strain with ball milling time.

Table 5.4. Lattice parameter, crystallite size and lattice strain of the Fe-9Cr powder batches ball milled for various durations, as calculated from the XRD data

Alloy	Lattice Parameter (Å)	Crystallite Size (nm)	Strain (%)
Fe-9Cr	2.89 ± 0.01	11.34 ± 0.02	0.84 ± 0.01
Fe-9Cr-3W-0.3Ti	2.88 ± 0.01	36.25 ± 0.02	0.85 ± 0.02
Fe-9Cr-3W-0.3Ti-0.9CeO$_2$	2.87 ± 0.01	27.36 ± 0.03	0.78 ± 0.02
Fe-9Cr-3W-0.3Ti-0.9La$_2$O$_3$	2.87 ± 0.02	24.17 ± 0.01	0.72 ± 0.02
Fe-9Cr-3W-0.3Ti-0.9Y$_2$O$_3$	2.87 ± 0.02	25.34 ± 0.04	0.73 ± 0.02

5.3.2. Characteristics of Spark Plasma Sintered Fe-9Cr and Fe-9Cr ODS Samples

5.3.2.1. Evaluation of density and microhardness

In this section, results of SPSed Fe-9Cr ODS alloys are presented. Table 5.5 shows the variation of relative density and Vickers microhardness of the sintered samples. The relative density decreases by a little with addition of the oxides and alloying elements while the Vickers microhardness increases drastically.

Table 5.5. Relative Density and Vickers Microhardness of the SPSed Fe-9Cr ODS alloys

Alloy	Relative Density (%)	Vickers Microhardness (VHN)
Fe-9Cr	97.9 ± 0.1	461.2 ± 3.7
Fe-9Cr-3W-0.3Ti	97.8 ± 0.1	703.5 ± 4.2
Fe-9Cr-3W-0.3Ti-0.9CeO$_2$	97.2 ± 0.1	867.1 ± 4.4
Fe-9Cr-3W-0.3Ti-0.9La$_2$O$_3$	97.6 ± 0.1	791.9 ± 5.3
Fe-9Cr-3W-0.3Ti-0.9Y$_2$O$_3$	97.1 ± 0.1	786.4 ± 4.1

5.3.2.2. Microstructural characteristics

SEM images of Fe-9Cr and Fe-9Cr-3W-0.3Ti alloys are shown in Figures 5.5 (a) and (b). The SEM micrographs of the SPSed Fe-9Cr ODS alloys are shown in Figure 5.5 (c) – (e). Grain size analysis was done using the mean linear intercept method. The average grain sizes are shown in Table 5.6.
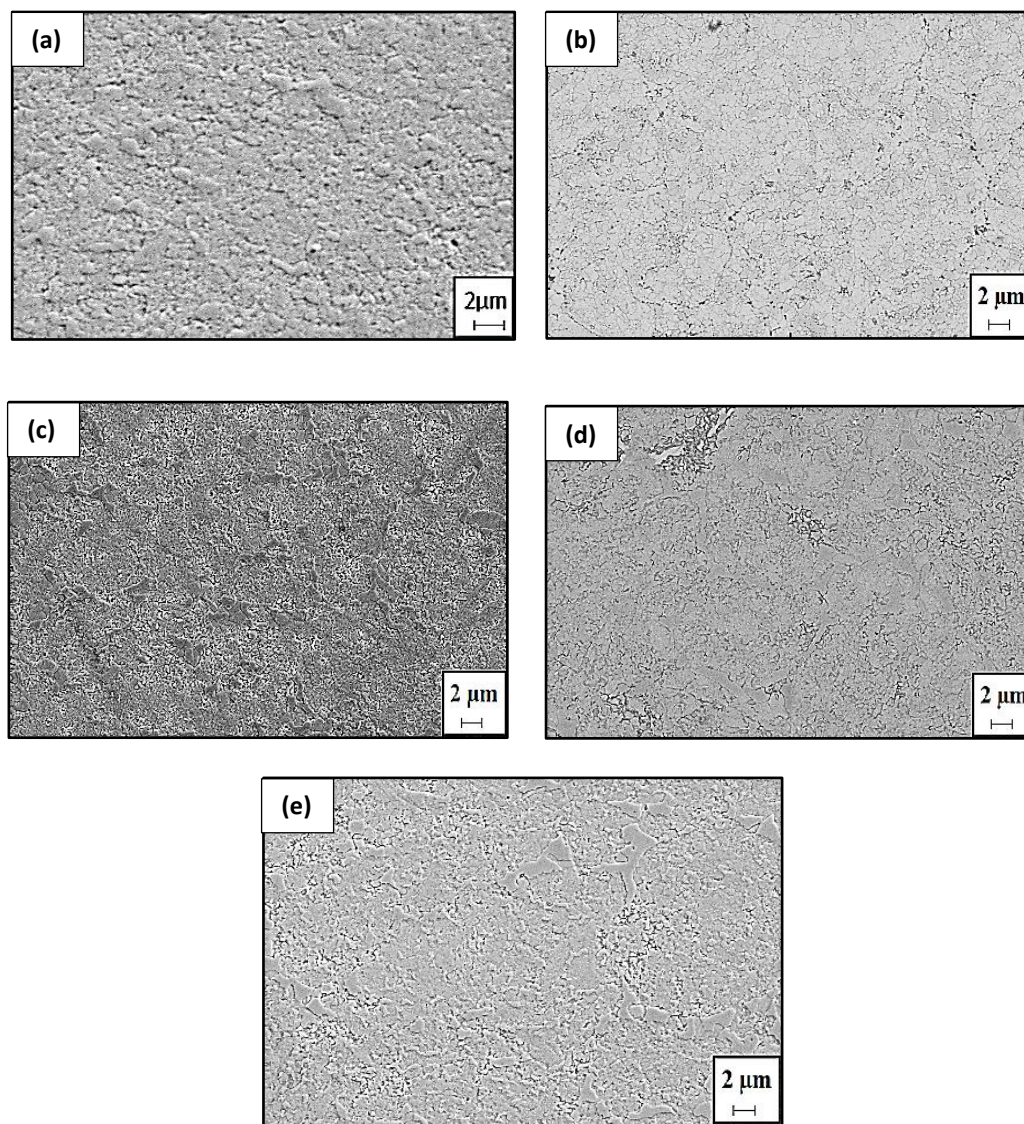
Figure 5.5. SEM images of (a) Fe-9Cr; (b) Fe-9Cr-3W-0.3Ti, (c) Fe-9Cr-3W-0.3Ti-0.9CeO$_2$, (d) Fe-9Cr-3W-0.3Ti-0.9La$_2$O$_3$, and (e) Fe-9Cr-3W-0.3Ti-0.9Y$_2$O$_3$.

Table 5.6. Grain size analysis of the SPSed Fe-9Cr ODS alloys

Alloy	Grain Size (μm)
Fe-9Cr	1.9 ± 1.2
Fe-9Cr-3W-0.3Ti	2.1 ± 1.4
Fe-9Cr-3W-0.3Ti-0.9CeO$_2$	0.22 ± 0.15
Fe-9Cr-3W-0.3Ti-0.9La$_2$O$_3$	0.25 ± 0.12
Fe-9Cr-3W-0.3Ti-0.9Y$_2$O$_3$	0.23 ± 0.13

Figures 5.6 (a)-(b) show bright field TEM images of the SPSed Fe-9Cr and Fe-9Cr-3W-0.3Ti ODS samples. The figures show fine grain size (2 µm) in Fe-9Cr alloy. With addition of the alloying elements and the rare-earth oxides, the grain size is decreased to submicron level. The grain size is comparable with that obtained by the previously described SEM studies. A lot of precipitates are observed for the ODS alloys compared to base Fe-9Cr matrix, which are due to the addition of the rare earth oxide particles.
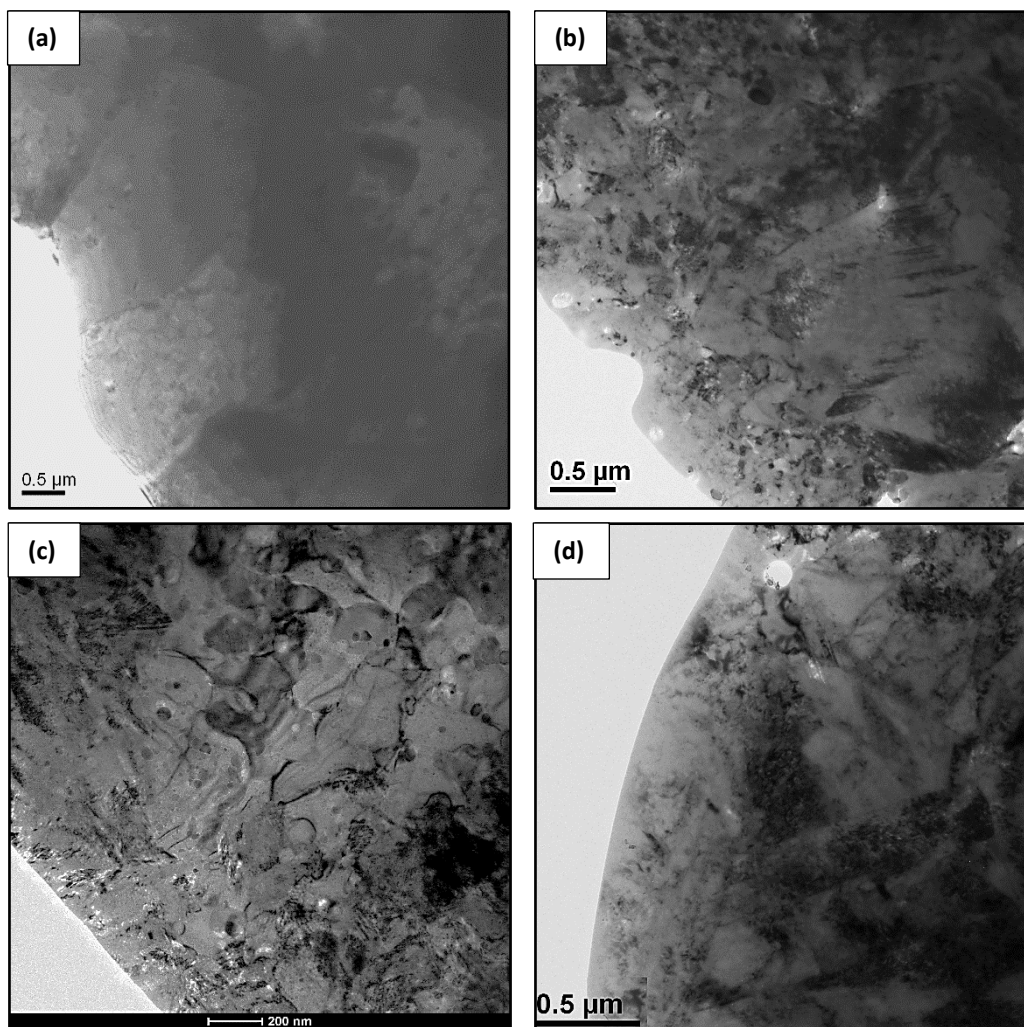
Figure 5.6. TEM images of the alloys: (a) Fe-9Cr, (b) Fe-9Cr-3W-0.3Ti-0.9CeO$_2$, (c) Fe-9Cr-3W-0.3Ti-0.9La$_2$O$_3$ and (d) Fe-9Cr-3W-0.3Ti-0.9Y$_2$O$_3$.

High angle-annular dark field (HAADF) imaging is used for understanding the nature and distribution of the precipitates present in the Fe-9Cr-3W-0.3Ti-0.9CeO$_2$, Fe-9Cr-3W-0.3Ti-0.9La$_2$O$_3$ and Fe-9Cr-3W-0.3Ti-0.9Y$_2$O$_3$ alloys and corresponding EDS spectra are shown in Figure 5.7 (a)-(f). The Fe-9Cr-3W-0.3Ti-0.9Y$_2$O$_3$ shows a large number density of precipitates compared to the other two ODS alloys. The precipitate size is also smaller for Y$_2$O$_3$ compared two others. The Fe-9Cr-3W-0.3Ti-0.9La$_2$O$_3$ has a large volume fraction of precipitates compared to the other ODS alloys. However, the precipitate size is the largest in case of Fe-9Cr-3W-0.3Ti-0.9CeO$_2$ alloy.
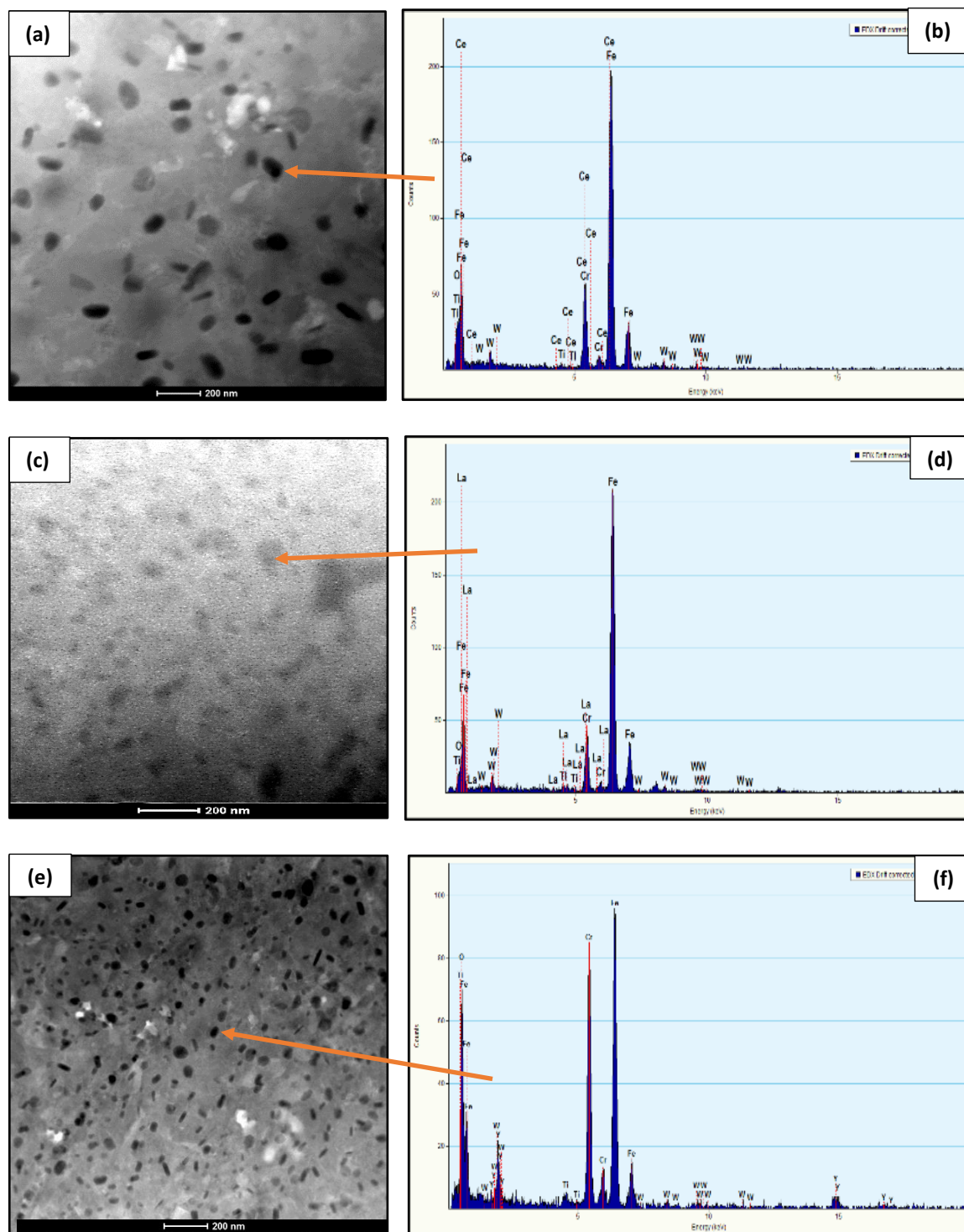
Figure 5.7. Drift-corrected HAADF-STEM image and corresponding EDS of the alloys: (a)-(b) Fe-9Cr-3W-0.3Ti-0.9CeO$_2$, (c)-(d) Fe-9Cr-3W-0.3Ti-0.9La$_2$O$_3$, (e)-(f) Fe-9Cr-3W-0.3Ti-0.9Y$_2$O$_3$

Figure 5.8(a) shows the line scan of a precipitate of Fe-9Cr-3W-0.3Ti-0.9Y$_2$O$_3$ alloy

in HAADF-STEM mode. Figure 5.8(b) shows the corresponding EDS spectrum of the line

scan of a single precipitate. The spectrum shows that as one traverses into the precipitate following the red line from left to right in Figure 5.8(a), the concentration of chromium (Cr), titanium (Ti), yttrium (Y) and oxygen (O) increases whereas the concentration of iron (Fe) and tungsten(W) decreases.
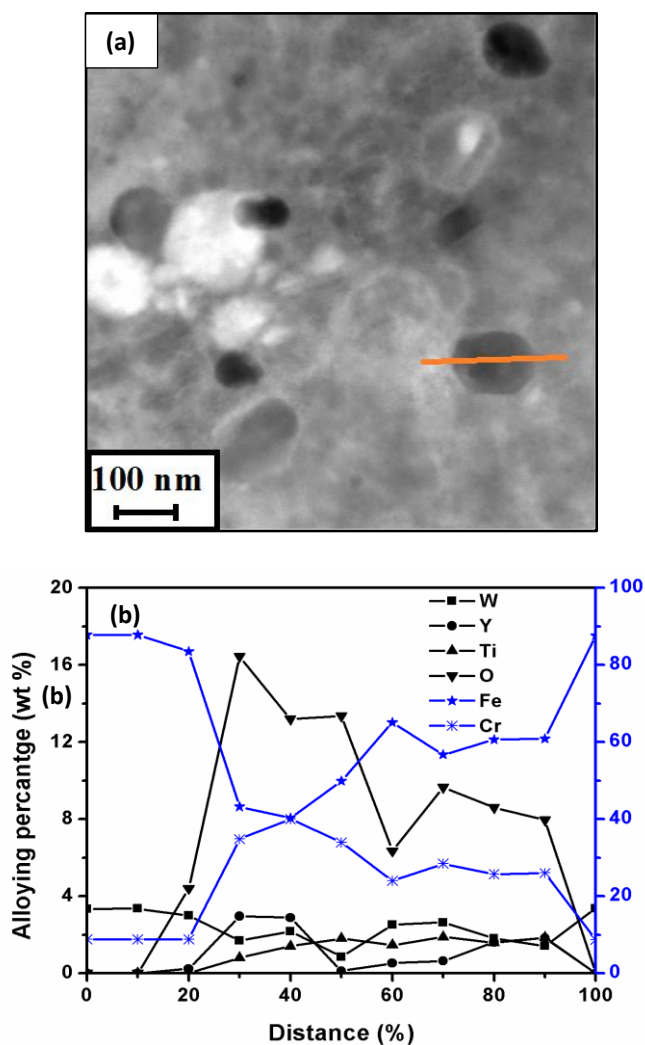
Figure 5.8 (a): Drift-corrected HAADF-STEM image of the alloy and (b) the corresponding line EDS spectrum of a precipitate in the matrix.

This is a conclusive evidence that the precipitates formed are Ti-Cr-O-RE types oxides. Similar EDS compositional line scan profiles have been done for the other ODS alloys and similar observations have been made.

Figure 5.9 shows the XRD pattern of the SPSed alloys. The pattern shows the presence of ferrite that has a body centred cubic (BCC) structure. Also, presence of a second phase is observed on addition of W and Ti. This second phase is identified as a complex compound of Cr and Ti which is $Cr_{0.875}Ti_{0.125}$.
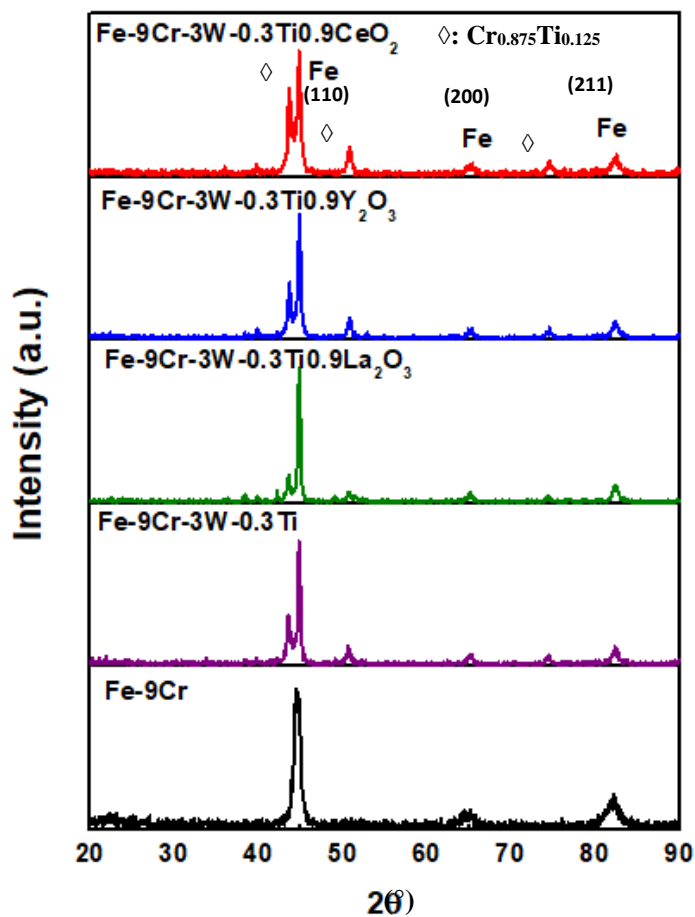
Figure 5.9. XRD patterns of the SPSed Fe-Cr alloys

The presence of this second phase Cr-Ti complex also makes the matrix harder as evidenced in higher microhardness values of the Fe-9Cr-3W-0.3Ti and three Fe-9Cr-3W-0.3Ti-RE ODS alloys than the Fe-9Cr alloy.

5.3.2.3. Evaluation of compression properties

Compressive true stress – true plastic strain curves of the SPSed Fe-9Cr, Fe-9Cr-3W-0.3Ti, and three ODS alloys at two different temperatures (room temperature and 700 ^{O}C) are shown in Figure 5.10 (a)-(b) respectively.
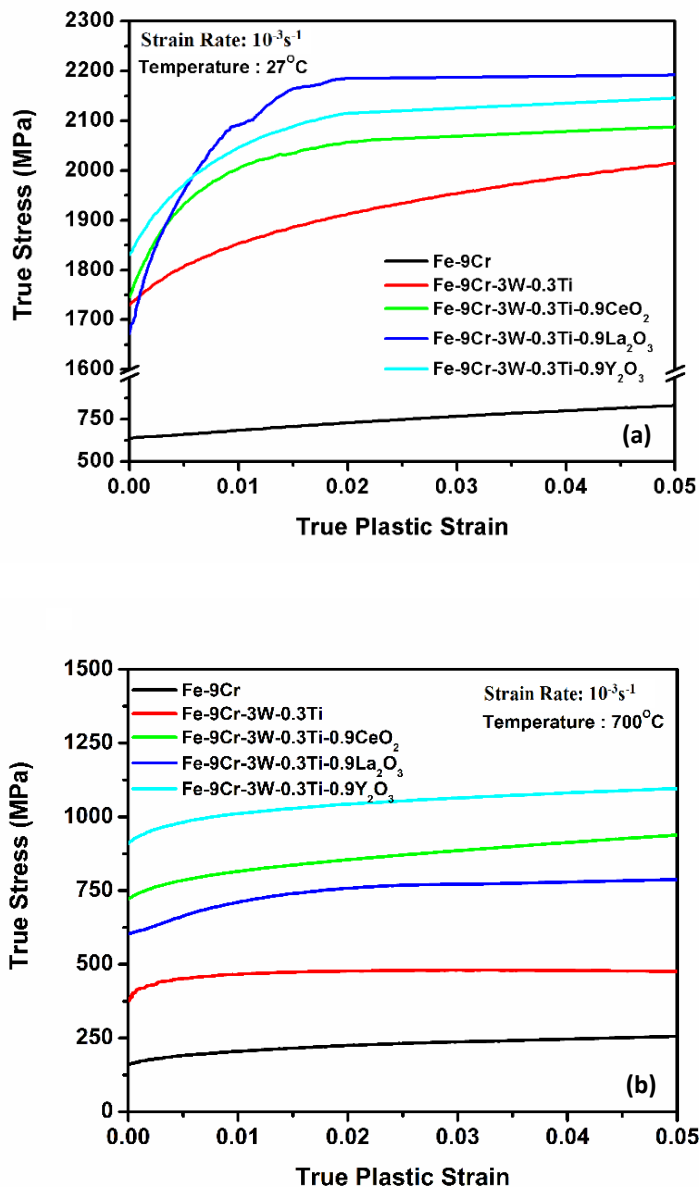
Figure 5.10. Compression true stress vs. true plastic strain curves of the various Fe-9Cr based alloy sample at (a) 27 ^{O}C and (b) 700 ^{O}C.

From the figures, the yield stress was determined and listed in Table 5.7. Here the yield stresses are defined as the true stress at the initiation of plastic flow.

Table 5.7. Yield stress values of Fe-9Cr ODS alloys at 27 $^{\circ}$C and 700 $^{\circ}$C

Alloy	Yield Stress (MPa)	
	27 $^{\circ}$C	700 $^{\circ}$C
Fe-9Cr	642	162
Fe-9Cr-3W-0.3Ti	1736	377
Fe-9Cr-3W-0.3Ti-0.9CeO$_2$	1745	726
Fe-9Cr-3W-0.3Ti-0.9La$_2$O$_3$	1682	604
Fe-9Cr-3W-0.3Ti-0.9Y$_2$O$_3$	1829	914

Two models, Hollomon [34] and Ludwik [35], have been fitted for the analysis of strain hardening exponent (*n*) as given by the equations 5.3 and 5.4 respectively,

$$\sigma = k\left(\varepsilon_p\right)^n \quad (5.3)$$

$$\sigma = \sigma_y + k\left(\varepsilon_p\right)^n \quad (5.4)$$

where σ is the stress, k is the strength coefficient and ε_p is the plastic strain. The values of the strain hardening exponent according to different models are shown in the Tables 5.8 and 5.9.

Table 5.8. Strain hardening exponent value of Fe-9Cr ODS alloys at 27 $^{\circ}$C

Alloy	Strain Hardening Exponent (n)	
	Hollomon	Ludwik
Fe-9Cr	0.118 ± 0.003	0.88 ± 0.01
Fe-9Cr-3W-0.3Ti	0.066 ± 0.005	0.62 ± 0.02
Fe-9Cr-3W-0.3Ti-0.9CeO$_2$	0.051 ± 0.002	0.69 ± 0.01
Fe-9Cr-3W-0.3Ti-0.9La$_2$O$_3$	0.077 ± 0.004	0.75 ± 0.03
Fe-9Cr-3W-0.3Ti-0.9Y$_2$O$_3$	0.052 ± 0.002	0.71 ± 0.02

Table 5.9. Strain hardening exponent value of Fe-9Cr ODS alloys at 700 $^{\circ}$C

Alloy	Strain Hardening Exponent (n)	
	Hollomon	Ludwik
Fe-9Cr	0.091 ± 0.003	0.76 ± 0.02
Fe-9Cr-3W-0.3Ti	0.039 ± 0.005	0.54 ± 0.02
Fe-9Cr-3W-0.3Ti-0.9CeO$_2$	0.053 ± 0.004	0.52 ± 0.03
Fe-9Cr-3W-0.3Ti-0.9La$_2$O$_3$	0.064 ± 0.00	0.59 ± 0.01
Fe-9Cr-3W-0.3Ti-0.9Y$_2$O$_3$	0.037 ± 0.003	0.55 ± 0.02

5.3.3. Spark Plasma Sintering Kinetics

In order to understand the SPS kinetics, the model proposed by Young and Cutler [36] has been used. In their study, non-isothermal equations for volume and grain boundary diffusion have been modified. The equations represent the relationship between the shrinkage (Y) and diffusion coefficient (D), where c represents the heating ramp rate in units of K.s^{-1} [36]:

$$ln(YT\frac{dY}{dT}) = ln(\frac{2.63\gamma\Omega D_o^V}{ka^3c}) - \frac{Q_V}{RT} \qquad (5.5)$$

$$ln(Y^2T\frac{dY}{dT}) = ln(\frac{0.71\gamma b\Omega D_o^B}{ka^4c}) - \frac{Q_B}{RT} \qquad (5.6)$$

where Y is the linear shrinkage ($\Delta l/l_o$), Ω is the volume of vacancy (m^3), γ is the surface energy (J/m^2), D_V is the volume diffusion coefficient given by $D_V = D_0{}^V \exp(-Q_V/RT)$ (m^2.s^{-1}), bD_B is the product of the grain boundary thickness 'b' and grain boundary diffusion coefficient 'D_B' given by $bD_B = bD_0{}^B \exp(-Q_B/RT)$ (m^3.s^{-1}), k is the *Boltzmann* constant (J/K), T is the temperature (K), a is the particle radius (m) and t is time (s). Q_V and Q_B are the activation energy for volume diffusion and grain boundary diffusion, respectively. The activation energies for volume diffusion and grain boundary diffusion can be obtained from

the slope of the plots between ln $(YT(\mathrm{d}Y/\mathrm{d}T))$ versus $1/T$ and ln $(Y^2T(\mathrm{d}Y/\mathrm{d}T))$ versus $1/T$, respectively.

Figure 5.11 depicts the displacement profile curve of the SPSed sample. Constant heating
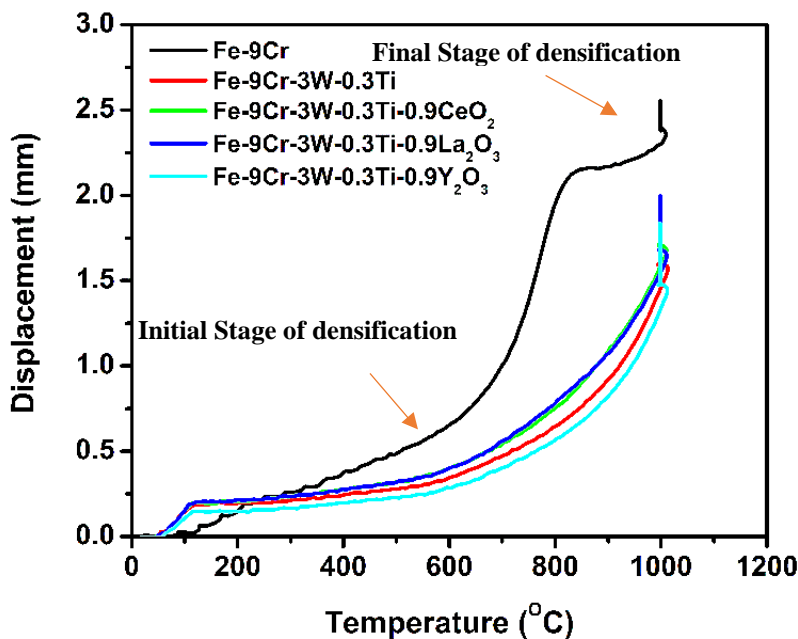
Figure 5.11. Displacement profile curve of different alloy samples sintered at 1000 ^{O}C for 45 min under a pressure of 80 MPa.

Rate has been used during the SPS process. The temperature at which densification begins (T_s) and the temperature at which maximum densification rate occurs (T_{max}) are calculated from the displacement curve and its first derivative, respectively [37]. From the data obtained, it has been seen that the densification starts around 600 ^{O}C and reaches the maximum densification rate around 825 ^{O}C for simple Fe-9Cr system which is close to the value obtained by previous studies [38]. But for Fe-9Cr ODS alloys prolonged densification time is required.
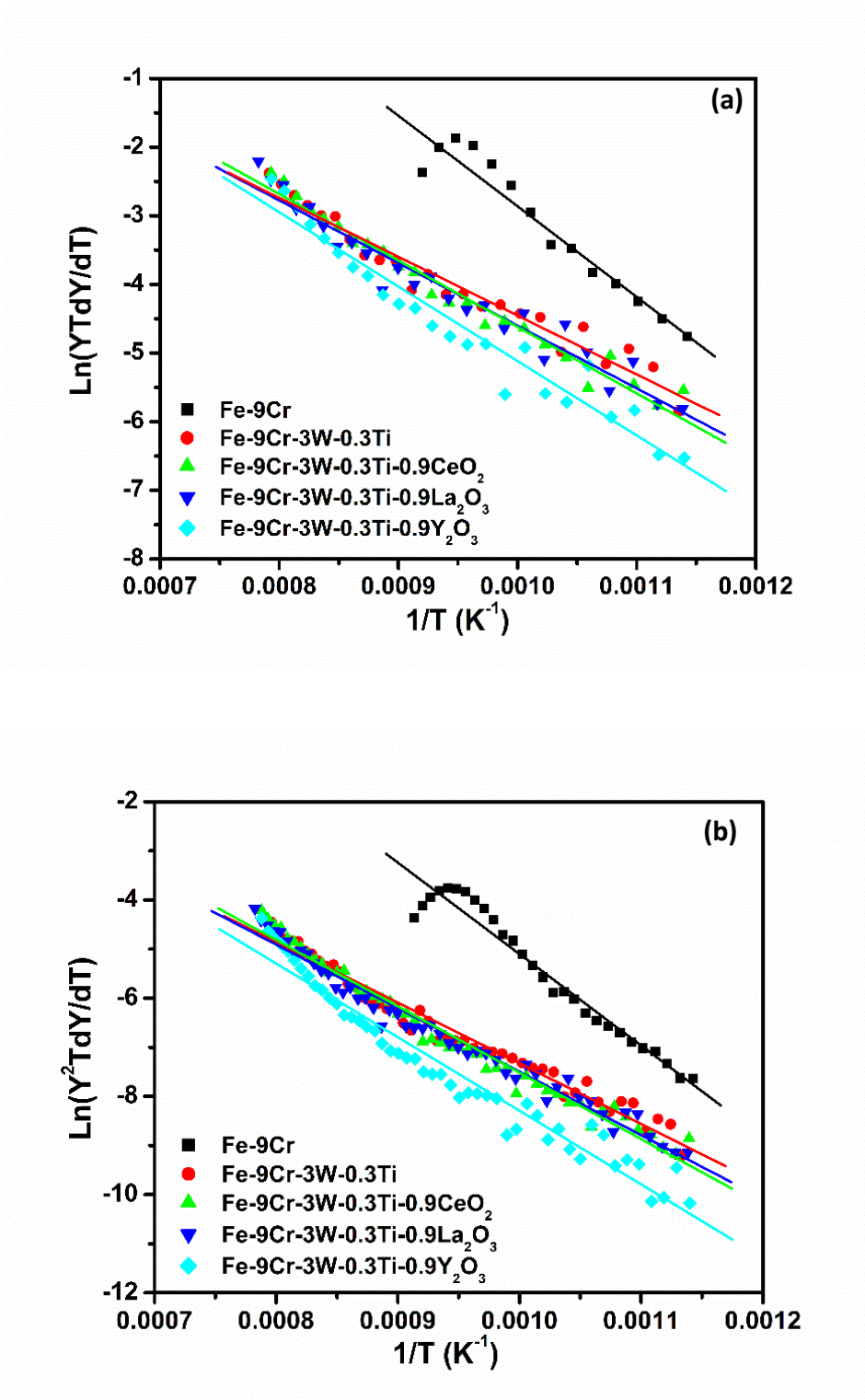
Figure 5.12. Activation energy profiles for (a) volume diffusion, and (b) grain boundary diffusion of the Fe-9Cr alloy sample sintered at 1000 ^{O}C for 45 min under a pressure of 80 MPa.

From the slope of the ln (YT dY/dT) versus 1/T plots shown in Figure 5.12(a), the volume diffusion activation energy for the Fe-9Cr ODS alloys sintered at 1000 ^{O}C was estimated. From the slope of the ln (Y^2T dY/dT) versus 1/T plots shown in Figure 12(b), the grain boundary diffusion activation energy for the Fe-9Cr ODS alloys was estimated. The values of the T_s, T_{max}, Q_V and Q_B are shown in Table 5.10.

Table 5.10. Kinetic Parameters of Fe-9Cr ODS alloys as calculated from displacement data during SPS

Sample description	Sintering Start Temperature (T_S) (^{O}C)	Sintering Finish Temperature (T_{max}) (^{O}C)	Activation Energy for Volume diffusion (Q_V) (Kjmol^{-1}K^{-1})	Activation Energy for Grain Boundary diffusion (Q_B) (Kjmol^{-1}K^{-1})
Fe-9Cr	600	825	130.1	170.3
Fe-9Cr-3W-0.3Ti	550	950	71.3	102.7
Fe-9Cr-3W-0.3Ti-0.9CeO$_2$	550	1000	80.5	112.3
Fe-9Cr-3W-0.3Ti-0.9La$_2$O$_3$	550	1000	75.9	107.5
Fe-9Cr-3W-0.3Ti-0.9Y$_2$O$_3$	575	1000	90.1	124.6

5.4. Discussion

The as received powders varied in their powder size ranging from 30 µm to around 150 nm as shown in Table 5.3. When the powders are milled for 10 hrs in the shaker mill, it yielded powder particles of varying sizes, Figure 5.3. The mean size of the milled powder decreased with the addition of alloying elements and oxide particles in the parent Fe-9Cr matrix. The reason behind this is that during the process of ball milling, the alloying elements

become solid solutionized into the parent material. According to solid-solution hardening equation [39],

$$\sigma_{SS} = \sum A_i\, C_i \qquad (5.7)$$

the addition of alloying elements like W and Ti increases the hardness of the matrix. But the scenario is different with the introduction of rare earth oxides. With the introduction of rare earth oxides, titanium starts forming complexes with them due to the high Ti-O affinity [40]. On addition of La_2O_3, complex precipitates of Cr-Ti-La-O are formed during the process of high energy ball milling. Pasebani et al. [41] reported that after high energy ball milling, La_2O_3 got decomposed and La and O were incorporated in the ferritic matrix substitutionally and interstitially, respectively. The decomposition was suggested to be due to the repeated fracture and shearing of the fragmented oxide particles. Also, with the addition of Y_2O_3, Y–Ti–Cr–O nanostructures are produced during high energy ball milling as reported elsewhere [42]. But the effect of CeO_2 is still to be understood as not much work has been done on CeO_2 based ODS materials. The formation of the nanoclusters and also the subsequent solid solutionizing increases the strength of the powder particles and thus with repeated impact during the mechanical alloying process, instead of getting deformed more, the hardened particles breaks down in smaller particles thus decreasing the effective mean powder size, as shown in Figure 5.3. As discussed before, the introduction of these alloying elements (W, Ti) increases the strength, resulting in higher mean powder size of the Fe-9Cr powder than the corresponding Fe-9Cr-3W-0.3Ti powder. With the further introduction of rare earth oxides, due to the formation of the nanoclusters, the powder gets further hardened and becomes much more brittle in nature than the Fe-9Cr-3W-0.3Ti powder, resulting in further decrease of powder size. Since the atomic percentage of CeO_2 and La_2O_3 present are similar, it can be

inferred that their powder sizes are quite comparable. But due to the presence of higher atomic percentage of Y_2O_3, the powder gets hardened more than the corresponding CeO_2 and La_2O_3 powders, resulting in further reduction in mean powder size.

From the X-Ray diffraction analysis of the milled powder, only prominent peaks of the BCC structure are observed due to the presence of the BCC iron. No additional peak of other alloying elements is observed from which one can deduce that the alloying elements have undergone solid solutionizing into the ferritic matrix. The lattice parameter as obtained from the XRD data is 2.88 ± 0.001 Å, which is in between that of iron (2.87 Å) and chromium (2.89 Å). The variation in crystallite size is something interesting to look upon. Fe-9Cr powder has lower crystallite size whereas the Fe-9Cr-3W-0.3Ti powder has higher one. The reason behind this can be that Fe-9Cr powder being softer than Fe-9Cr-3W-0.3Ti, got deformed more due to self-impact and with the balls in the vial during milling resulting in lower crystallite size although having comparable amount of lattice strain. On the introduction of rare earth oxides, the matrix becomes more strengthened compared to Fe-9Cr-3W-0.3Ti as stated before. Thus, because of the impact during milling, the Fe-9Cr ODS powder breaks down into smaller particles resulting in smaller crystallite size with a decrease in lattice strain due to the relaxation after breaking as compared with Fe-9Cr-3W-0.3Ti counterpart.

The consolidated alloys show comparable relative density. Although the density decreases a little bit due to the addition of rare earth oxides as shown in Table 5.5, the density values of the ODS alloys should have been higher compared to the counterpart Fe-9Cr-3W-0.3Ti, since they had smaller powder size. Smaller powder size leads to higher densification at constant operating parameters in SPS as seen from previous studies [41]. But in this

scenario, the density is following the reverse trend. The reason for this is explained in the next paragraph.

Although the relative density is decreasing, a drastic increase in the microhardness is observed with the addition of W, Ti as compared to the base Fe-9Cr matrix. The reason behind this is the effect of the solid solution strengthening mechanism as discussed before. With the further introduction of rare earth oxides, the hardness increases. The rare earths form nanometric precipitates as discussed before. These nanoclusters actually retard the grain growth by pinning the dislocation movement as reported previously [43]. Addition of rare earth oxides leads to smaller grain sizes as seen from the secondary electron and backscattered electron imaging shown in Figure 5.7. From Table 5.6, it is observed that grain size does not vary much between Fe-9Cr and Fe-9Cr-3W-0.3Ti, but with the addition of rare earth oxides the grain size decreases to submicron level. The TEM images also depicts a similar scenario. The presence of very fine precipitates is found in the ODS alloys. From the HAADF-STEM images, Fe-9Cr-3W-0.3Ti-0.9Y$_2$O$_3$ shows the largest number density of precipitates compared to the other two ODS alloys, which is likely due to the presence of higher atomic percentage of Y$_2$O$_3$. The precipitate size is also small for Y$_2$O$_3$ compared to two others. The Fe-9Cr-3W-0.3Ti-0.9La$_2$O$_3$ has a large volume fraction of precipitates compared to the other ODS alloys. However, the precipitate size is the largest in case of Fe-9Cr-3W-0.3Ti-0.9CeO$_2$ alloy which results in higher microhardness of the alloy compared to the others as seen from Table 5.5. The precipitates present in the ODS material is of complex structure consisting of Ti-Cr-O-RE composition as seen from the EDS spectrum in Figure 5.8(b). Also, from the XRD analysis of the SPSed material, presence of BCC ferritic structure is obtained. Also, some phase rich in Cr$_{0.875}$Ti$_{0.125}$ are also observed as seen in Figure 5.10. These second phase

particles along with the addition of tungsten, makes the matrix of the Fe-9Cr-3W-0.3Ti stronger than the Fe-9Cr matrix resulting in higher microhardness. Tungsten is known to be one of the potent solid solution hardeners in iron. This also results in higher yield strength of the Fe-9Cr-3W-0.3Ti than Fe-9Cr matrix at 27 ^{O}C and 700 ^{O}C, as seen from Table 5.7. Since the Fe-9Cr-3W-0.3Ti-0.9La$_2$O$_3$ alloy has the largest volume fraction of precipitates, the yield strength of this alloy at room temperature is the highest. Comparing between CeO$_2$ and Y$_2$O$_3$ containing ODS alloys, since the later has higher number of precipitates than the other, the latter has higher strength than the other both at 27 ^{O}C and 700 ^{O}C. However, there are a number of mechanisms involved for strengthening at high temperatures but that analysis is beyond the scope of the present study.

From the kinetic data it seems most likely that although Fe-9Cr alloy has reached the final stage of sintering resulting in higher relative density, whereas the other alloys have not as no final stage of densification is observed according to Figure 5.11. The alloys on addition of W, Ti and RE still need more time for reaching its final stage of densification that will achieve less porosity. The analysis from Young and Cutler equation shows the addition of W, Ti and RE decreases the grain boundary diffusion activation energy as shown in Table 5.10, thus enabling the process of sintering for these alloys to start at a lower temperature than the Fe-9Cr counterpart. Because of the presence of second phase particles and oxide particles in the matrix, charge accumulation occurs which results in rapid heating on the matrix thus decreasing the activation energy for the other alloys with respect to Fe-9Cr alloy. However, the grain boundary activation energy increases with addition of oxide particles. The plausible reason for this could be the preponderance of boundaries due to the nanocrystalline crystallite size produced during MA. However, during SPS, various mechanisms can occur as reported

in previous studies [14]. In the initial phase, surface diffusion is the dominant mechanism because electric charge is concentrated mainly on the outer surface of the particles leading to capacitive nature between two nearby particles thus producing enough heat for the surface diffusion to take place. In the later stage when enough particles have fused together, the volume diffusion might come into play but the exact mechanism of the final stage of densification is yet unknown.

5.5. Conclusions

The main objective of this study was to develop a fabrication route for Fe-9Cr ODS alloy by high energy ball milling and spark plasma sintering. Also, the effect of addition of alloying elements (W and Ti) and RE oxides (ceria, lanthana and yttria) are investigated. The following salient features are observed:

1. Addition of alloying elements that exhibit solid solution hardening increase the powder size during ball milling. Addition of RE oxides, on the contrary, decreases the powder size.

2. On addition of RE oxides, both crystallite size and lattice strain decrease for the same duration of ball milling.

3. Addition of alloying elements and RE oxides to the base matrix requires more time for densification.

4. Decrease in grain boundary diffusion activation energy is noted with addition of alloying elements and RE oxides, thus enabling sintering to start at lower temperature.

5. The process of SPS shows that the densification occurs more due to grain boundary diffusion than volume diffusion.

6. A significant increase in microhardness and strength is observed on addition of alloying elements which is further increased by addition of RE oxides both at room temperature and at 700 $^\text{O}$C.

7. Sub-micron grains in the SPSed ODS alloys are observed.

8. TEM study revealed the presence of nanometre sized Cr-Ti-O-RE precipitates in the matrix whereas XRD analysis shows the presence of second phase $Cr_{0.875}Ti_{0.125}$ particles.

9. CeO_2 increases the hardness of the matrix with respect to La_2O_3 and Y_2O_3 due to larger precipitate size. La_2O_3 having higher precipitate volume fraction increases strength at room temperature. On the other hand, due to the smaller precipitate sizes and highest number density of precipitates in case of Y_2O_3 alloy, the alloy has better strength than CeO_2 alloy at room temperature.

Data availability

The raw/processed data required to reproduce these findings cannot be shared at this time as the data also forms part of an ongoing study.

Acknowledgement

References

1. A. Kohyama, A. Hishinuma, D.S. Gelles, R.L. Klueh, W. Diets and K. Ehrich, Auger spectroscopy study of the stress enhanced impurity segregation in a Cr-Mo-V steel, J. Nucl. Mater. 138 (1996) 233.

2. F.A. Garner, M.B. Toloczko and B.H. Sencer, Comparison of swelling and irradiation creep behaviour of fcc-austenitic and bcc-ferritic/martensitic alloys at high neutron exposure, J. Nucl. Mater. 276 (2000) 123.

3. R.L. Klueh and D.H. Harries, High-chromium ferritic and martensitic steels for nuclear applications, ASTM, Book 3, July 1, 2001.

4. B. Raj, S. L. Mannan, P. Rao and M. D. Mathew, Development of fuels and structural materials for fast breeder reactors, Sadhana 7 (2002) 527.

5. C. Suryanarayana, Mechanical alloying and milling, Prog. Mater. Sci. 46 (2001) 1.

6. C.L. Chen and Y. M. Dong, Effect of mechanical alloying and consolidation process on microstructure and hardness of nanostructured Fe–Cr–Al ODS alloys, Mater. Sci. Eng. A 528 (2011) 8374.

7. C. Suryanarayana, E. Ivanov and V.V. Boldyrev, Mater. Sci. Eng. A 304 (2001) 151.

8. J.B. Fogagnolo, F. Velasco, M.H. Robert and J.M. Torralba, The science and technology of mechanical alloying, Mater. Sci. Eng. A 342 (2003) 131.

9. M. Zawrah and L. Shaw, Microstructure and hardness of nanostructured Al/Fe/Cr/Ti alloys through mechanical alloying, Mater. Sci. Eng. A 355 (2003) 37.

10. R. Juarez, J.J. Sunol, R. Berlanga, J. Bonastre and L. Escoda, The effects of process control agents on mechanical alloying behaviour of a Fe–Zr based alloy, J. Alloys Compd. 434 (2007) 472.

11. Z. Oksiuta and N. Baluc, Effect of mechanical alloying atmosphere on the microstructure and Charpy impact properties of an ODS ferritic steel, J. Nucl. Mater. 386 (2009) 426.

12. X.L. Wang, G.F. Wang and K.F. Zhang, Effect of mechanical alloying on microstructure and mechanical properties of hot-pressed Nb–16Si alloys, Mater. Sci. Eng. A 527 (2010) 3253.

13. O. Guillon, Field-assisted sintering technology / spark plasma sintering: Mechanisms, Materials, and Technology Developments, Adv. Eng. Mat. 16 (2014) 830

14. KU Leuven, SPS process modeling, https://www.mtm.kuleuven.be/Onderzoek/Ceramics/research/sintering/spark-plasma (accessed 09/27/2018).

15. M. Suárez, A. Fernández, J.L. Menéndez, R. Torrecillas, H. U. Kessel, J. Hennicke, R. Kirchner and T. Kessel, Challenges and Opportunities for Spark Plasma Sintering: A Key Technology for a New Generation of Materials in Sintering Applications, 2013, http://dx.doi.org/10.5772/53706 (accessed 09/27/2018).

16. R. Orru, R. Licheri, A. M. Locci, A. Cincotti and G. Cao, Consolidation/synthesis of materials by electric current activated/assisted sintering, Mater. Sci. Eng. R 63 (2009) 127.

17. E. Olevsky, S. Y. Kandukuri and L. Froyen, Consolidation enhancement in spark-plasma sintering: Impact of high heating rates, J. Appl. Phys. 102 (2007) 114913.

18. L. Toualbi, C. Cayron, P. Olier, J. Malaplate, M. Praud, M.-H. Mathon, D. Bossu, E. Rouesne, A. Montani, R. Logé and Y. de Carlan, Assessment of a new fabrication route for Fe–9Cr–1W ODS cladding tubes, J. Nucl. Mater. 428 (2012) 47.

19. S. Noh, A. Kimura and T. K. Kim, Diffusion bonding of 9Cr ODS ferritic/martensitic steel with a phase transformation, Fusion Eng. Des. 89 (2014) 1746.

20. S.A. Briggs, P.D. Edmondson, K.C. Littrell, Y. Yamamoto, R.H. Howard, C.R. Daily, K.A. Terrani, K. Sridharan and K.G. Field, A combined APT and SANS investigation of α´ phase precipitation in neutron-irradiated model FeCrAl alloys, Acta Mater. 129 (2017) 217.

21. S. Ukai Hokkaido University, Sapporo, Japan, Oxide Dispersion Strengthened Steels, https://www.slideshare.net/jufortunato84/oxide-dispersion-strengthened-steels?from_action=save, (accessed 12/31/2018).

22. C. Topbasi, D. Kaoumi, A. T. Motta and M. A. Kirk, Microstructural evolution in NF616 (P92) and Fee9Cre0.1C-model alloy under heavy ion irradiation, J. Nucl. Mat. 466 (2015) 179.

23. S. Li, Y. Wang, X. Dai, F. Liu, J. Li and X. Wang, Evaluation of hardnening behaviors in ion-irradiated Fe-9Cr and Fe-20Cr alloys by nanoindentation technique, J. Nucl. Mater. 478 (2016) 50.

24. K. Ono, K. Arakawa, H. Shibasaki, H. Kurata, I. Nakamichi and N. Yoshida, Release of helium from irradiation damage in Fe-9Cr ferritic alloy, J. Nucl. Mater. 329 (2004) 933.

25. K. Ono, H. Sasagawa, F. Kudo, M. Miyamoto and Y. Hidaka, Effects of tungsten on thermal desorption of helium from Fe–9Cr–2W ferritic alloy irradiated with low energy helium ions, J. Nucl. Mat. 417 (2011) 1026.

26. W. Eiichi, H. Akimichi, U. Kouji, K. Yasushi, T. Seiici and A. Kenji, Damage Structures and Mechanical Properties of High-Purity Fe–9Cr Alloys Irradiated by Neutrons, Mater. Trans. 41 (9) (2000) 1180.

27. L. Toualbi, C. Cayron, P. Olier, R. Logé and Y. de Carlan, Relationships between mechanical behavior and microstructural evolutions in Fe 9Cr–ODS during the fabrication route of SFR cladding tubes, J. Nucl. Mat. 442 (2013) 410.

28. L. Toualbi, C. Cayron, P. Olier, J. Malaplate, M. Praud, M. H. Mathon, D. Bossu, E. Rouesne, A. Montani, R. Logé and Y. de Carlan, Assessment of a new fabrication route for Fe–9Cr–1W ODS cladding tubes, J. Nucl. Mat. 428 (2012) 47.

29. K. Rajan, T. Shanmugasundaram, V.S. Sarma, and B.S. Murty, Effect of Y_2O_3 on Spark Plasma Sintering Kinetics of Nanocrystalline 9Cr-1Mo Ferritic Oxide Dispersion-Strengthened Steels, Metall. Mater. Trans. A 44A (2013) 4037.

30. M. Zakeri, M. Ramezani and A. Nazari, Prediction of the mean grain size of MA-synthesized nanopowders by artificial neural networks, Mater. Res. 15 (2012) 6.

31. J.B. Nelson and D.P. Riley, An experimental investigation of extrapolation methods in the derivation of accurate unit-cell dimensions of crystals, Proc. Phys. Soc. 57 (1945) 160.

32. G.K. Williamson and W.H. Hall, X-ray line broadening from filed aluminium and wolfram, Acta Metall. 1 (1953) 22.

33. X.T.A. Chu, B.N. Ta, L.T.H. Ngo, M.H. Do, P.X. Nguyen, D.N.H. Nam, Microwave absorption properties of iron nanoparticles prepared by ball-milling, J. Electron. Mater. 45 (2016) 2311.

34. S. Liu, A. Wang, J. Xie, Effect of deformation temperature, strain rate and strain on the strain hardening exponent of copper/aluminium laminated composites, Adv. Comp. Letts. 27 (4) (2018) 129.

35. H. J. Kleemola and M. A. Nieminen, On the strain-hardening parameters of metals, Met. Trans. 5 (1974) 1863.

36. W.S. Young and I.B. Cutler, Initial sintering with constant rates of heating, J. Am. Ceram. Soc. 53 (1970) 659.

37. J. Guyon, A. Hazotte, J.P. Monchoux and E. Bouzy, Effect of powder state on spark plasma sintering of TiAl alloys, Intermetallics 34 (2013) 94.

38. S. Pasebani, I. Charit, D. P. Butt, J. I. Cole, Y. Wu and J. Burns, Sintering behavior of lanthana-bearing nanostructured ferritic steel consolidated via spark plasma sintering, Adv. Engg. Mat. 18 (2) (2016) 324.

39. S. Schmauder and C. Kohler, Atomistic simulations of solid solution strengthening of α-iron. Computational Mater. Sci. 50 (4) (2011) 1238.

40. S. Pasebani, I. Charit, I., K. Allahar, B. Jaques., D. Butt, and J. Cole (2011). Microstructural characterization of mechanically alloyed lanthana-bearing oxide dispersion strengthened steels, Minerals, Metals and Materials Society/AIME, 420 Commonwealth Dr., P. O. Box 430 Warrendale PA 15086 United States.

41. S. Pasebani, I. Charit, Y. Wu, D. P. Butt and J. I. Cole, Mechanical alloying of lanthana-bearing nanostructured ferritic steels, J. of Acta Mater, 61 (2013) 5605.

42. C.A. Williams, P. Unifantowicz, N. Baluc, G.D. Smith and E.A. Marquis, Acta Mater (2013) 2219.

Chapter 6: A Study on helium and sulfur ion irradiation of pure BCC Iron

Arnab Kundu, Allyssa Bateman, Brian Jaques, Indrajit Charit, Chao Jiang and Lin Shao

Abstract

Metallic alloys are widely used or are being planned for use as structural and cladding materials in current and future reactors. Under irradiation, grain boundary (GB) cohesion strength decreases due to interaction with defects and impurities, leading to intergranular fracture and embrittlement of alloys. A new technique for understanding grain boundary cohesion and its impact on fracture behavior in irradiated alloys has been developed by the utilization *in situ* transmission electron microscopy (TEM) push-to-pull (P2P) tensile testing technique. This work is focused on studying intergranular fracture behavior in pure BCC iron that has been irradiated with He^+ and S^{2+} ions at 550 ^{O}C.

6.1. Introduction

The degradation of the mechanical properties of the nuclear material due to neutron or ion irradiations possess a heavy setback to the widespread use of nuclear energy [1]. Body centered cubic ferritic steels are considered for use as structural and cladding materials in future nuclear reactors. Mechanical integrity of these alloys is of utmost importance to ensure

safe reactor operation. In extreme environments of a reactor core, under neutron or ion irradiations, many point defects and their clusters will be directly formed during collision cascades. Diffusion of interstitials or vacancies towards sinks such as grain boundaries can lead to redistribution of solute concentrations, resulting in so-called radiation-induced segregation effect [2]. The motion of dislocations can also be obstructed by nano-sized clusters made of point defects (vacancies or interstitials) produced [3]. The accumulation of obstacles makes the mobility of dislocations limited and thus increases the fragility of the material [4,5]. Irradiation can alter the distribution of alloying elements, phase stability and the kinetics of phase transformations. This phenomenon not only affect the mechanical properties of the cladding material, but creep resistance properties [6,7]. The cladding material should be able to withstand the service temperatures making thermal creep resistance and microstructural stability key issues for the selection of materials as there is a trend to increase the service temperatures to achieve higher thermal efficiency for the reactor [8,9]. All of these mechanisms result in detrimental impact on the grain boundary strength which ultimately alters the fracture behavior of the material.

In ferritic Fe-Cr alloys, both radiation-induced depletion and enrichment of Cr at grain boundaries (GBs) have been observed [10]. Due to super-saturation of point defects created under irradiation, radiation-enhanced diffusion can also greatly accelerate the segregation of impurity elements to GB. In nuclear reactors, large quantities of helium are also produced by transmutation reactions [11,12]. They have a detrimental effect on the micro-structural evolution of materials under irradiation and with possible implications from a macroscopic point of view [12]. Pure alpha-iron is an important model material, as it serves as the matrix

material for many ferritic steels which are promising materials for future nuclear applications [13].

The present work focusses in understanding the fracture behavior of pure BCC iron pre and post irradiation. Understanding the fracture behavior at micro scale is very important for getting an idea about the grain boundary cohesive energy. This work has been done keeping in mind to draw an analogy between the experimentally obtained grain boundary cohesive energy to that obtained from MOOSE simulation and density functional theory(DFT) but the later part is beyond the present scope of study. A new novel in situ tensile testing technique has been developed which gives us an understanding of the fracture mechanism at micro scale.

6.2. Materials and Methods

The present study deals with a comparative study of different irradiation conditions of pure iron. The pure iron rod (diameter 12 mm) was purchased from Alfa Aesar (Product No.: 40499, Lot No.: M21B024) having iron (purity 99.991 wt%). The major impurities included oxygen (200 ppm), carbon (<100 ppm), phosphorus (<7.2 ppm), hydrogen (<10ppm) and nitrogen (<100 ppm) as reported in the test certificate provided by Alfa Aesar. The carbon content was determined by infrared (IR) spectroscopy. Hydrogen and nitrogen were determined by IGF-TC. Oxygen was determined by IFG-NDIR. All other elements were determined by GDMS process. The samples were cut in small discs having diameter of 12 mm. and were polished upto 0.3 µm. The Vickers microhardness test was performed a LECO LM-100 Microhardness Tester using a load of 0.5 kgf (~4.9 N) and a loading time of 15 s at

10 different random points. The samples were etched with 5% Nital (5 vol.% nitric acid + 95 vol.% ethanol) for 20 s. The microstructures were observed in Olympus PGM-3 optical microscope and the grain size were determined by mean linear intercept method. The samples were then heat treated at 700 ^{O}C in a box furnace in argon atmosphere for different durations (1 week, 2 weeks and 4 weeks). The samples were polished and the microhardness tests were performed and optical microstructure were observed.

The 2-week heat treated samples had average grain size of 108.2 µm which was desired for irradiation test. The 2-week heat treated samples were then sent to Texas A&M Ion Beam Laboratory for performing ion irradiation experiments. The Stopping and range of ions in matter (SRIM) and Transport of ions in matter (TRIM) calculations[14] were performed in order to have an idea of the depth versus dpa profile before actually starting the irradiation experiments. The irradiation was performed on the iron at 3 MeV beam energy, two different temperatures (27 ^{O}C and 550 ^{O}C) under two different doses of 1 dpa and 3 dpa using two different ions, which are helium (He^{+}) and sulfur (S^{2+}) in defocused mode. The irradiation region covers roughly 6×6 mm^{2} around the center of the sample having a thickness of 0.5mm. The overall irradiation procedure is shown in Table 6.1.

Table 6.1: Irradiation experiment conditions for 2-week heat treated pure Iron.

Sample ID	Energy (MeV)	Ions	DPA	Ion Fluence (ions/cm^2)	Temperature (^{O}C)	Beam Current (nA)
1	3	He$^+$	3	1.62 x10^{17}	550	200
2	3	S^{2+}	3	5.28 x10^{15}	550	200

Post irradiation, samples were lifted from the irradiated region by focused ion beam (FIB) milling in a Scios FEI FIB-SEM at and later viewed in JEOL 2010J Transmission Electron Microscope (TEM) in order to understand the presence of radiation-induced defects (clusters, voids, bubbles, segregations). The heat treated samples were also sent to the Boise State University for capabilities for performing using FIB (FEI Quanta 3D FEG) for sample fabrication, electron backscattered diffraction (EBSD) for grain boundary quantification, and in situ TEM (FEI Tecnai TF-30FEG TEM and Hysitron PI-95 Picoindenter) tensile testing by push to pull device (P2P). Micro sized samples were lifted out from the irradiated region by fibbing and were welded to the P2P device as shown in Figure 6.1(a)-(c). The top view and side view of the sample welded are shown in Figure 6.1(d) and 6.1(e), respectively.
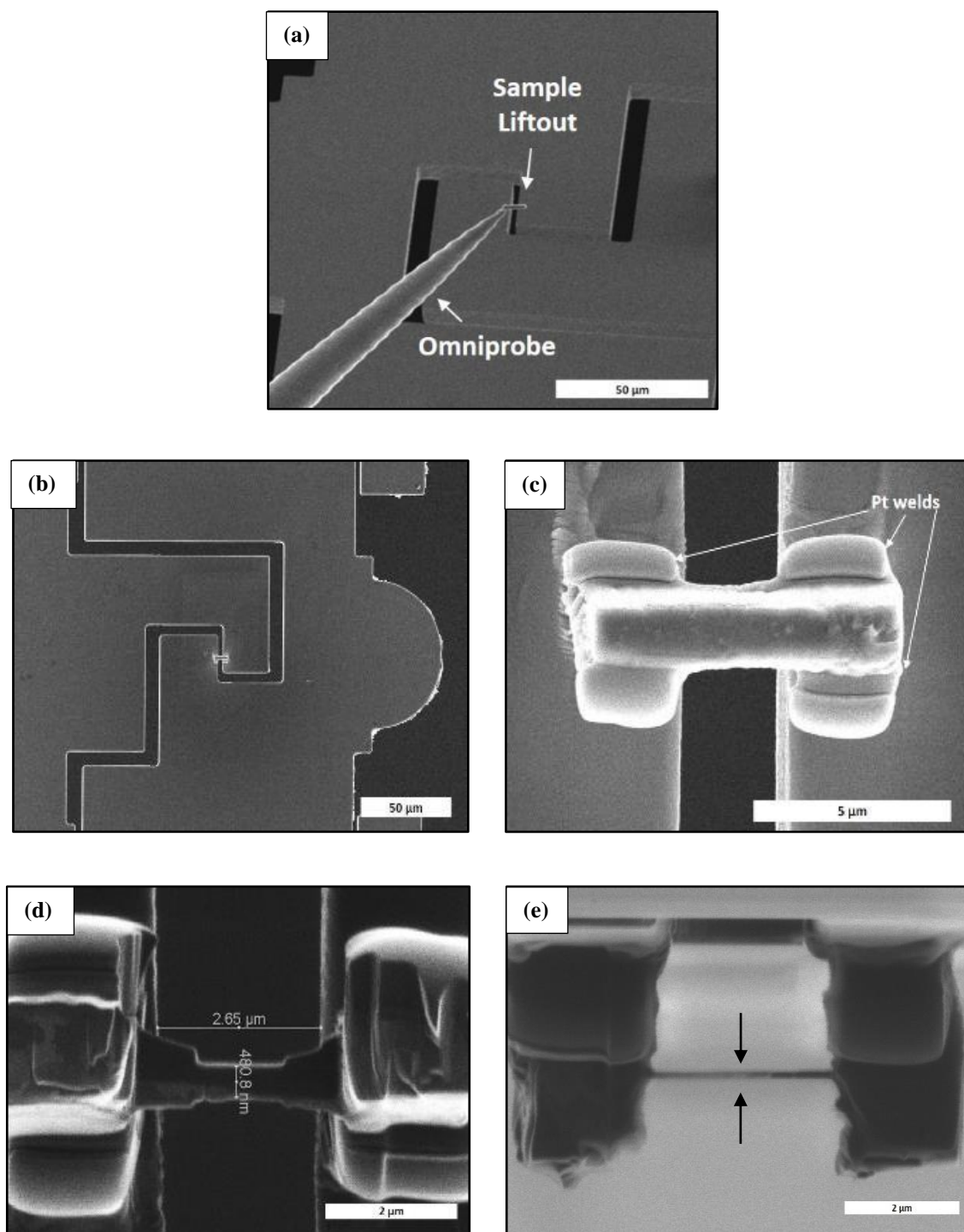
Figure 6.1: Process of P2P technique: (a) Sample lifted after FIBing, (b) Sample welded in the P2P device, (c) Enlarged view of the welded sample, (d) Top view of the welded sample, and (e) Side view of the welded sample.

6.3. Results and Discussion

The microstructure of the as received and heat treated (HT) pure iron specimen is shown in Figure 6.2(a)-(d). The microstructure of the as received iron depicts distorted microstructure with plenty of deformation banding. Also, the grain boundaries are not well defined. With heat treatment due to recrystallization and grain growth mechanism, the grain boundaries became well defined and an increase in grain size is observed as shown in Table 6.2. A decrease in microhardness is also observed (Table 6.2) which is as a result of increasing grain size.
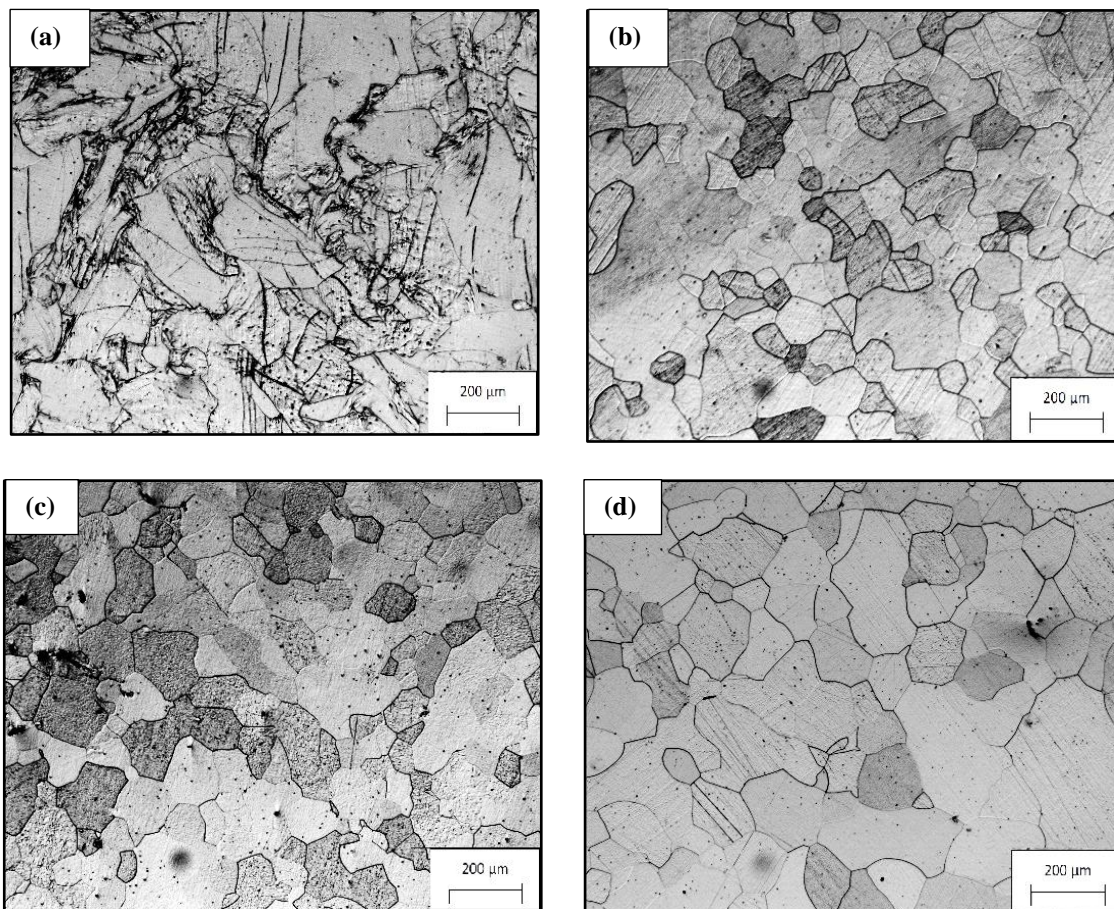

Figure 6.2: Optical Microstructure of pure iron: (a) As received, (b) 1 week HT,
(c) 2 weeks HT and (d) 4 weeks HT

Table 6.2: Grain Size of heat treated pure iron (Heat Treatment- HT)

Sample	As Received	1 week HT	2 week HT	4 week HT
Grain Size (μm)	80.9 ± 36.2	99.9 ± 25.6	108.2 ± 12.5	130.7 ± 16.7
Microhardness (VHN)	119.2 ± 30.5	71.2 ± 2.5	67.3 ± 1.3	59.2 ± 6.5

According to the density functional theory (DFT) calculations (see Table 6.3), sulfur present (S) in steels and helium (He) produced by nuclear transmutation reactions all have a strong tendency to segregate at grain boundaries. An important consequence of the local enrichment of impurities at grain boundaries is that they can weaken grain boundary cohesion considerably and induce intergranular fracture and embrittlement. Among other elements, present DFT calculations reveal a dramatic reduction in grain boundary cohesion energy due to the segregation of S and He.

Table 6.3. DFT calculated segregation energies (E_{seg}) of impurities to a Σ5(310)[001] symmetric tilt GB in bcc Fe. The change of the GB cohesion strength (dE_{coh}) due to impurity segregation is also shown.

Impurity	S	P	He	Cu	Si	Al	Mo	Ni	Cr
E_{seg} (eV)	-1.25	-0.87	-1.51	-0.56	-0.44	-0.38	-0.40	-0.40	-0.25
dE_{coh} (eV)	-2.25	-1.30	-3.21	-0.33	-0.48	-0.22	+0.90	+0.04	+0.47

The SRIM-TRIM calculations were performed using SRIM 2013 software using Kinchin-Pease (KP) model. The simulation study can only be performed at room temperature conditions. The number of ions used for the calculation is 99999. Figure 6.3(a) shows the dose versus the depth profile for the He^+ ions on pure iron for 3 dpa. Figure 6.3(b) shows a similar

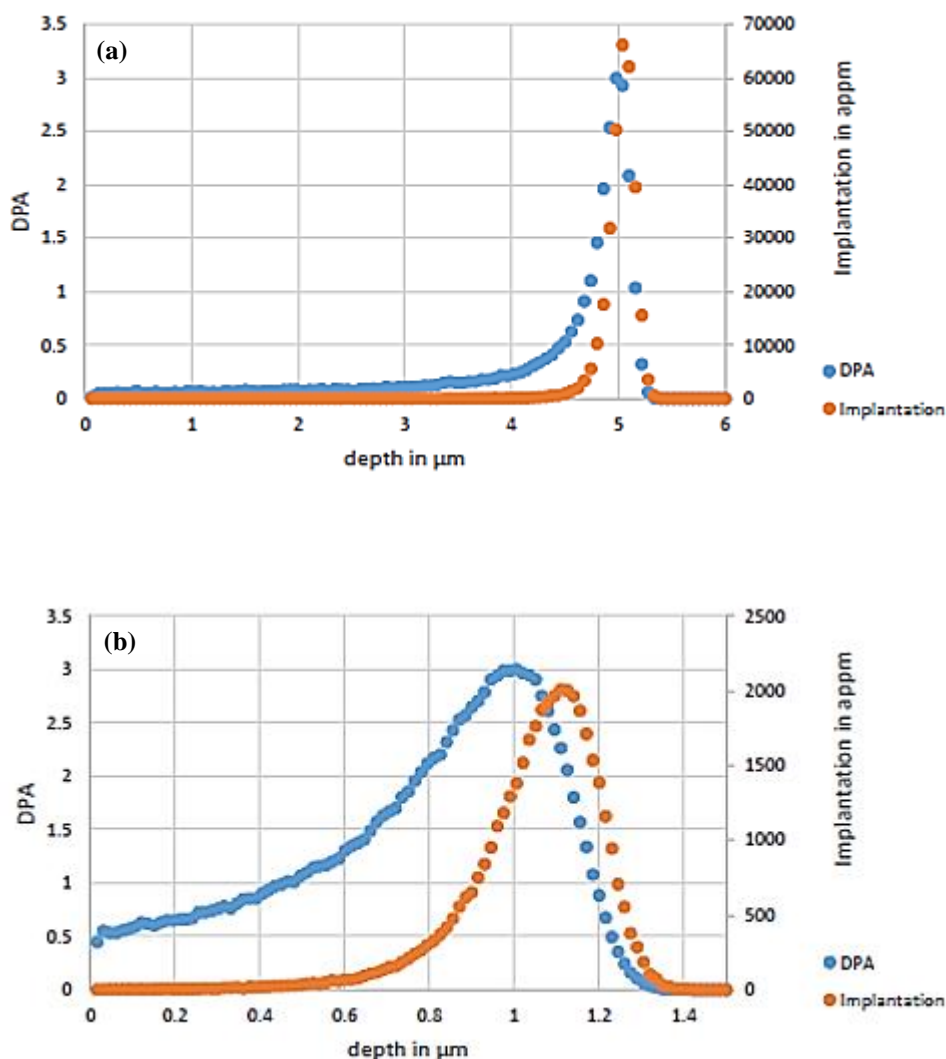kind of plot for the S^{2+} ion bombardment for 3 dpa. All the calculations were done assuming 3 MeV beam energy.

Figure 6.3: SRIM-TRIM calculation of implantation on pure iron for (a) He^+ ion for 3 dpa and (b) S^{2+} ion for 3 dpa

From the SRIM calculations, it can be noted that the maximum damage on the pure iron sample due to He^+ implantation will occur around 5 µm depth whereas S^{2+} ion will occur around 1 µm depth for same energy of 3 MeV. The reason behind damage due to S^{2+} occurring at less depth than He^+ at same ion energy is because of the fact that S^{2+} ion is heavier and

larger in size than He$^+$. The mean free path for He$^+$ ions is larger than that of the S^{2+} ions with the same energy [15].

After irradiation of the 2-week HT iron, microstructural characterization was performed after FIBing. The sample was FIBed from the irradiated region through thickness for understanding the nature of irradiated damage region as shown in Figure 6.4.
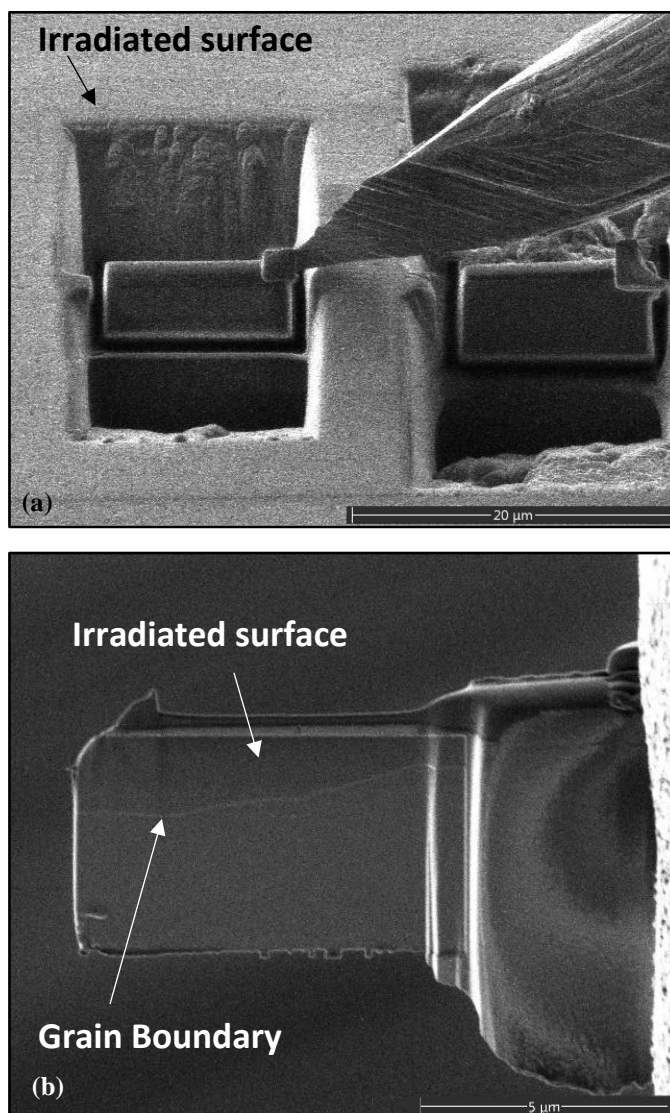

Figure 6.4: FIBing process of an irradiated sample: (a) FIB lift out and (b) Final sample after the completion of fibbing

Post FIBing, the samples were viewed in the TEM. Figure 6.5 (a)-(c) show the through-thickness pure iron for He$^+$ ion irradiation for 3 dpa at 550 ^{O}C and 6.5 (d)-(g) shows the though thickness pure iron for S^{2+} ion irradiation for 3 dpa at 550 ^{O}C.
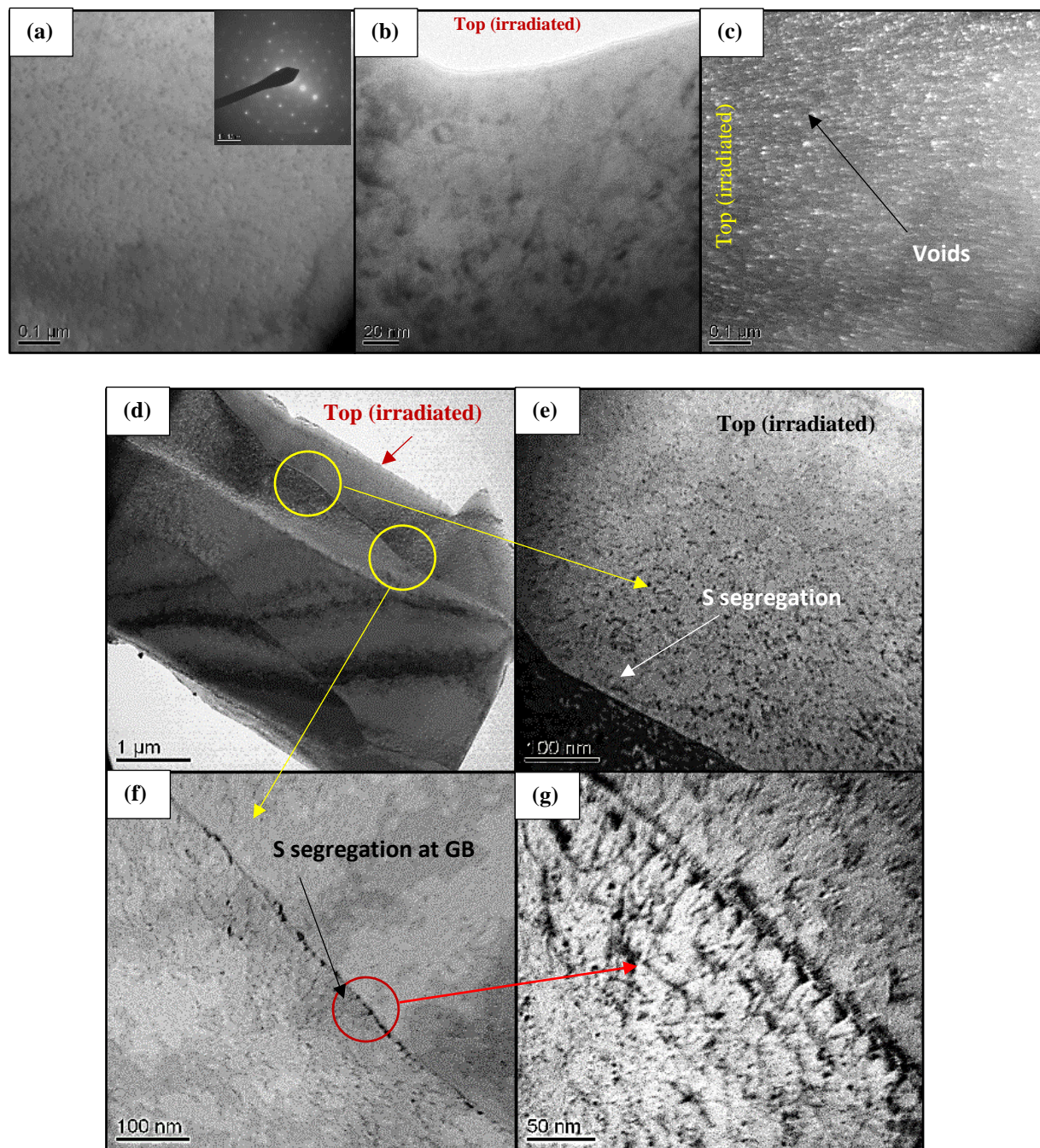

Figure 6.5: TEM image of pure iron irradiated at 550 ^{O}C at 3 dpa by (a)-(c) He$^+$ and (d)-(g) S^{2+}

Figure 6.5(a)-(b) shows the formation of defects (voids) in the iron matrix. The defect density is less at the top surface and keeps on increasing as one goes into the material along the through-thickness. Figure 6.5(c) shows the corresponding dark field image of the area as shown in Figure 6.5(a). The bright colored regions are the voids present in the matrix. From this figure, it appears like all the voids are having some directional effect, i.e. they are formed in the direction of ion flow. Figure 6.5(d)-(g) shows the sulfur segregation due to irradiation. Two grain boundaries are seen as shown in figure 6.5(d), one near the irradiated region and one far away. Near the grain boundary in the irradiated region, concentrated area of segregations is seen. The segregation density was highest in the vicinity of 1 μm from the top. Segregations are also seen in the grain boundaries. Near the top grain boundary numerous dislocations and dislocation loops are found which are not so much seen near the bottom grain boundary. EDS spectra of the segregated regions show the presence of sulfur, but since the sulfur concentration is very low, an accurate estimate of the segregated phase is not possible to know with EDS. The sulfur segregation increases depth is comparable to the SRIM calculations as shown in figure 6.3(b). Moreover, it is observed that sulfur tends to segregate more in the vicinity of the grain boundary.

In situ P2P tensile testing was first done from the samples FIBed out of the unirradiated region then the He^+ ion irradiated sample and S^{2+} ion irradiated sample; last two samples were irradiated for 3 dpa at 550 ^{O}C. The results of the P2P testing are summarized as below:

Sample 1 (pure iron from unirradiated region)

Figure 6.6(a) shows the sample lift-off with the corresponding EBSD image. Figure 6.6(b) shows the stress-strain curve obtained from the tensile testing. Figure 6.6(c) shows the process of intragranular fracture in the sample during P2P process.
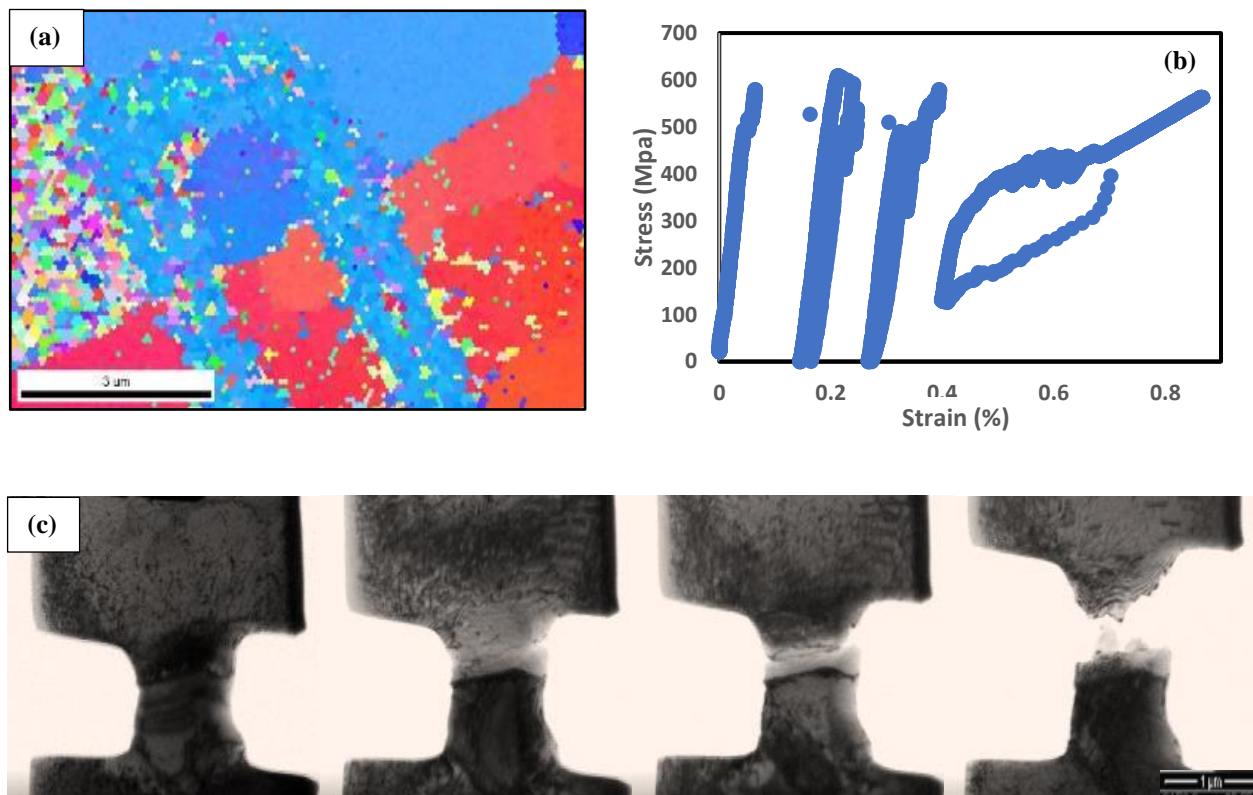

Figure 6.6: In Situ P2P process: (a) EBSD of sample lift off region, (b) Stress-strain curve of the tensile test and (c) Process of fracture occurring during tensile testing

In situ tensile testing for all the samples of unirradiated pure iron showed an approximate yield strength in the vicinity of 600-800 MPa. Intragranular fracture above the grain boundary is observed during the tensile testing.

Sample 2 (He$^+$ irradiated pure iron):

Figure 6.7(a) shows the sample lift off with the corresponding EBSD image. Figure 6.7(b) shows the stress-strain curve obtained from the tensile testing. Figure 6.7(c) shows the process of intragranular fracture in the sample during P2P process.
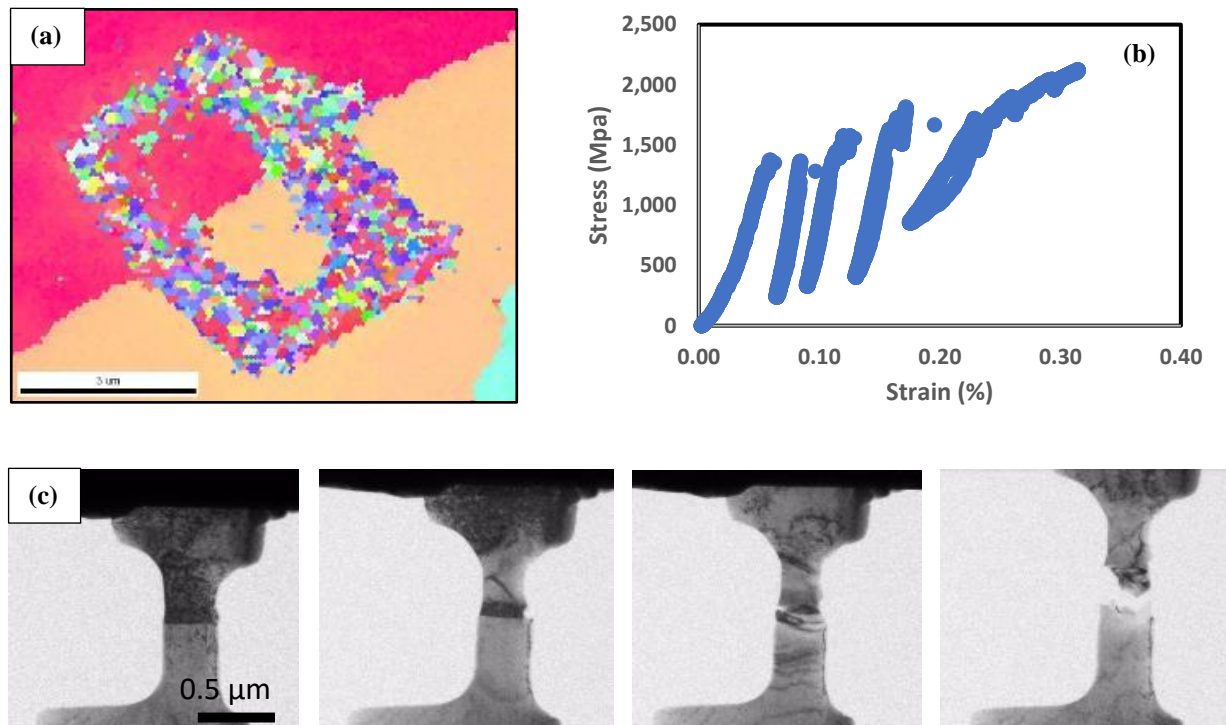

Figure 6.7: In Situ P2P process: (a) EBSD of sample lift off region, (b) Stress-strain curve of the tensile test and (c) Process of fracture occurring during tensile testing

In situ tensile testing for all the samples of He$^+$ irradiated pure iron showed an approximate yield strength in the vicinity of 1500-2000 MPa. Intragranular fracture is also observed during the tensile testing. The failure initiates at the grain boundary but proceeds through the grain.

Sample 2 (S^{2+} irradiated pure iron)

Figure 6.8(a) shows the sample lift off with the corresponding EBSD image. Figure 6.8(b) shows the stress-strain curve obtained from the tensile testing. Figure 6.8(c) shows the process of intragranular fracture in the sample during P2P process.
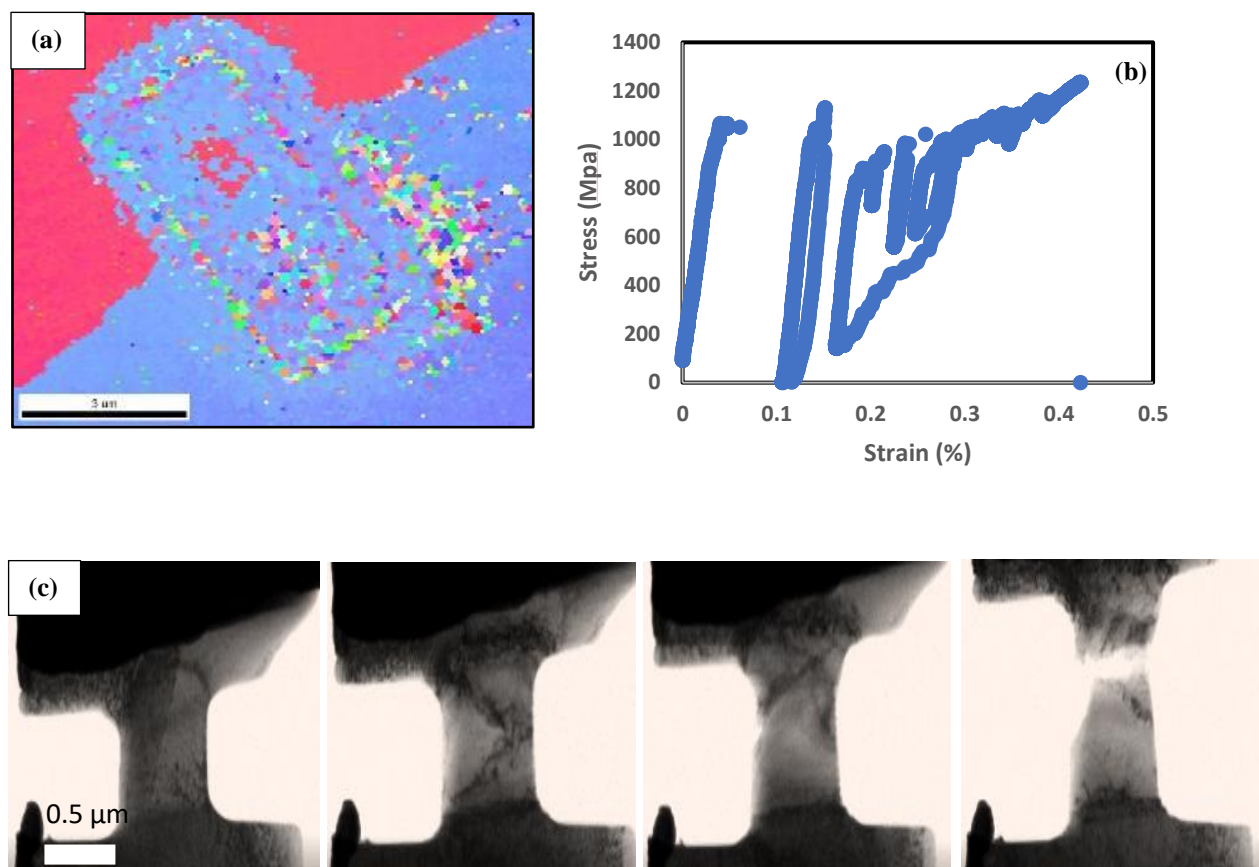

Figure 6.8: In Situ P2P process: (a) EBSD of sample lift off region, (b) Stress-strain curve of the tensile test and (c) Process of fracture occurring during tensile testing

In situ tensile testing for all the samples of unirradiated pure iron showed an approximate yield strength in the vicinity of 1000-1100 MPa. Intragranular fracture is observed during the tensile testing. Similar to the He$^+$ ion irradiation, failure initiates at grain boundary and proceeds through the grain.

A comparison of the variation in yield strength is shown in Table 6.4.

Table 6.4. P2P Tensile testing results for the non-irradiated and irradiated BCC iron

Material	No. of Samples	Type of fracture	Approximate yield strength (MPa)	Angle of Misorientation (^{O})
Pure Iron	3	Intragranular fracture initiating at GB	600-800	43.3 @ [21 -1 -21] 40.7 @ [-2 -26 -15] 43.8 @ [7 27 0]
He+ irradiated iron	3	Intragranular fracture on the diagonal and also initiating at GB	1500-2000	13.4 @ [-1 10 0] 13.4 @ [-1 10 0] 38.6@ [3 -3 5]
S+ irradiated iron	3	Intragranular fracture initiating at GB	1000-1100	14.5 @ [22 3 -13] 33.3 @ [-2 -3 18] 58.7 @ [-16 17 -7]

The yield strength of the matrix increases due to the introduction of voids when the sample was irradiated with He$^+$ ions as seen previously from the TEM imaging. Also due to sulfur segregation due to S^{2+} irradiation, the matrix yield strength increases. But post irradiation, the material starts failing at lower strain. Fracture starts occurring at grain boundaries but generally proceeds through the grains.

6.4. Conclusions

The main objective of this study was to understand the effect of He$^+$ and S^{2+} ion implantation on pure BCC iron. The study is also for the development of this novel P2P in

situ tensile testing instead of conventional cantilever bend testing process. The damage profile obtained from the SRIM calculations is almost similar to that obtained from experiment, the deviation may be attributed to the high temperature during irradiation which cannot be taken into consideration during SRIM calculations. In the He^+ irradiated material voids are found to be present and the void number density is found to be large in the vicinity of 5 µm depth from the irradiated surface. In case of S^{2+} irradiated materials, sulfur segregation is seen at the grain boundaries and also near the vicinity of 1 µm depth from the irradiated surface. In situ P2P tensile testing shows us the base BCC iron has a yield strength of 600-800 MPa. The yield strength increases to 1500-2000 MPa after He^+ irradiation due to the introduction of voids, while it increases to 1000-1100 MPa due to sulfur segregation during S^{2+} irradiation.

Data availability

The raw/processed data required to reproduce these findings cannot be shared at this time as the data also forms part of an ongoing study.

Acknowledgement

References

1. D. Brimbal, B. Décamps, A. Barbu, E. Meslin, J. Henry, Dual-beam irradiation of a-iron: Heterogeneous bubble formation on dislocation loops, J. Nucl. Mater. 418 (2011) 313.

2. S. Dudarev et al., The EU programme for modelling radiation effects in fusionreactor materials: an overview of recent advances and future goals, J. Nucl.Mater. 1 (2009) 386.

3. M. Lambrecht, On the correlation between irradiation-induced microstructural features and the hardening of reactor pressure vessel steels, J. Nucl. Mater. 406 (2010) 84.

4. E. Gaganidze, H.-C. Schneider, B. Dafferner, J. Aktaa, Embrittlement behavior ofneutron irradiated RAFM steels, J. Nucl. Mater. 367 (2007) 81.

5. B.C. Masters, Dislocation loops in irradiated iron, Nature 200 (1963).

6. Robertson Jal. Zirconium: an international nuclear material. J. Nucl. Mater. 100 (1981) 108.

7. Northwood Do., The development and application of zirconium alloys. Mater. Des. 6(2) (1985) 58.

8. Motta AT, Yilmazbayhan A, Silva MJG, Comstock RJ, Was GS, Busby JT, et al. Zirconium alloys for supercritical water reactor applications: challenges and possibilities. J. Nucl. Mater. 61 (2007) 371.

9. Wikmark G, Hallstadius L, Yueh K. Cladding to sustain corrosion, creep and growth at high burn-ups, Nucl. Eng. Technol. 2009 41(2)143.

10. J.L. Boutard, A. Alamo, R. Lindau, M. Rieth, Fissile core and Tritium-Breeding Blanket: structural materials and their requirements, C. R. Phys. 9 (2008) 287.

11. N. Wanderka, E. Camus, H. Wollenberger, Microstructure Evolution of Selected Ferritic-Martensitic Steels under Dual-Beam Irradiation, Mater. Res. Soc. Symp. Proc. 439 (1997) 451.

12. R. Schaeublin, D. Gelles, M. Victoria, Microstructure of irradiated ferritic/martensitic steels in relation to mechanical properties, J. Nucl. Mater. (2002) 307.

13. T. Tanaka, K. Oka, S. Ohnuki, S. Yamashita, T. Suda, S. Watanabe, E. Wakai, Synergistic effect of helium and hydrogen for defect evolution under multi-ion irradiation of Fe–Cr ferritic alloys, J. Nucl. Mater. 294 (2004) 329.

14. J. F. Ziegler, J.P. Biersack, U. Littmark, The Stopping and Range of Ions in Matter., 1985, New York: Pergamon Press. ISBN 978-0-08-021607-2.

15. G. S. Was, Fundamentals of Radiation Materials Science, 2007, Metals and Alloys, ISBN 978-3-540-49472-0.

Chapter 7: Future work

This work has been performed in order to have a basic understanding of microstructural, mechanical and corrosion properties of Fe-Cr and Fe-9Cr ODS alloys processed via the route of high energy ball milling and spark plasma sintering. The Fe-9Cr ODS alloys are potential candidates for generation IV fast reactor fuel cladding material and various other applications. Due to limited time and limited resource availability, the author has been unable to investigate other properties of these alloys that would make them more suitable for the aforesaid application. Keeping in mind the potential usage of these alloys, in order to fabricate them for real life application purpose, the author would like to recommend some of the following future works:

(a) Further optimization of SPS process for ODS alloys for reducing porosity.

(b) Further optimization of the alloy composition by addition of other alloying elements and RE oxides for better high temperature applications.

(c) Understanding kinetics of consolidation in SPS process by both experimental and supported simulation studies.

(d) Further characterization of the ODS alloys with Atom probe tomography.

(e) Corrosion test in Molten bath of eutectic LiCl –KCl salt.

(f) Further ion irradiation and neutron irradiation of the Fe-9Cr based ODS alloys

(g) Characterization of the irradiated ODS alloys.

Appendix

A.1

Linear Polarization study on the Fe-Cr alloys and on Alloy HT-9 in 0.5M H_2SO_4, 0.05M NaH_2PO_4 solution and in 1M NaOH solution as shown in Figures A.1(a)-(c) respectively.
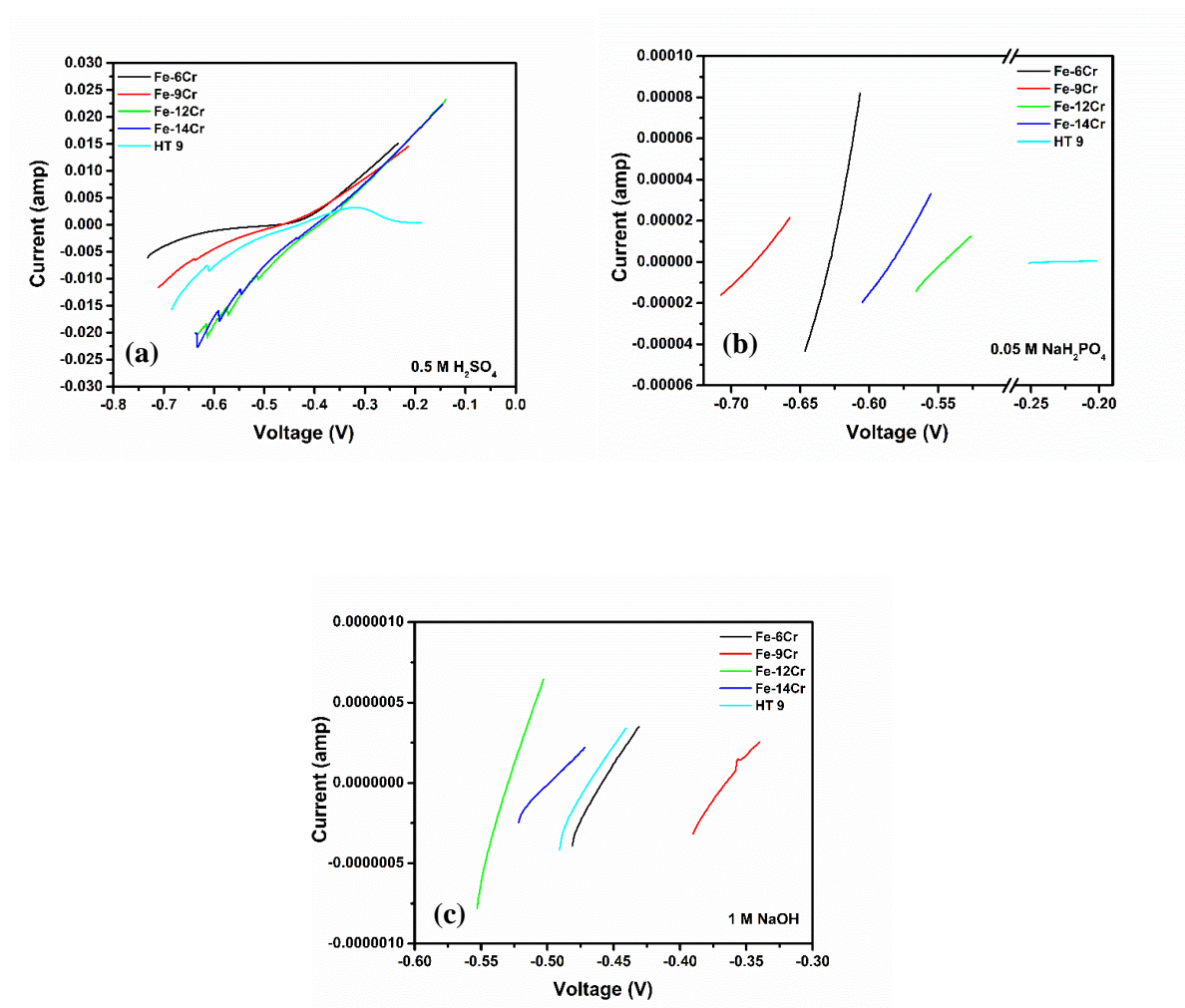

Figure A.1. LP in (a) 0.5M H_2SO_4, (b) 0.05M NaH_2PO_4 solution and (c) 1M NaOH solution

A.2

Nyquist plots of the Fe-xCr alloys and on Alloy HT-9 in 0.5M H_2SO_4, 0.05M NaH_2PO_4 solution and in 1M NaOH solution are shown in Figures A.2(a)-(c) respectively.
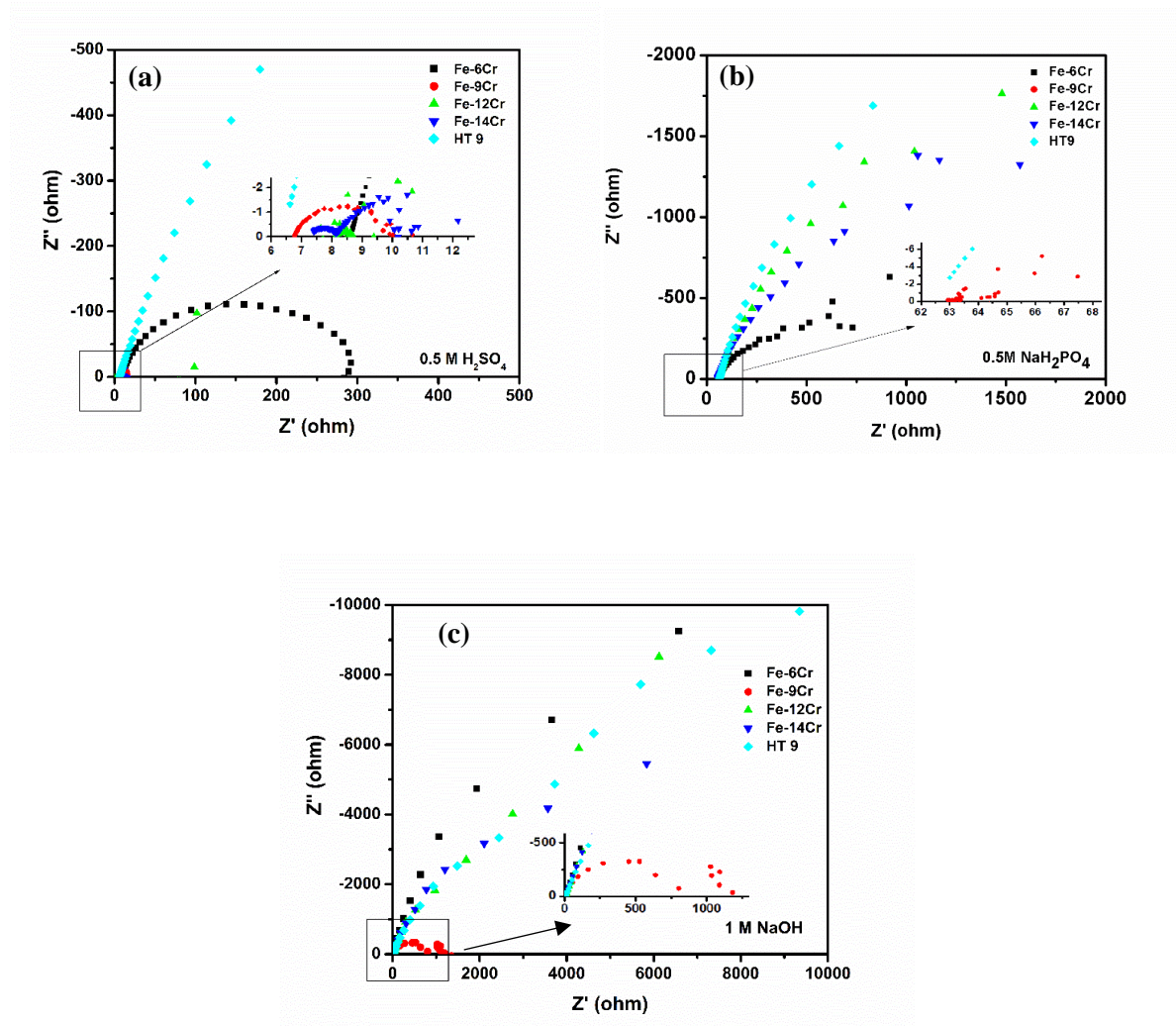

Figure A.2. Nyquist plots in (a) 0.5M H_2SO_4, (b) 0.05M NaH_2PO_4 solution and (c) 1M NaOH solution

A.3

Phase angle vs frequency plots of the Fe-xCr alloys and on Alloy HT-9 in 0.5M H_2SO_4, 0.05M NaH_2PO_4 solution and in 1M NaOH solution are shown in Figures A.3(a)-(c) respectively.
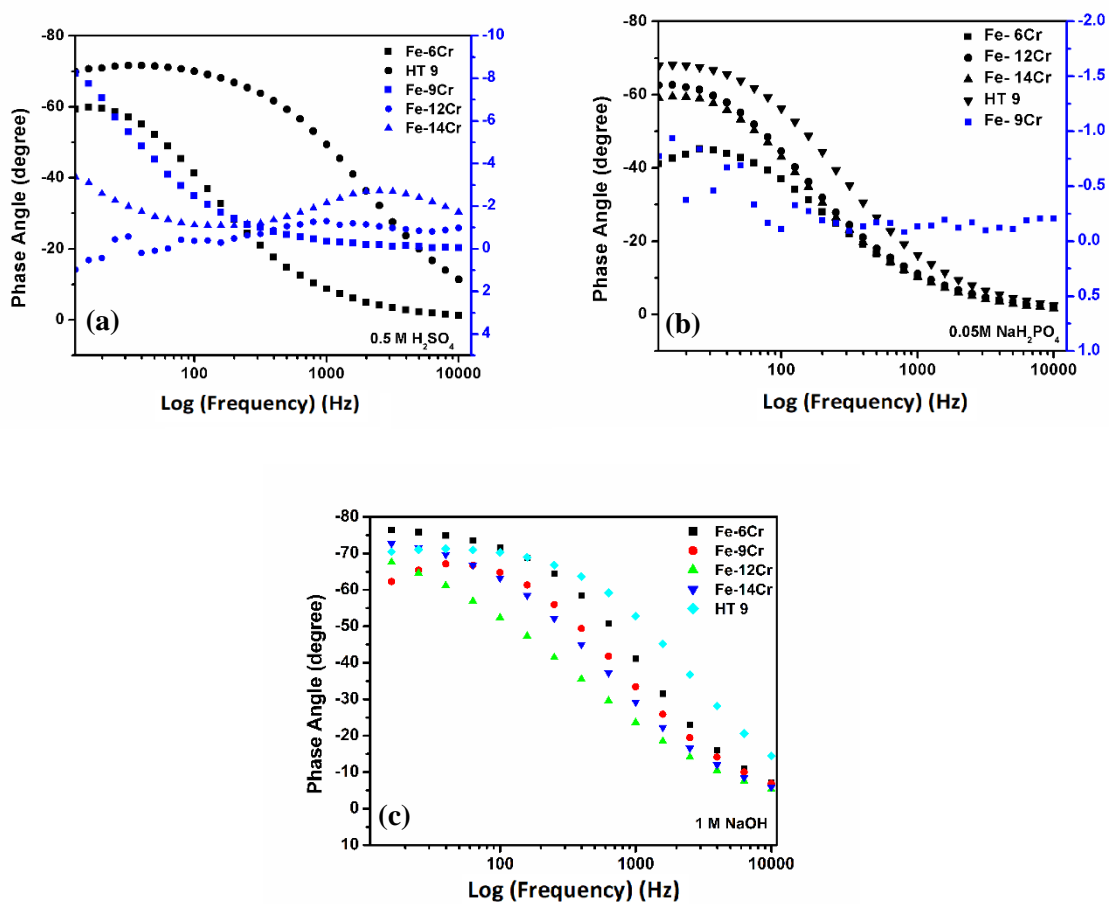

Figure A.3. Phase angle vs Frequency plots in (a) 0.5M H_2SO_4, (b) 0.05M NaH_2PO_4 and (c) 1M NaOH solution